

Quantitative Analysis of Microscopy

Rhodri S. Wilson

Submitted for the degree of Doctor of Philosophy

Heriot-Watt University

Institute of Biological Chemistry, Biophysics and Bioengineering

School of Engineering and Physical Sciences

August 2016

The copyright in this thesis is owned by the author. Any quotation from the thesis or use of any of the information contained in it must acknowledge this thesis as the source of the quotation or information.

Abstract

Particle tracking is an essential tool for the study of dynamics of biological processes. The dynamics of these processes happens in three-dimensional (3D) space as the biological structures themselves are 3D. The focus of this thesis is on the development of single particle tracking methods for analysis of the dynamics of biological processes through the use of image processing techniques. Firstly, introduced is a novel particle tracking method that works with two-dimensional (2D) image data. This method uses the theory of Haar-like features for particle detection and trajectory linking is achieved using a combination of three Kalman filters within an interacting multiple models framework. The trajectory linking process utilises an extended state space variable which better describe the morphology and intensity profiles of the particles under investigation at their current position. This tracking method is validated using both 2D synthetically generated images as well as 2D experimentally collected images. It is shown that this method outperforms 14 other state-of-the-art methods. Next this method is used to analyse the dynamics of fluorescently labelled particles using a live-cell fluorescence microscopy technique, specifically a variant of the super-resolution (SR) method PALM, spt-PALM. From this application, conclusions about the organisation of the proteins under investigation at the cell membrane are drawn.

Introduced next is a second particle tracking method which is highly efficient and capable of working with both 2D and 3D image data. This method uses a novel Haar-inspired feature for particle detection, drawing inspiration from the type of particles to be detected which are typically circular in 2D space and spherical in 3D image space. Trajectory linking in this method utilises a global nearest neighbour methodology incorporating both motion models to describe the motion of the particles under investigation and a further extended state space variable describing many more aspects of the particles to be linked. This method is validated using a variety of both 2D and 3D synthetic image data. The methods performance is compared with 14 other state-of-the-art methods showing it to be one of the best overall performing methods.

Finally, analysis tools to study a SR image restoration method developed by our research group, referred to as Translation Microscopy (TRAM) are investigated [1]. TRAM can be implemented on any standardised microscope and deliver an improvement in resolution of up to 7-fold. However, the results from TRAM and other SR imaging methods require specialised tools to validate and analyse them. Tools have been developed to validate that TRAM performs correctly using a specially designed ground truth. Furthermore, through analysis of results on a biological sample corroborate other published results based on the size of biological structures, showing again that TRAM performs as expected.

Dedication

For my family and friends without whom none of this would be possible.

We did it!

Acknowledgements

As is tradition I would like to start by acknowledging my supervisor's Dr Weiping Lu and Prof Rory. R. Duncan for their support and guidance throughout my time at Heriot-Watt University. I would also like to acknowledge the funding body, EPSRC, without whom I would not have been able to undertake the project.

I would also like to acknowledge my all the academics who gave me guidance throughout my project, in particular Dr Tina Howarth and Dr Paul Dalgarno. Also, Dr Vassilis Sboros for helping me find new application for my work.

To my friends and the whole of the PoBBBS community who I am particularly thankful to for making Heriot-Watt a fun and productive environment to come work.

Finally, to my family who stood by me and helped wherever possible throughout my PhD, even when I was being a nuisance and moaning for no good reason. I love you all and this is for you.

ACADEMIC REGISTRY
Research Thesis Submission

| | | | |
|----------|---|----------------|----------------------|
| Name: | Rhodri S. Wilson | | |
| School: | Institute of Biological Chemistry, Biophysics and Bioengineering, School of Engineering and Physical Sciences | | |
| Version: | Final | Degree Sought: | Doctor of Philosophy |

Declaration

In accordance with the appropriate regulations I hereby submit my thesis and I declare that:

- 1) the thesis embodies the results of my own work and has been composed by myself
- 2) where appropriate, I have made acknowledgement of the work of others and have made reference to work carried out in collaboration with other persons
- 3) the thesis is the correct version of the thesis for submission and is the same version as any electronic versions submitted*.
- 4) my thesis for the award referred to, deposited in the Heriot-Watt University Library, should be made available for loan or photocopying and be available via the Institutional Repository, subject to such conditions as the Librarian may require
- 5) I understand that as a student of the University I am required to abide by the Regulations of the University and to conform to its discipline.
- 6) I confirm that the thesis has been verified against plagiarism via an approved plagiarism detection application e.g. Turnitin.

* Please note that it is the responsibility of the candidate to ensure that the correct version of the thesis is submitted.

| | | | |
|-------------------------|--|-------|--|
| Signature of Candidate: | | Date: | |
|-------------------------|--|-------|--|

Submission

| | |
|---|--|
| Submitted By (<i>name in capitals</i>): | |
| Signature of Individual Submitting: | |
| Date Submitted: | |

For Completion in the Student Service Centre (SSC)

| | | | |
|--|--|-------|--|
| Received in the SSC by (<i>name in capitals</i>): | | | |
| Method of Submission (<i>Handed in to SSC; posted through internal/external mail</i>): | | | |
| E-thesis Submitted (mandatory for final theses) | | | |
| Signature: | | Date: | |

Table of Contents

| | |
|--|-----|
| Abstract | ii |
| Dedication | iii |
| Acknowledgements | iv |
| List of Abbreviations | 6 |
| List of Publications by the Candidate | 8 |
| Chapter 1 Introduction..... | 9 |
| 1.1 Motivation..... | 9 |
| 1.2 Quantitative analysis of microscopy | 11 |
| 1.2.1 Microscopy techniques | 11 |
| 1.2.1.1 Time-lapse microscopy | 11 |
| 1.2.1.2 Fluorescence microscopy..... | 11 |
| 1.2.1.3 Total internal reflection fluorescence microscopy (TIRFM) | 12 |
| 1.2.2 Super-Resolution Microscopy | 14 |
| 1.2.2.1 Photoactivated localisation microscopy..... | 15 |
| 1.2.2.1.1 Single particle tracking PALM..... | 16 |
| 1.2.3 Image processing tasks and challenges | 19 |
| 1.3 Approaches and contributions..... | 20 |
| 1.4 Structure of the thesis..... | 21 |
| Chapter 2 Review of Previous Literature | 22 |
| 2.1 Fluorescent particle detection | 22 |
| 2.1.1 Signal enhancement methods | 22 |
| 2.1.1.1 Laplacian of Gaussian Filter | 22 |
| 2.1.1.2 Multi-scale wavelets | 23 |
| 2.1.1.3 Opening filter | 24 |

| | |
|---|----|
| 2.1.1.4 H-dome transform | 24 |
| 2.1.1.5 Supervised learning method | 25 |
| 2.1.2 Particle segmentation methods | 25 |
| 2.1.3 Particle localisation methods | 26 |
| 2.1.3.1 Weighted Centre of mass..... | 26 |
| 2.1.3.2 Gaussian fitting | 27 |
| 2.1.3.3 Radial Symmetry | 28 |
| 2.2 Trajectory Linking..... | 28 |
| 2.2.1 Deterministic trajectory linking | 28 |
| 2.2.1.1 Local nearest neighbour..... | 29 |
| 2.2.1.2 Global nearest neighbour | 29 |
| 2.2.2 Probabilistic trajectory linking | 30 |
| 2.2.2.1 Bayesian state estimation | 30 |
| 2.2.2.2 The Kalman Filter | 31 |
| 2.2.2.3 Interacting multiple model Filter | 31 |
| 2.2.2.4 The Particle Filter | 32 |
| 2.2.2.5 Dynamic models..... | 32 |
| 2.2.2.6 Multiple Hypothesis Tracking | 33 |
| 2.3 Haar-like features..... | 33 |
| 2.3.1 Haar-like features for detection..... | 34 |
| 2.3.2 Twisted Haar-like Features | 34 |
| 2.3.3 Rotated Haar-like Features | 35 |
| 2.3.4 The Problem with Haar-like features | 36 |
| 2.4 Super-Resolution Microscopy | 37 |
| 2.5 Summary | 38 |

| | |
|---|----|
| Chapter 3 Single Particle Tracking in 2-Dimensional Microscopy Data | 40 |
| 3.1 Particle Detection..... | 40 |
| 3.1.1 Image Denoising..... | 41 |
| 3.1.2 Signal Enhancement..... | 42 |
| 3.1.2.1 Particle Probability Image Signal Enhancement | 42 |
| 3.1.3 Particle Segmentation | 46 |
| 3.1.3.1 Marker-Controlled Watershed Segmentation | 47 |
| 3.1.4 Particle Localisation | 50 |
| 3.2 Trajectory Linking..... | 51 |
| 3.2.1 Trajectory linking with IMM and Kalman filters | 52 |
| 3.2.1.1 State Space Variable | 52 |
| 3.3 Performance Evaluation on Synthetic Images | 55 |
| 3.3.1 Synthetic Datasets..... | 55 |
| 3.3.2 Comparison with State of the Art Methods..... | 56 |
| 3.3.3 Results | 58 |
| 3.4 Performance Evaluation on Real Microscopy Images..... | 65 |
| 3.4.1 Experimental Setup and Image Quality | 65 |
| 3.4.2 Comparison of Performance | 66 |
| 3.4.3 Results | 66 |
| 3.5 Summary | 68 |
| Chapter 4 Biological Applications | 69 |
| 4.1 Tracking of Single Molecules..... | 69 |
| 4.2 Experimental Setup..... | 69 |
| 4.3 Results | 70 |
| 4.3.1 Tracking of Single Molecules in Primary Cortical Neurons | 70 |

| | |
|---|----|
| 4.3.2 Tracking of Single Molecules in Neuroendocrine Cells | 71 |
| 4.4 Summary | 73 |
| Chapter 5 Particle Tracking 3-Dimensional Microscopy Data..... | 75 |
| 5.1 Particle Detection..... | 76 |
| 5.1.1 Signal Enhancement using a Novel Haar-Inspired Feature..... | 76 |
| 5.1.1.1 Signal Enhancement in 2D Image Data | 77 |
| 5.1.1.2 Signal enhancement in 3D image data | 80 |
| 5.1.2 Thresholding and Clump Splitting Segmentation | 81 |
| 5.1.2.1 Thresholding in 2D and 3D image space | 81 |
| 5.1.2.2 Clump splitting in 2D image space | 84 |
| 5.1.2.3 Clump splitting in 3D image space | 85 |
| 5.1.2.4 Choosing the correct clump splitting method | 85 |
| 5.1.3 Particle Localisation | 88 |
| 5.1.3.1 Localisation in 2D image data | 88 |
| 5.1.3.2 Localisation in 3D image data | 89 |
| 5.2 Trajectory Linking..... | 90 |
| 5.2.1 State space variable | 90 |
| 5.2.1.1 State space variable for 2D image data | 90 |
| 5.2.1.2 State space variable for 3D image data | 92 |
| 5.2.1.3 Weighting of state space variable..... | 93 |
| 5.2.2 Motion Modelling | 94 |
| 5.3 Performance Evaluation on Synthetic Images | 94 |
| 5.3.1 Synthetic Datasets..... | 95 |
| 5.3.2 Comparison with State of the Art Methods..... | 97 |
| 5.3.3 Results | 97 |

| | |
|---|-----|
| 5.4 Summary | 111 |
| Chapter 6 Super-Resolution | 113 |
| 6.2 Analysis to Validate TRAM | 114 |
| 6.3 Analysis of Application of TRAM | 118 |
| 6.4 Summary | 121 |
| Chapter 7 Conclusions..... | 122 |
| 7.1 Summary | 122 |
| 7.2 Further Work..... | 123 |
| Appendices..... | 125 |
| Appendix A: Chapter 3 tracking method user guide..... | 126 |
| References..... | 131 |

List of Abbreviations

| | |
|------------------|---|
| 1D | One-Dimensional |
| 2D | Two-Dimensional |
| 3D | Three-Dimensional |
| AFM | Atomic Force Microscopy |
| CLSM | Confocal Laser Scanning Microscope |
| DNA | Deoxyribonucleic Acid |
| dSTORM | Direct Stochastic Optical Reconstruction Microscopy |
| EGFP | Enhanced Green Fluorescent Protein |
| EMCCD | Electron Multiplying Charged Coupled Device |
| FN | False-Negative |
| FP | False-Positive |
| FPS | Frames Per Second |
| FWHM | Full Width at the Half Maximum |
| GT | Ground Truth |
| IMM | Interacting Multiple Models |
| ISBI | International Symposium on Biomedical Imaging |
| IUWT | Isotropic Undecimated Wavelet Transform |
| JSC | Jaccard Similarity Index (Track Points) |
| JSC ₀ | Jaccard Similarity Index (Tracks) |
| LDCV | Large Dense Core Vesicles |
| LoG | Laplacian of Gaussian |
| LSM | Light-Sheet Microscopy |
| MHT | Multiple Hypothesis Tracking |
| MPHD | Maximum Possible h-Dome |
| Munc18-1 | Mammalian Uncoordinated-18 |
| NLLS | Non-Linear Least Squares |
| PALM | Photoactivated Localisation Microscopy |
| PAmCherry | Photoactivatable Monomeric Cherry |
| PC12 | Rat Phaeochromocytoma |

| | |
|----------|---|
| PPI | Particle Probability Image |
| PSF | Point Spread Function |
| QD | Quantum Dot |
| QD-DO | Quantum Dot DNA Origami |
| RMSE | Root Mean Squared Error |
| sCMOS | Scientific Complementary Metal-Oxide-Semiconductor |
| SIM | Structured Illumination Microscopy |
| SMLM | Single Molecule Localisation Microscopy |
| SNAP-25 | Synaptosomal-Associated Protein 25 |
| SNR | Signal-to-Noise Ratio |
| SPIM | Single Plane Illumination Microscopy |
| spt-PALM | Single Particle Tracking Photoactivated Localisation Microscopy |
| SR | Super Resolution |
| STED | Stimulated Emission Depletion |
| STORM | Stochastic Optical Reconstruction Microscopy |
| TIRFM | Total Internal Reflection Fluorescence Microscopy |
| TP | True-Positive |
| TRAM | Translational Microscopy |

List of Publications by the Candidate

1. **Wilson RS**, Yang L, Dun AR, Smyth AM, Duncan RR, Rickman C, Lu W (2016) Automated single particle detection and tracking for large microscopy datasets. Royal Society Open Science 3:160225
2. Zhen Q*, **Wilson RS***, Liu Y, Dun AR, Saleeb R S, Liu D, Rickman C, Frame M, Duncan RR, Lu W (2016) Translation Microscopy (TRAM) for super-resolution imaging. Nature Scientific Reports 6:19993
3. Dun AR, Lord GJ, **Wilson RS**, Kavanagh DM, Cialowicz KI, Sugita S, Park S, Yang L, Smyth AM, Papadopulos A, Rickman C, Duncan RR (2017) Navigation through the Plasma Membrane Molecular Landscape Shapes Random Organelle Movement. Current Biology 27, 408-414
4. Kavanagh DM, Smyth AM, Martin KJ, Dun AR, Brown ER, Gordon S, Smillie KJ, Chamberlain LH, **Wilson RS**, Yang L, Lu W, Cousin MA, Rickman C, Duncan RR (2014) A molecular toggle after exocytosis sequesters the presynaptic syntaxin1a molecules involved in prior vesicle fusion. Nature Communications 5:5774

Chapter 1 Introduction

Introduced here is the motivation behind the work that contributes to this thesis, also included is an outline of microscopy techniques relevant to various sections of the work. Finally, in this short introduction, briefly outlined are contributions to the subject area and the approaches used to achieve these contributions as well as giving a description of the organisation of the Chapters contained within the thesis.

1.1 Motivation

Microscopy has become invaluable in the study of biological systems. However, the ability to acquire images of high quality is hindered by physical aspects of the imaging systems. Firstly, the achievable resolution of standard microscopy techniques are constrained by the diffraction limit as defined by Abbe [2], around 200-300 nm for the wavelengths of light typically used. However, modern so-called SR microscopy techniques utilise various methods to surpass the diffraction limit and achieve better resolution. Secondly, image quality is hampered by the presence of severe noise. This noise is typically mixed Poisson-Gaussian in nature, because of the short exposure times and fast readout times used to image the fluorophores and investigate the fast dynamics of the biological system.

Particle tracking is a crucial tool used for the analysis of the dynamics of particles in time-lapse fluorescence microscopy and is typically modelled as a two stage correspondence problem of particle detection followed by trajectory linking [3]. Particle detection requires particles within image data to be detected, segmented and localised with the highest possible accuracy, within all frames of a time-lapse image sequence. This is achieved using various image processing techniques. In trajectory linking, the detected particles are linked from frame-to-frame to form particle trajectories based mainly on the particles' location but other information regarding the appearance and motion of a particle can also be incorporated. However, the accuracy achieved in detection and localisation process and the

subsequent trajectory linking, are directly affected by the quality of the images used in the analysis. In live-cell microscopy there is always a compromise between the quality of the images that can be generated and the viability of the sample being investigated due to effects such as photo-toxicity. Furthermore, the fluorophores tagged to the particles of interest in the sample undergo an effect called photo-bleaching when imaged as they can only emit a given number of photons. These two factors, together with image acquisition at increasingly higher frame rates, result in images that are of low quality, that is of low-contrast and have a low-SNR.

The motivation behind the work presented in this thesis is to generate a particle tracking method with a robust particle detection framework that is capable of high accuracy in low quality image data, such as those found in live-cell fluorescent biological imaging applications, and a trajectory linking method that is not only accurate but also computationally efficient. Achieving high detection accuracy at low quality image data allows more reliable measurements to be taken from the particles, which in turn would improve the accuracy of the trajectory linking process. Furthermore, the analysis of these particle trajectories, that can be imaged over a longer period of time and/or at a high framerate dependent on the requirement of the biological application being investigated, is more accurate and as such the conclusions drawn from the analysis is more reliable. Furthermore, achieving high accuracy in low quality images would allow for more controlled doses of light to be used whilst imaging the particles and therefore minimizing the photo-toxic effect which may affect the behaviour of the particles being investigated. In addition to accurate particle detection, the tracking method should be able to tackle the traditional particle tracking challenges of 3D image data, as biological processes occur in 3D space and dynamical processes may be missed if they are above or below the 2D image plane being investigated. Secondly, the tracking method should be able to accurately tackle the challenge of high density particle fields so that reliable statistics about the process being investigated can be calculated.

Finally, with SR microscopy methods becoming more commonly used the techniques needed to validate and analyse the data produced by these methods are becoming more important. Validation and analysis tools are required that are able to show that the

improvement of resolution generated by these methods is consistent with the theory of what the method or device can generate.

1.2 Quantitative analysis of microscopy

1.2.1 Microscopy techniques

This section provides an overview of the basic principles of the microscopy techniques used in different studies throughout this thesis. Each of these techniques utilises a different method of sample illumination and detection, it is therefore important to ensure that when choosing which microscopy technique to utilise that it complements the biological process being investigated.

1.2.1.1 Time-lapse microscopy

Time-lapse microscopy is a tool for observing biological changes over time and is achieved by taking consecutive images of the same region within a sample, at an imaging frame-rate, which is tailored to the biological process being investigated. This can be on the scale of milliseconds for processes such as single molecule dynamics to minutes or hours for processes such as embryo development. Time-lapse microscopy can be used in combination with most other microscopy techniques and is more dependent on sample preparation than the hardware utilised, i.e. the sample must be live and not fixed.

1.2.1.2 Fluorescence microscopy

Fluorescence microscopy utilises the fluorescence property of photon emission which occurs in molecules called fluorophores. These fluorophores are tagged to the particles and

structures that are to be investigated [4,5]. Fluorescence works on the principle that when a fluorophore is illuminated with light of specific wavelength, an electron within the fluorophore will absorb energy from the light and transition from a ground state, S_0 , to an excited state, S_2 (Figure 1.1 blue arrow). Over time (fluorescence lifetime, τ) the excited electron transitions to a lower excited state, S_1 (Figure 1.1 yellow arrow). Photon emission occurs as the electron cannot maintain enough energy to reside in any of the excited states and so returns to its initial ground energy state, S_0 (Figure 1.1 green arrow). These emitted photons are collected by the detector of the imaging system to form an image. Typically, filters will be implemented to eliminate light of unwanted wavelengths being collected. Fluorescence microscopy is a pre-requisite for many other microscopy techniques such as laser scanning and spinning-disk confocal microscopy [6,7], TIRFM [8] and SR techniques such as PALM [9], STED microscopy [10], SIM [11] and SPIM or LSM [12].

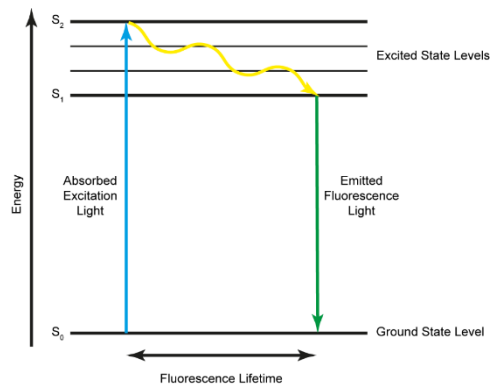


Figure 1.1: Jablonski diagram illustrating the changes in energy state levels undergone by an electron in fluorescence emission. The blue arrow represents absorption of energy from the excitation light source transitioning the electron from its ground energy state level S_0 into an excited state S_2 . Yellow arrow representing the relaxation of the electron over the fluorescence lifetime into a lower excited state S_1 . Finally, the green arrow represents the transition of the electron back to its ground state energy level, this is when fluorescent emission occurs.

1.2.1.3 Total internal reflection fluorescence microscopy (TIRFM)

TIRFM is a technique that has been used extensively for imaging at the cell surface where many of the cell processes that are of interest to scientific community transpire [13]. TIRFM is essentially a specialised method of illuminating a sample which limits the depth of fluorescence excitation into the cell to the order of 100-200 nm from section of the cell

membrane in contact with the coverslip, with the intensity of the fluorescence characterised as an exponentially decaying evanescent field. In using TIRFM a fluorophore that resides deeper within the cell is less likely to be excited and thus the amount of light originating from out of focus image planes collected by the detector is reduced. The most common method of creating an evanescent field in TIRFM is the so-called “through-the-objective” method (Figure 1.2). In this method the excitation illumination is directed into the periphery of a high numerical aperture objective lens so that upon reaching the coverslip-sample boundary it has a sufficiently high angle to achieve total internal reflection [8].

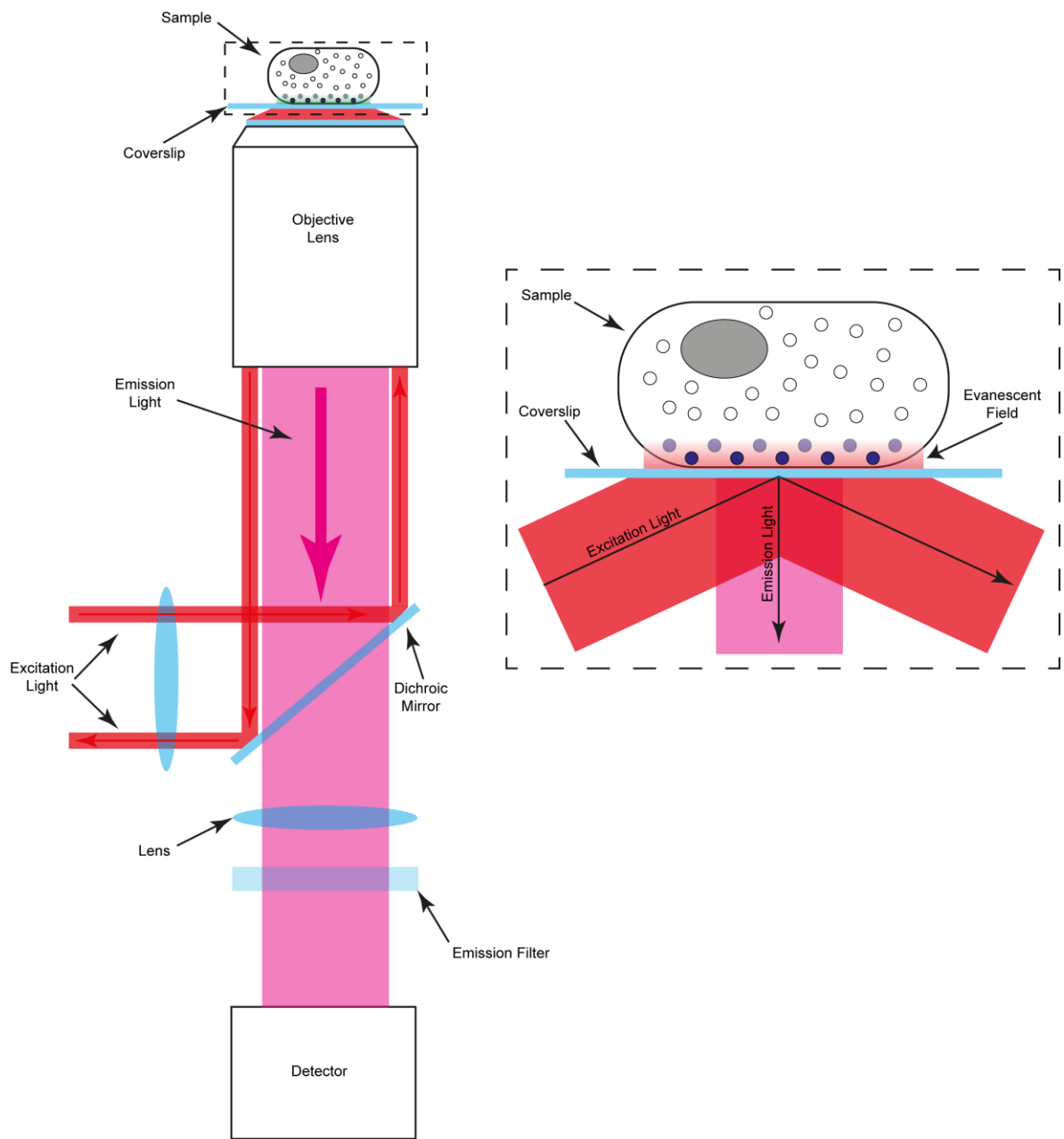


Figure 1.2 TIRFM Schematic. The schematic displays the “through-the-objective” method of achieving TIRF evanescent illumination field. Excitation light is directed through the periphery of the objective lens at an angle to achieve TIRF. Emission light is collected in the detector after passing through a dichroic mirror, lens and filter.

1.2.2 Super-Resolution Microscopy

SR is the term used to describe microscopy techniques that are able to surpass the resolution limit as described by Ernst Abbe’s equation [2].

1.2.2.1 Photoactivated localisation microscopy

PALM is a SMLM SR microscopy technique that surpasses the diffraction limit through the use of photoswitchable fluorophores [9]. It is conceptually almost identical to another SR microscopy technique, STORM [14], with the two methods only differing in their method of fluorophore photoswitching. As with other SR SMLM methods [15], PALM uses repeated cycles of laser-based fluorophore activation, localisation and bleaching to temporally separate single molecules within a sample (Figure 1.3). This temporal separation allows the molecules to be localised with an accuracy an order of magnitude higher than conventional diffraction limited optical microscopy methods [16]. To acquire PALM image data there are two essential requirements: the sample must be labelled with photoswitchable or photoconvertible fluorophores and at least two wavelengths of laser light should be available on the microscope for the activation and imaging of the fluorophores. Demands on the specification of the wavelength of the laser light used is entirely dependent upon the fluorophores used in labelling the sample. Typically, the lasers used are low power continuous wave lasers as to limit damage to the sample during imaging and allow longer acquisition times. Localisation and reconstruction of a SR image from a sequence of PALM images is typically post acquisition process, although some state-of-the-art localisation software's claim to be capable of localisation and reconstruction in real-time [17,18].

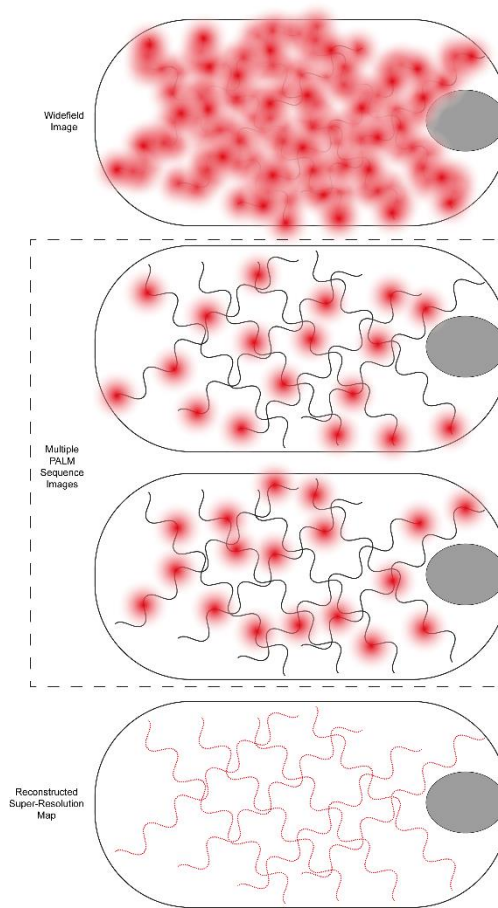


Figure 1.3 PALM Schematic. Top – Schematic of a densely labelled widefield with no visible structures due to the diffraction limit. Middle – Schematic of PALM sequence image where the density of fluorophores is low in each image and as such can be localised with a high accuracy. Bottom – Schematic of a reconstructed SR map with previously unresolved structures clearly identified.

1.2.2.1.1 Single particle tracking PALM

The use PALM for single particle tracking is favourable as, by design, the density of particles within PALM images is low, which is favourable for particle detection and trajectory linking. Different to standard PALM experiments, which in common with many other SR methods is usually performed in fixed cells, spt-PALM is a live-cell microscopy technique used to study the dynamics of single particles [19]. In spt-PALM the fluorophore labelled particles are activated and imaged over time, as in time-lapse microscopy. During the imaging process the fluorophores attached to the particles bleach until they are unable to emit any more photons. This activation, imaging and bleaching cycle is repeated many times, typically until

there are no more fluorophores to activate (Figure 1.4). Here the amount (power of the laser) of illumination used in the imaging is key. High doses of illumination will result in the particles being easier to localise but will also have the counter effect of bleaching them more quickly so they cannot be imaged for as long. Higher doses of illumination also make the cell more susceptible to phototoxic effects. Conversely, lower doses of illumination allow for longer imaging of a sample but results in images that are of a low quality and hence make the task of localisation more difficult. The ability of an algorithm to analyse the data generated by these experiments greatly impacts on what biological questions can be investigated and in what detail.

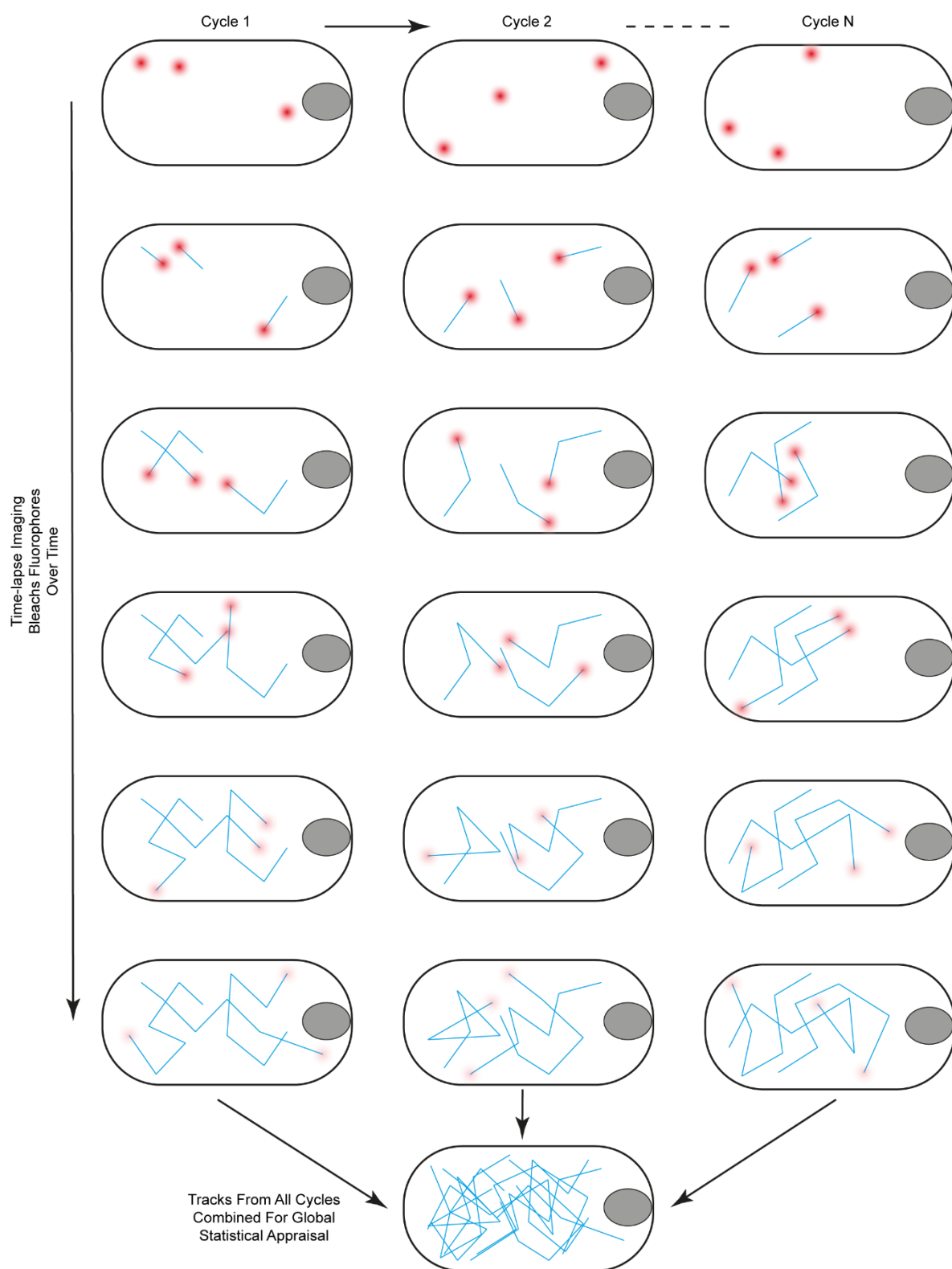


Figure 1.4 spt-PALM Schematic. Columns represents cycles of repeated activation, imaging and bleaching of fluorophores conjugated to the particles of interest. During each cycle the fluorophores are imaged for tracking, typically post acquisition. Finally, all tracks from all cycles are combined for analysis and statistical appraisal.

1.2.3 Image processing tasks and challenges

As discussed in section 1.1 particle tracking is a crucial tool used for the analysis of the dynamics of particles in time-lapse fluorescence microscopy. As such, the aim of the work presented in this thesis is to be able to track and investigate the dynamics and behaviours of all particles. The tasks required to accurately achieve the tracking of single particles can be split into two main components; particle detection and trajectory linking. For these components to be achieved accurately particle tracking methods typically rely upon the pixel based intensity information provided in each image, as prior knowledge about the systems being investigated is generally limited. However, since this pixel based information is susceptible to corruption by noise emanating from multiple sources, it affects the achievable accuracy of a particle tracking method. The task of particle detection can be described as three main processes; signal enhancement, segmentation and localisation. However, this task is typically hampered by the particles being investigated being of small size (covering only a few pixels) and of low-contrast, when compared to their surrounding the area. To obtain accurate particle detection the signal originating from the particles must first be enhanced, this is typically achieved through the use of various image filters. Segmentation normally takes the form of thresholding or watershed techniques. However, these techniques are strongly affected by the SNR of the images under investigation. Finally, determining a particle localisation through centre-of-mass is directly affected by the accuracy of the particle segmentation process. 2D Gaussian fitting methods for localisation can provide better accuracy but at much greater computational cost. The detected particles must next be linked through the sequence of images to form particle trajectories. The accuracy of the final trajectories is determined by the accuracy of the measurements extracted from the detected particles and a methods ability to link them correctly. These trajectories are then used for statistical analysis to determine the individual and global dynamics of the particles being investigated. The accuracy of the generated trajectories directly impacts on the accuracy and reliability of the statistical measures extracted describing the particles dynamics. Thus, to draw accurate conclusions accurate trajectory linking is required. The tasks of particle detection, trajectory linking and trajectory analysis

are not trivial ones, which is why consideration should always be given to the variable factors of the imaging technique used to acquire the data that is to be analysed, ideally tailoring the processing and analysis to the data under investigation. Furthermore, it is possible that errors generated in the detection process can propagate throughout the entire tracking method, therefore it can be said that accuracy in particle detection is the most important attribute for a particle tracking method to be effective.

1.3 Approaches and contributions

The focus of the work presented in this thesis is on the development of two particle tracking methods capable of working in complex live-cell imaging environments of low-SNR and low-contrast. Specific attention has been given to the development of the two particle detection algorithms within the tracking methods that are able to work with image data of all dimensionality. The algorithms implement novel signal enhancement techniques and robust segmentation processes thus allowing them to achieve the high accuracy required live-cell microscopy environments. Trajectory linking in both particle tracking methods is achieved using a variety of so-called “particle features” to better describe the current state of the system being investigated and thus allowing for more accurate trajectory linking in dense particle fields. Both trajectory linking processes work in different way with the second trajectory linking method being able to link trajectories much more efficiently and in 3D image space. Although the imaging technologies to achieve “true” 3D time-lapse imaging are currently under development they typically require specialised equipment and complex implementations. However, as these technologies become more readily available to the wider scientific community, it will be essential that the tools to analyse the data generated by these technologies are ready. Finally, new methods for the validation and analysis of the TRAM SR technique are developed, thus allowing the confirmation of observations previously only seen using specialised and expensive SR hardware.

1.4 Structure of the thesis

The structure of the thesis is as follows. Chapter 2 reviews the existing techniques for particle detection and trajectory linking as well as reviewing the use of Haar-like features for general objection detection. Also provided is a brief overview of existing SR microscopy techniques. Chapter 3 describes the first of two particle tracking methods, which utilises signal enhancement through filtering with Haar-like features for improved particle detection. Trajectory linking in this method is achieved through the use of three Kalman filters within an IMM filter with an extended state space variable. This method is fully validated using both synthetic and experimentally collected image data. Chapter 4 describes the implementation of the particle tracking method described in Chapter 3 to investigate various biological applications. Chapter 5 describes the second particle tracking method capable of working in 3D image space. Here signal enhancement for particle detection is achieved through a novel filtering method using a novel Haar-inspired feature. Trajectory linking is achieved using a global nearest neighbour method with motion models and incorporating many more features describing each particle extracted in the particle detection process. The performance of this tracking method is fully validated using both 2D and 3D synthetic image data. Chapter 6 focuses on the validation and analysis of a new SR microscopy technique called TRAM. Finally, Chapter 7 highlights the main conclusions that can be drawn from the work as a whole and the scope for further development of the methods.

Chapter 2 Review of Previous Literature

This Chapter reviews the current methods and techniques that exist for the detection of fluorescent particles in microscopy image and the subsequent linking of these detections to form trajectories. A further review of methods using Haar-like features for detection applications, not just the detection of fluorescent particles in microscopy images, is also given as the new techniques presented in Chapters 3 and 5 of this thesis are derived from these concepts. Finally, a brief overview of SR methods is given relating to our developed presented in Chapter 6.

2.1 Fluorescent particle detection

As discussed in Chapter 1 particle detection is typically split into a three stage procedure of signal enhancement followed by particle segmentation before particle localisation. Techniques associated with all three of these processes are reviewed here.

2.1.1 Signal enhancement methods

There exist many different methods for signal enhancement of fluorescent particles in microscopy images. These enhancement methods can generally be classed as belonging to one of the following subsets of methods: filtering, wavelet analysis, morphological analysis or patch-based analysis. Presented here is a discussion of various methods that achieve signal enhancement in one of these ways.

2.1.1.1 Laplacian of Gaussian Filter

Also known as the spot enhancing filter the LoG filter is a filter used for the detection of fluorescent spots [20]. A conceptually simple method the LoG kernel is first convolved with the input image to enhance the signal emanating from spot like features so that a global threshold, T , can be applied to the result. T is defined using a combination of the mean and standard deviation of the convolved image along with a user defined factor to compensate for the amount of noise in the image [21]. The size (width) of the LoG kernel, κ_{LoG} , is defined by its standard deviation, σ :

$$\kappa_{LoG}(x, y) = \left(\frac{x^2}{\sigma_{xy}^4} - \frac{1}{\sigma_{xy}^2} + \frac{y^2}{\sigma_{xy}^4} - \frac{1}{\sigma_{xy}^2} \right) \cdot \kappa_G(x, y) \quad (2.1)$$

Where κ_G is a 2D Gaussian kernel defined as:

$$\kappa_G(x, y) = \frac{e^{-\frac{(x^2+y^2)}{2\sigma_{xy}^2}}}{2\pi\sigma_{xy}} \quad (2.2)$$

Here the value of σ must be chosen carefully and relates to the size of the particles to be detected, if too large a value is chosen the filter will over smooth the image and particles will be lost. If too small a value is chosen, the LoG filter will enhance noise within the image resulting in false detections.

2.1.1.2 Multi-scale wavelets

The IUWT utilises the fact that adjacent wavelet planes of the transform display high levels of correlation [22]. It is particularly suited to for the detection of fluorescent particles in biological images as they manifest as isotropic features with no definite edges [23]. The IUWT works by decomposing the input image in to wavelet planes, w_i , and approximated images, a_i , which are analysed using the a-trous algorithm where $i = 1, 2 \dots N$ and N is the number of wavelets to be computed. An approximated image is generated by convolving the original image with a low-pass filter, h_i . The associated wavelet plane is generated by

subtracting the new approximated image from the previous approximated image (and the original approximated image, a_0 , takes the form of the input image). The final construction of an image using the IUWT takes the form of:

$$a_0 = a_N + \sum_{i=1}^N w_i \quad (2.3)$$

However, when the task is to detect particles not restore an image, detection is achieved by first calculating the point-wise product of the wavelet planes that provide the best response relating to the size of particles. This process generates a so-called correlation image in which the signal from particles appears enhanced and a threshold assuming a Gaussian noise model can be applied to detect particles.

2.1.1.3 Opening filter

Using the morphological opening operator, the opening filter aims to separate particles of a given size from the image background [24]. The opening operator is first applied to a noise reduced version of the image, achieved through convolution with a Gaussian kernel, using a disk structuring element. The length of the radius of the structuring element should radius of the particles to be detected. The generated “open image” will contain disk shaped flat regions of high pixel values relating to regions in the input image containing disk like particle features smaller than the radius of the disk structuring element. This open image is then subtracted from the noise reduced image and thus only leaves features with pixel values greater than the flat regions. Using the opening filter requires accurate identification of the size of the radius of the particles to be detected and is not very reliable for detecting particles of varying size in the same image [25].

2.1.1.4 H-dome transform

The h-dome transform is most effectively implemented on images that have been pre-processed with the LoG filter and utilises morphological reconstruction to identify and cut off “dome-like” structures with a specified peak intensity “height” resulting in a so-called dome image [26]. The dome image consists of regions which are made up of spatially connected pixels of the same height, however not all of these regions will relate to particles that are to be detected. To identify true particle regions further cluster analysis is performed on the dome image as well as importance sampling schemes to analyse the properties of each of the regions. However, as the performance of the method is directly linked to the selected height value, which in turn is linked to SNR of the input image, the h-dome transform is not especially suit for applications where the SNR of the image may vary within different regions of the image. Extensions of this method such as the MPHD transform seek to apply a range of height values to an image as to overcome the varying SNR limitation [27].

2.1.1.5 Supervised learning method

Supervised learning methods employ pattern recognition techniques to identify particles of interested in an image. These techniques require prior training of the method with data that contains particles with characteristics similar to the particles to be detected. Methods proposed for particle detection in fluorescence microscopy perform extremely well when compared to the other methods discussed here in term of both accuracy and input parameter tolerance [25]. However, as training such methods require manual identification of the so-called GT features in a large number of images their application to images of low-SNR is not reliable as the GT cannot be accurately identified in these images. Furthermore, as particle characteristics can change from dataset to dataset the detection method would need to be trained each time it is applied to a different dataset.

2.1.2 Particle segmentation methods

The simplest method for particle segmentation is to apply a global threshold to a signal enhanced image. In the resultant binary image, a particle will appear as a region of spatially connected “on” (white) pixels. If particles are well separated, then it can be assumed that each region of the binary image only contains one particle. The size and morphology of the regions can also be used to filter out errors due to noise and other factors. However, when particle density is high the regions will generally appear to be larger and hence contain multiple “clumped” particles. Further segmentation of these regions is required to identify single particles for accurate trajectory linking. Due to the particles of interest being of small size, classical watershed methods using the distance transform do not perform well. Suggested methodologies to overcome this include performing the watershed transform on a denoised version of the input image, in this case each clumped region is split depending on the number of local maxima within it [28,29]. Another suggested method includes the splitting of these clumped regions using the k-means clustering algorithm [30]. However, this has the prerequisite that the number of particles within a clumped region is known.

A more advanced segmentation method, capable of localising the segmented particles simultaneously, describes utilising the fact that the particles of interest are typically of sub-resolution size and thus manifest in the image as Airy distributions which can be approximate to Gaussian distributions [31]. As such, the method attempts to fit an increasing number of mixed Gaussian models to the grayscale information within a region containing clumped particles. The number and location of the particles within each region is determined as the mixed Gaussian model that gives the best fit to the grayscale information. Although elegant this method is very computationally expensive. Furthermore, as it is only compatible with sub-resolution particles and would not be applicable to all applications.

2.1.3 Particle localisation methods

2.1.3.1 *Weighted Centre of mass*

Due to its simplistic nature weighted centre of mass is one of the popular localisation methods used throughout the particle tracking literature [21,22,32–35]. Assuming that the particles of interest are symmetric, weighted centre of mass is a computationally efficient method for providing localisation with sub-pixel accuracy. In 2D image data the weighted centre mass is calculated as:

$$\begin{bmatrix} x_c \\ y_c \end{bmatrix} = \frac{\sum_{i,j \in R} \begin{bmatrix} x_i \\ y_j \end{bmatrix} I(i,j)}{\sum_{i,j \in R} I(i,j)} \quad (2.4)$$

Where, x_c and y_c are the calculated sub-pixels localisations of the centre of mass, i and j are the x and y indices of all pixels within the segmented region R within the image I . This method is also easily extendable to 3D localisation if required.

2.1.3.2 Gaussian fitting

It has been shown that fitting a model that best describes the PSF of the imaging method used can yield very high localisation accuracy. Although the models to describing the PSF are typically well characterised they can be very complex, as such they cannot be fitting easily and become computationally expensive to use. However, it has been shown that using a generalised Gaussian model to approximate the PSF of an imaging method can be used to achieve accurate localisation in many different particle tracking applications [36]. As long as the signal within the image is great enough, and the particles to be localised are sub-resolution it has been shown that Gaussian fitting methods provide greater localisation accuracy than weighted centre of mass methods [37]. However, as the Gaussian model is an approximation of the PSF of the imaging system using it for particles above the resolution limit is not possible. Furthermore, Gaussian fitting methods are susceptible to noise within an image and computationally expensive as such they are not well suited to more complex image environments or applications with high particle density [37].

2.1.3.3 Radial Symmetry

A newly developed method, radial symmetry aims to utilise the symmetric nature of particles that are to be localised [38]. The method uses radial lines to estimate the centre of a rotation symmetric distribution. As the method is not iterative it is computationally efficient and has been shown to provide localisation accuracy similar to that of Gaussian fitting methods. However, as with Gaussian fitting methods it can typically only be applied for localising particles which are of sub-resolution.

2.2 Trajectory Linking

Trajectory linking methods typically fall into one of two categories; “deterministic” or “probabilistic”. Deterministic approaches use the particle localisations from the detection process and an assessment of their distance and/or features to assign a score relating to their suitability for linking with another detection. Probabilistic methods require the incorporation of prior knowledge about the particles under investigation to try and estimate the particles “true” trajectory from the available information. Both concepts are reviewed below.

2.2.1 Deterministic trajectory linking

Deterministic trajectory linking methods are often referred to as “joint-the-dots” methods. Given a set of particle detections a deterministic method will aim to determine correspondences between detections present in adjacent frames of a time-lapse image sequence. Along with particle location deterministic methods will utilise other measured features to define a “distance” between detections in consecutive frames. Typically, the squared distance, d^2 , is utilised with the distance between the particle detection at time point t_n and the particle detection at time point t_{n+1} being defined as:

$$d^2 = \sum_{f=1}^{N_f} \alpha_f (\mathbf{x}_f(t_n) - \mathbf{x}_f(t_{n+1}))^2$$

(2.6)

Where \mathbf{x}_f is a vector containing N_f feature measurements describing the particle detection and α_f is a weighting factor to scale the feature measurement dependant its unit of measurement and importance to the trajectory linking process [39].

2.2.1.1 Local nearest neighbour

A simple method for determining particle correspondences, local nearest neighbour links detections into trajectories by simply searching for the minimum distance between two detections at two consecutive time points. To eliminate impossible trajectory links the search for possible links is limited to a search radius defined using some prior knowledge describing the speed of the particles of interest. Trajectories are updated from frame to frame with a trajectory being terminated if no detections are found within the search radius. Thresholds can also be applied to the value of d so that incorrect links can be avoided even if they are within the defined search radius.

Implementations of this style of trajectory linking are described in [40,41]. With a different linking philosophy described in [42], here trajectories are individually built up over time, with the detection being used in the trajectory being removed from the set detections for that time point. The authors claim improved performance using this method with results similar to that of the global nearest neighbour method described below.

2.2.1.2 Global nearest neighbour

Local nearest neighbour methods only perform accurately when the closest measurement in the next time point is the detection to be linked to. This limits the application of these

methods to scenarios where the particles are of low density and are spaced far from each other. Global nearest neighbour methods aim to find the globally optimal solution in which the sum of all distances between linked detections is minimised. To do this a cost matrix is defined describing all possible links between two sets of detections and the goal is to find the optimum pairing that generates the minimum cost.

Many tracking methods exist using the global nearest method, these methods include using graph theory to minimise [32] the global distance, dynamic programming to solve the assignment problem [43] as well as a two-pass approach to form tracklets and then combine these tracklets into trajectories [31]. A more recent implementation also utilises Kalman filters for particle state predication [44].

2.2.2 Probabilistic trajectory linking

Probabilistic trajectory linking methods do not search for direct correspondences from time point to time point, instead they aim to estimate a particles true trajectory using motion models and characteristics from the detection measurements. However, these methods require some prior knowledge of the system under investigation, this information is used to better predict the true state of particles at future time points.

2.2.2.1 Bayesian state estimation

Utilising a Bayesian framework for trajectory linking involves constantly updating the posterior probability density function which implies the certainty of the state of a set of particles at a given time. Bayesian estimation relies on inferring information about the behaviour of the particles given a set of measurements. A time evolving model is required to describe the change in the state in adjacent time frames, and a measurement model to relate the state of an object to the measurement from the data. The posterior probability density function is iterative estimated for each time frame. This is followed by an update for the current time frame by applying Bayes' theorem.

Typically, Bayesian estimation is too computationally expensive to be used for particle tracking applications but the Kalman filter, described below, can be used as an analytical solution if the system under investigation is known to be both linear-Gaussian.

2.2.2.2 The Kalman Filter

If the system under investigation is known to be undergoing a linear-Gaussian process such as diffusion, then the Kalman filter can be utilised as an efficient analytical variant of Bayesian state estimation. The Kalman filter assumes that the real state of a system can be described as its previous state after undergoing some transition with noise. The noise within the system is assumed to be of a Gaussian distribution with zero mean. The noise covariance matrix of the process defines the variation in the state space variables from a linear state evolution between consecutive time frames.

The Kalman filter has been extensively used in the tracking of single particles [21,45,46], showing improved performance over deterministic methods. However, in very low-SNR environments improved data association is required to achieve better performance equivalent to that of more advanced filtering techniques.

2.2.2.3 Interacting multiple model Filter

For optimal trajectory linking with the Kalman filter required the correct model of motion for the particles being investigated to be selected. As each Kalman filter is only capable of modelling one particle motion it is therefore not suited for most tracking applications in which particles of interest can display a multitude of different motions. Furthermore, only using one model of motion may bias the trajectory linking process and the analysis of the results. The IMM filter is a solution to this, within the IMM filter it is possible to incorporate multiple Kalman filters each modelling a different type of particle motion [47,48]. Since the proposed use of the IMM for single particle tracking [49] it has become increasingly more

popular and has been used in many different tracking methods because of its ability to cope with multiple motion models [29,50,51].

2.2.2.4 The Particle Filter

When the particles under investigation do not follow a linear- Gaussian system the particle filters offer a numerical approach for solving the estimation problem [52]. The posterior density function is represented by a set of individually weighted random examples. Prediction of the state in the adjacent time frame is performed by propagating new random examples taken from a proposal distribution, which is typically chosen to be a dynamic model.

The use of particles filters has been shown to provide superior accuracy in trajectory linking when compared to the Kalman filter and deterministic methods previously mentioned here [21]. As with the IMM filter, multiple models of particle behaviour can be modelled with multiple particle filters [53]. However, the computation cost associated with particle filters increasing with the number of particles to be tracked, as such they are not suggested for application where the number of particles to be tracked is high.

2.2.2.5 Dynamic models

As with Kalman filters the particle filter will only perform accurately when the motion of the particles being investigated is modelled accurately. Typically, the particles investigated will undergo one of two models of motions: Brownian motion, relating to simple diffusion of the particles or directed motion, relating to directed transport via motor proteins i.e. along microtubules. Whilst Brownian motion can simply be modelled as a random walk process [46,50,54,55] directed motion requires more sophisticated modelling for example as a constant speed model [26,50,56], linear-Gaussian model [54] or a combination of first order and second order linear extrapolation models [55].

2.2.2.6 Multiple Hypothesis Tracking

MHT is a multi-frame trajectory linking method in that it not only looks to make trajectory links on a frame by frame basis but on the likelihood of a trajectory given multiple future links (hypotheses). The two main methodologies for MHT revolve around forming trajectories either based on a prior hypothesis [57] or around the prior trajectory [58]. However, these multi-frame filtering approaches are extremely computationally expensive and are not suited for tracking applications with many frame or many particles. Relative improvement in the efficiency of the MHT has been made by sharing the computational load through the implementation of parallel processing [51,59].

2.3 Haar-like features

Haar-like features are so named due to their similarity to the Haar wavelet derived by Alfred Haar in 1909 [60] (Figure 2.1a). Although Haar did not originally use the term wavelet, as the field of wavelet analysis had not yet been conceived, is now recognised to be the first, as well as the simplest, wavelet basis. The Haar wavelet is a 1D square-shaped function that can be rescaled as needed (Figure 2.1b).

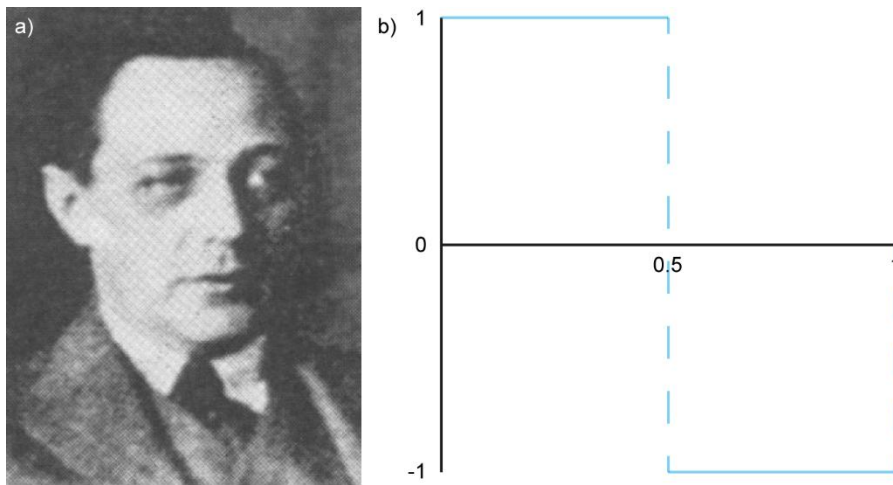


Figure 2.1: Alfred Haar and his Wavelet. a) Photograph of Alfred Haar taken around 1928. b) The original Haar wavelet designed in 1909, a square 1D function.

2.3.1 Haar-like features for detection

From this 1D square-shaped function an extension to 2D space was explored with an application in the analysis of images [61]. Further investigation into the use of 2D Haar filters for detection resulted in the term Haar-like features being developed [62]. The work showed that these Haar-like features could be effective when applied to the challenge of face detection; this is due to the face being able to be simply represented as a combination of adjacent light and dark areas. In this application, a set of four simple Haar-like features were implemented and resulted in rapid object detection (Figure 2.2). Whilst noting that this limited set of features is not as sensitive as other filters that were available at the time and could only identify edges in the orientations of the features used this was compensated by the relative computational efficiency of the method.

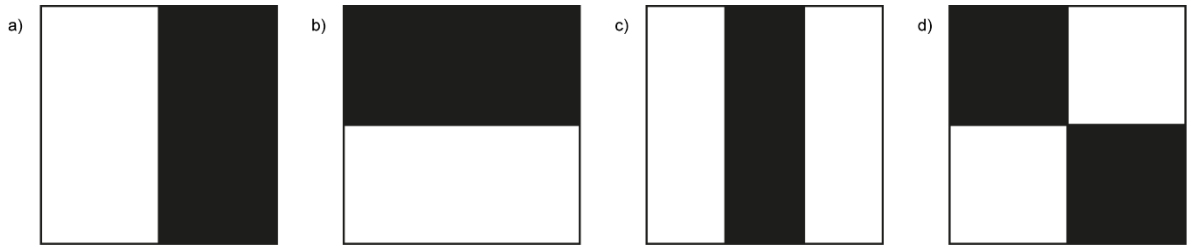


Figure 2.2: Library of Haar-like features used by Viola and Jones in their rapid object detection framework [62]. a) The Haar-like feature used to identify vertical edges. b) The Haar-like feature used to identify horizontal edges. c) The Haar-like feature used to identify vertical stripe like features. d) The Haar-like feature used to identify diagonal line like features.

2.3.2 Twisted Haar-like Features

A proposed extended set of Haar-like feature for object detection building on the original work included an efficient set of 45° “twisted” (rotated) features (Figure 2.2) [63]. In this application, the previously special diagonal line feature is eliminated (Figure 2.2j) as diagonal edges could now be identified by twisted features (Figure 2.2c, d, f and g). Finally, a surround feature was also included to identify dark areas completely surrounded by lighter areas (Figure 2.2h and i). Although, the computational time of the method was

relatively unaffected by the use of an extended set of features this was more likely due to the computational hardware utilised being more powerful than the method being equally or less complex. Nevertheless, increasing the complexity of the set of features used within the detection algorithm did give an overall improvement to the accuracy of the method.

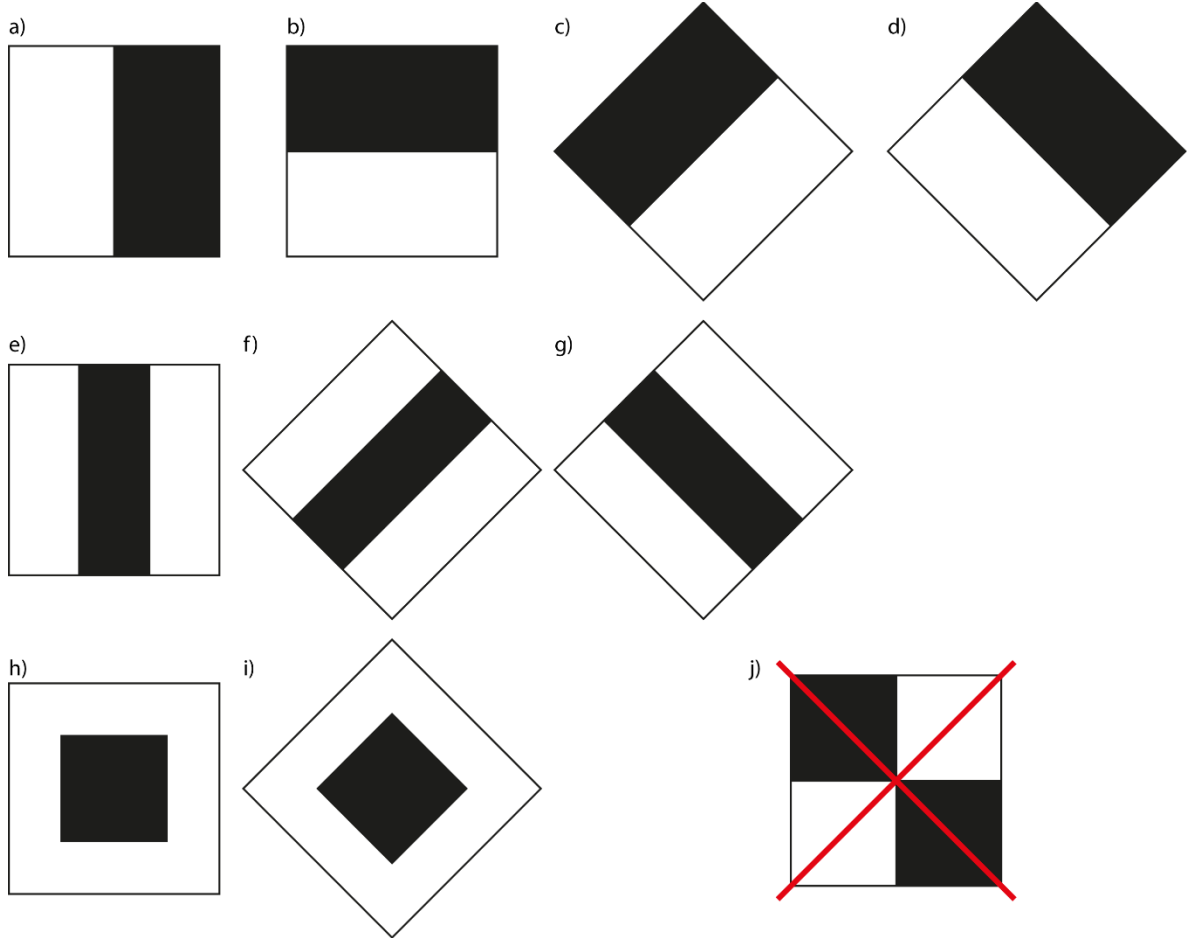


Figure 2.3: Library of twisted Haar-like features used by Lienhart and Maydt in their rapid object detection framework [63]. Features a), b) and e) are the same as used by Viola and Jones in [62] for identifying vertical edges, horizontal edges and vertical stripes, respectively. c), d), f) and g) are the new twisted features that are now capable of identifying diagonal edges and lines. h) A new surround feature introduced by Lienhart and Maydt. i) The 45° twisted counterpart of the new surround feature. j) The diagonal line feature used by Viola and Jones but is no longer needed due to the inclusion of twisted features.

2.3.3 Rotated Haar-like Features

Again increasing the complexity of the set of features used by extending the idea of twisted Haar-like features to include integer rotated Haar-like features showed an improvement in

the detection accuracy achieved using these filters [64]. Here the angle of rotation of any Haar-like feature is defined as an integer rotation, θ , where $\theta = \tan^{-1}(A/B)$ where A and B are both integer. A further subset of integer rotations, called unit-integer rotations, was defined where either A , B or both is equal to 1, here the twisted Haar-like features can be defined by the integer rotation $\theta = \tan^{-1}(1/1)$. Table 2.1 gives a sample list of unit-integer rotation angles. Whilst the original implementation of Haar-like features was capable of identifying targets rotated up to $\pm 20^\circ$ it is stated that the proposed set of unit-integer rotated features should be more than capable of identifying targets of any orientation as the difference between any two consecutive unit-integer rotations is always less than this initially proposed 20° limit.

Table 2.1: Example of some unit-integer rotations used in [64]. Each angle is defined as $\theta = \tan^{-1}(A/B)$ where either A or B or both are equal to one 1 and the other value is also integer.

| Integer Rotation | Angle | Integer Rotation | Angle |
|------------------|--------|------------------|--------|
| 1-1 | 45.00° | 1-1 | 45.00° |
| 2-1 | 63.43° | 1-2 | 26.57° |
| 3-1 | 71.57° | 1-3 | 18.43° |
| 4-1 | 75.96° | 1-4 | 14.04° |
| 5-1 | 78.69° | 1-5 | 11.31° |
| 6-1 | 80.54° | 1-6 | 09.46° |
| 7-1 | 81.87° | 1-7 | 08.13° |
| 8-1 | 82.87° | 1-8 | 07.13° |
| 9-1 | 83.66° | 1-9 | 06.34° |
| 10-1 | 84.29° | 1-10 | 05.71° |

2.3.4 The Problem with Haar-like features

The use of Haar-like features by constantly extending the feature library used presents problems on two fronts. Firstly, although the theory behind the use of rotated features of any angle is mathematically sound in practice it is not always viable. As pixels have a square aspect ratio accurate description of the rotation applied is difficult to implement and typically will lead leads to rounding errors in the associated calculations [65]. These rounding errors are exasperated when the targets to be detected many only cover a few pixels within the image. For this reason, rotated Haar-like features have been avoided in

most of the more recent literature. Furthermore, the introduction of larger and larger feature libraries, including rotated features if desired, leads to the calculations involved in the computation of Haar-like features becoming more and more complex. This increased complexity results in the need for more computational time and power, which is in opposition to the development of detection algorithms that are able to perform in real-time.

2.4 Super-Resolution Microscopy

As previously mentioned in Chapter 1, SR microscopy describes any microscopy technique that is able to surpass the resolution limit as describe by Ernst Abbe's equation [2].

$$d = \frac{\lambda}{2n \sin \alpha} \quad (2.7)$$

Where d is, the minimum distance needed between two objects that reveals them as separate entities, i.e. resolution, λ is the wavelength of light used for illuminating the sample and $n \sin \alpha$ describes the numerical aperture of the objective lens used in the microscope. These SR methods can be grouped into three main categories. Firstly, hardware based SR methods aim to manufacture a specific PSF smaller than Abbe's resolution limit, examples of this are STED microscopy [10] and SIM [11]. STED microscopy reduces the size of the PSF through the use of a second ring-shaped depletion laser which surrounds the illumination laser, whereas SIM employs optical patterning of the illumination and then combines the nonlinear response from the sample to reconstruct a SR image. Secondly, SMLM methods use both biological techniques and specially designed software to separate PSFs temporally allowing them to be localised with accuracy much greater than that of the diffraction limit. The most common examples of SMLM are PALM [9] and STORM [14]. Finally, computational SR methods use multiple diffraction limited images to restore a SR image using image processing techniques [66], it is into this category than the TRAM method, discussed in Chapter 6, resides.

2.5 Summary

Presented here is a review of the current methods used throughout this thesis. For particle detection, the processes of signal enhancement, segmentation and localisation are well documented with many methods suggested to complete each step of the detection process. What is clear from the literature is that the data under investigation needs to be appraised for quality (SNR and contrast) and features (size and shape) before a suitable method is selected and no one method can be successfully applied to all data. The key factors affecting the trajectory linking process are the amount of prior information about the particle movement that is available and the amount of power and time available for the computation of trajectories. Whilst the probabilistic methods in general outperform the deterministic methods they require much more processing time and the incorporation of prior information about the particles dynamics. Of the deterministic methods, the global nearest neighbour approach performs best with a possible area of improvement coming from the incorporation of motion models into this method.

Specifically, for the development of the signal enhancement and detection method using Haar-like features improved detection comes at computational cost. Increasing the feature library to include more detectable features requires prior knowledge of the features to be detected. However, the feature library can also be fine-tuned to only include Haar-like features describing the particles to be detected, this will further help the computational efficiency. Furthermore, rotation of features increases the complexity of the computation required, designing a feature that can avoid rotation would be preferential for efficient detection.

Finally, the use of SR methods is becoming increasingly more common. However, the complex hardware or experimental procedures required to achieve SR may be slowing its uptake by the wider scientific community. As such the use of computational methods for SR would be preferential as they do not require any specialised microscopy equipment.

However, in depth validation of such methods is essential to ensure that they are performing correctly.

Chapter 3 Single Particle Tracking in 2-Dimensional Microscopy Data

This Chapter discusses the challenge of tracking single particles in 2D microscopy data. As discussed in the previous Chapter, single particle tracking is typically split into the two independent challenges of particle detection and linking of detected particles to form trajectories. Treating these challenges independently is beneficial as it allows for the design of a tracking system, where the detection and linking methods are interchangeable, this in turn allows for the customisation of the tracking method depending on the features and quality of the data being investigated. Furthermore, the specific tasks contained within the particle detection challenge can be divided into the smaller sub-tasks of signal enhancement, segmentation and localisation. Splitting the tasks in this way allows for even greater customisation of the overall particle tracking method. Presented here are methods and techniques for particle detection and trajectory linking implemented into a particle tracking method. Of all the techniques described specific focus is given to the signal enhancement technique which uses Haar-like features and the trajectory linking method which utilises particle feature measurements extracted in the detection process.

3.1 Particle Detection

Typically, particle detection will follow the procedure of image denoising before signal enhancement followed by particle segmentation and finally localisation. However, the task of particle detection becomes increasingly more difficult as the SNR of the images within a time-lapse sequence data being investigated deteriorates. To achieve the best possible detection results in high noise environments sophisticated image denoising and signal enhancement are typically both required. However, in environments where the SNR is more manageable the process of image denoising can be simplified or omitted altogether as the challenge is to detect and localise particles and not to restore an image.

3.1.1 Image Denoising

Image denoising is the process of reducing the amount of noise and thus increasing the SNR of an image. Typically image denoising is described as a restoration process in which an image that has been corrupted by blur and noise is to be restored. In general, sophisticated image denoising methods will aim to solve the standard imaging inverse problem given by the equation $J = P \cdot I + N$. In this problem, the goal is to restore the original image I , from the observed image J , in which I has been corrupted by blurring effects due to the imaging systems PSF, P , and noise, N . However, image denoising in this way is typically time consuming and computationally expensive, especially if the process has to be completed for multiple images. Therefore, typically only simplified image denoising techniques based around Gaussian or median smoothing filters are used. These filters reduce the noise in images where necessary but do not maintain structures within the image. Using these filters places more emphasis on the signal enhancement process to restore any small (size) or weak signals affected in the smoothing process. Figure 3.1 gives an example of the difference between image denoising and signal enhancement techniques. In this simple 1D example the original Gaussian signal (blue line) has been corrupted by additive Gaussian noise (green line). A given image denoising technique would aim to restore the signal from its noise corrupted counterpart, in this case a simple smoothing filter was utilised to try and restore the original signal (yellow line). Signal enhancement techniques aim to increase the contrast at the edge of the signal, given as the FWHM in the simple example above, resulting in a signal similar to that given by the red line in Figure 3.1.

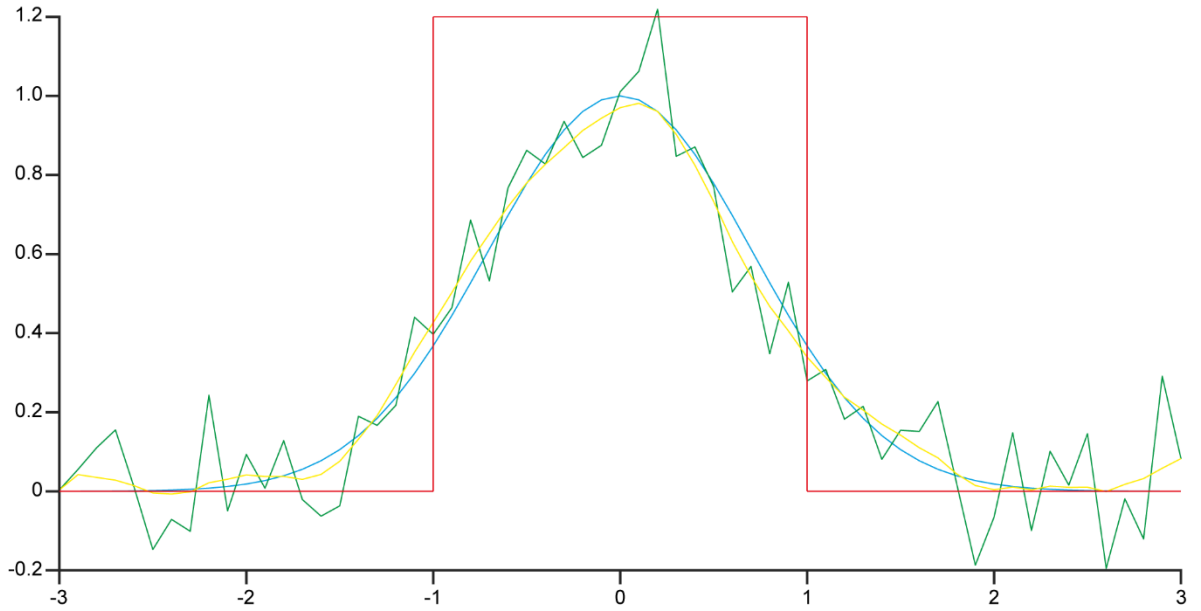


Figure 3.1: 1D comparison of signal denoising and signal enhancement. A single peak Gaussian distributed signal (blue line) is corrupted by additive Gaussian noise (green line). Signal denoising attempts to restore the original signal (yellow line) whilst signal enhancement (red line) attempts to increase the contrast.

3.1.2 Signal Enhancement

As seen in Figure 3.1 the goal of signal enhancement is to improve the contrast of particles, especially at the particles edge, and thus improving the ability to separate these particles of interest from their background within an image. Typically, signal enhancement is achieved through the use of filters that have been tailored specifically to the application. Signal enhancement can be coupled with image denoising processes, as enhancing the signal from the particles has the same effect as reducing the noise within the image. However, signal enhancement differs from image denoising in that it does not have the requirement of restoring or maintaining fine structure detail within an image. Proposed here is a signal enhancement method which builds on the concept of a PPI which is formed by first filtering an image with scalable Haar-like features before mapping to a PPI [67].

3.1.2.1 Particle Probability Image Signal Enhancement

Signal enhancement with a PPI is achieved through the non-local mapping of an input grayscale image into local-contrast image space, through the use of multi-scale Haar-like features, before mapping this local-contrast image into a PPI [67]. In this signal enhancement technique, the simple library of three Haar-like feature as previously described is adopted [29,67,68], with the PPI being generated following the more robust scheme outlined in [69].

Firstly, the library of three Haar-like features are used to measure the local-contrast values for each pixel in the input image (Figure 3.2a) for each feature at increasing spatial scales, $H_s^i \{i = 1,2,3\} \{s = 1, \dots 2 \times S\}$ where S is the size of the particles under investigation (Figure 3.2b). The local-contrast value for a pixel “i”, centred in a given Haar-like feature, is defined as the difference between the mean of the foreground pixel values (inner white pixels in 3.2b) and the mean of the background pixel values (outer gray pixels in 3.2b), of that given feature. Clearly, the measured value of local-contrast for “i” will be dependent on both the type of Haar-like feature used, and the spatial scale of that feature, H_s^i . As such, to complete the mapping of the grayscale image into local-contrast image space, the measurements from all three type of Haar-like features at all spatial scales need to be combined. This combination is achieved as a two-step process. Firstly, the maximum values from all spatial scales of a given feature are combined to generate three maximum local-contrast images (Figure 3.2c), one for each feature. These three maximum images are then combined by taking an average to complete the mapping into local-contrast image space (Figure 3.2d).

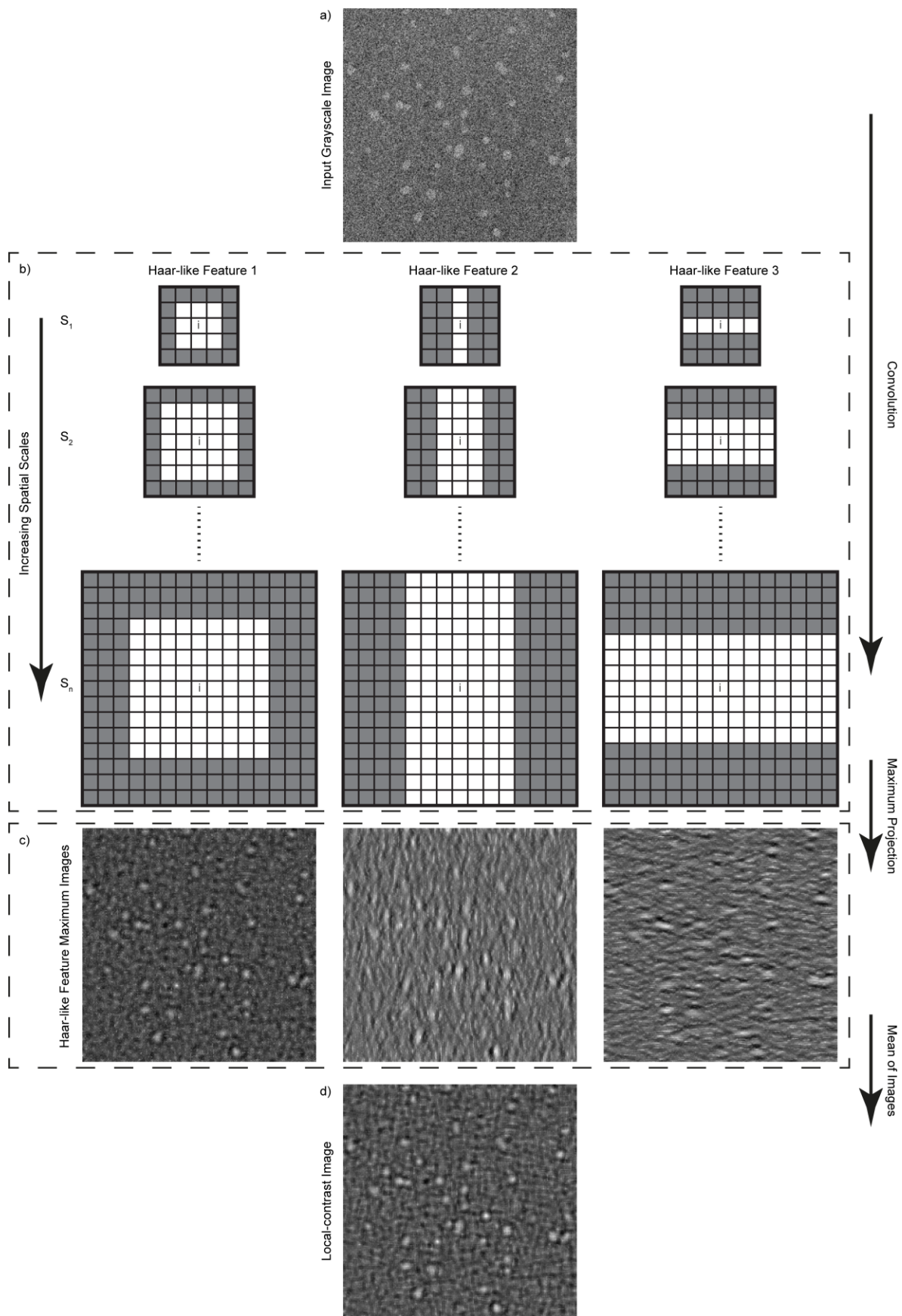


Figure 3.2: Process of mapping an image to a local-contrast image using Haar-like features. a) An example input grayscale image. b) Library of 3 Haar-like features used at increasing spatial scales measure the local-contrast within the input grayscale image. c) The maximum values for each pixel from each spatial scale are combined to form a maximum image for each feature. d) The 3 maximum images are combined by taking a mean to create a local-contrast image.

Next the local-contrast image is mapped into PPI space. This is achieved by first applying a global threshold to the local-contrast image (Figure 3.3b) to classify each pixel as either belonging to the foreground or background of the image. A higher value in the local-contrast image is indicative of a pixel that is statistically more likely to belong to the foreground than the background. The threshold for this classification is defined using a combination of the typical size of a particle, S , estimated number of particles in the image, P , and a particle enhancement factor, F . The particle enhancement factor is derived from both the density of the particles within the image and SNR of the image. Finally, the probability of particle existence in each pixel is calculated from the resultant binary image (Figure 3.3c), and is set as the ratio of the number of spatially connected foreground pixels to the total number of pixels in an area of size S , centred at that pixel. The use of only spatially connected foreground pixels, in the particle probability calculation, allows for the elimination of single isolated foreground pixels which will have most likely arisen from noise within the grayscale image. The resultant PPI (Figure 3.3d) can therefore be considered to be a signal enhanced and noised reduced counterpart of the input grayscale image (Figure 3.3a).

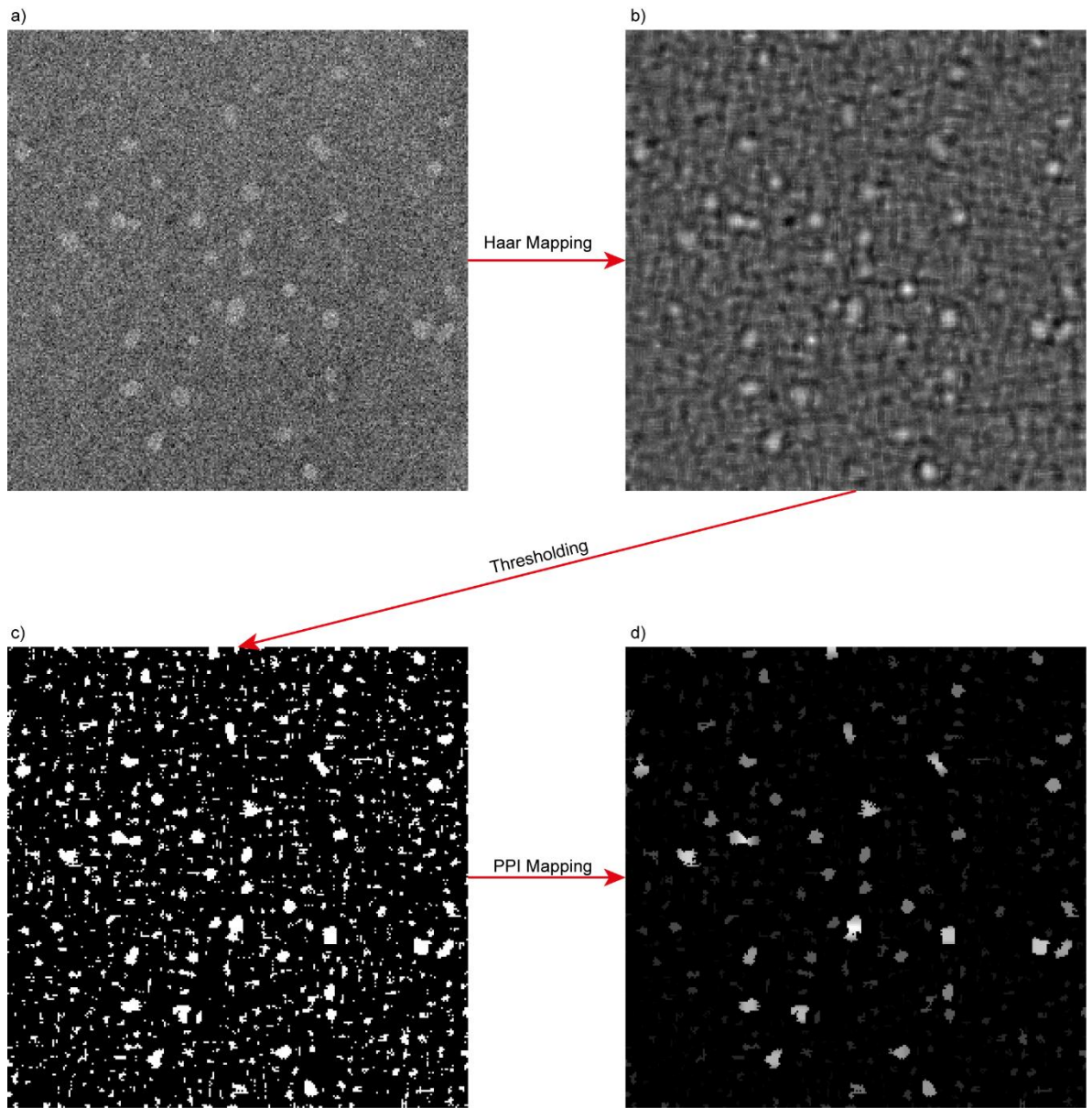


Figure 3.3: PPI Generation. a) The input grayscale image. b) The local-contrast image generated using Haar-like features as previously described. c) A threshold is applied to the local-contrast image to generate a binary image containing on (white, foreground) pixels and off (black, background) pixels. From this image the PPI is generated. d) Probability in each pixel of the PPI is calculated as the ratio of on pixels to off pixels from the binary image in a window the size of a typical particle surrounding the pixel in which probability is to be calculated.

3.1.3 Particle Segmentation

Particle segmentation is the process of identifying particle boundaries i.e. the outline of a particle. This process is of particular importance when localising particles using the centre-

of-mass localisation method, any error in the generated particle boundary will directly impact on the final localisation. The accuracy of segmentation also directly impacts on any measurements that are extracted relating to a particle, these measurements are later used in the trajectory linking process.

3.1.3.1 Marker-Controlled Watershed Segmentation

The watershed transform algorithm performs poorly, in low-SNR environments, when used independently, therefore so-called markers relating to estimated particles are implemented to help improve its performance. The incorporation of markers into the algorithm is typically referred to as marker-controlled watershed segmentation. Here the estimated particles markers are assumed to be local maxima identified in the grayscale image (Figure 3.4d), after convolution with a Gaussian kernel to reduce the number of false markers resulting from noise in the image. These markers are combined with the gradient of the grayscale image, calculated with a Sobel filter, (Figure 3.4e and f), as the gradient provides better identification of particle boundaries than the grayscale image itself, for processing by the watershed transform.

When the SNR of an image is extremely low, it is necessary to add a further restriction to the marker-controlled watershed transform. In the segmentation process these restrictions take the form of estimated particle boundaries, generated from the PPI (Figure 3.4b). These boundaries are initially generated using a simple global threshold of $1/e$ applied to the PPI, this value is derived from the assumption that each boundary will only contain a single peak distribution. Each of these estimated boundaries is then individually refined, considering the relative strength of the PPI values inside and outside of each boundary (Figure 3.4c). The significance of these estimated boundaries increases as the noise in the image increases, as the gradient can no longer be accurately measured causing the watershed transform to fail. Described in Figure 3.4h-k is an example of how the process can fail. Firstly, Figure 3.4h shows the result using the marker-controlled watershed segmentation in an image with relatively good SNR, here it is shown that the segmentation of particle

boundaries is accurate. A zoomed section from Figure 3.4h (highlighted by a yellow box) is shown in Figure 3.4j, here it can be seen that the gradient has strong values (high pixel intensity indicated by yellow arrows). These strong values are capable of maintaining the particle boundary without the other imposed restrictions. Conversely, Figure 3.4i shows the result using the marker-controlled watershed segmentation in an image where SNR is much lower, here segmentation is not as accurate. A zoomed section from Figure 3.4i (highlighted by a yellow box) is shown in Figure 3.4k, it is seen that the gradient has weaker values (low pixel intensity indicated by yellow arrows) and is no longer capable of maintaining the particle boundary. In this this case the particle boundary takes the form of the imposed estimated particle boundary restriction.

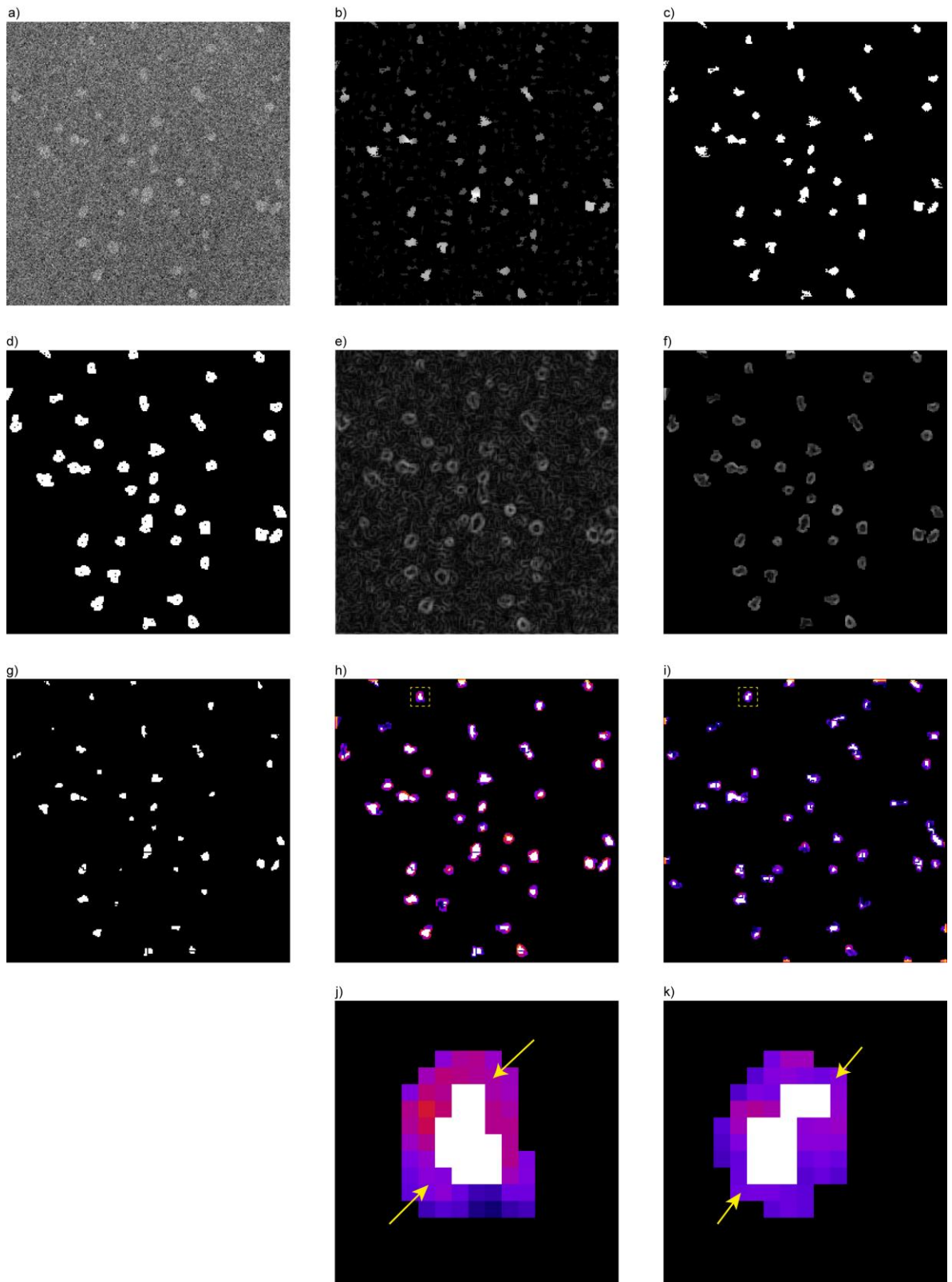


Figure 3.4: Mark-controlled watershed segmentation using grayscale image and PPI. a) Input grayscale image. b) The PPI corresponding to the input grayscale image. c) Estimated particle boundaries generated by thresholding the PPI. d) Estimate particle boundaries with the local maxima identified as markers for the watershed process. e) Gradient image of the input grayscale image calculated using a 3×3 Sobel filter. f) Gradient image with boundary restrictions and local

maxima from d) applied. g) Result of watershed segmentation for the input grayscale image. h) Example of segmented regions in which gradient is able to maintain the particle boundary as the input image has good SNR. i) Example of segmented regions in which gradient is not able to maintain the particle boundary as the input image has bad SNR, when this is the case the previously estimated particle boundaries become the final particle boundaries. j) A zoomed area of the box in h) with arrows indicating strong gradient values, as the input image has good SNR, and as such can maintain the particle boundary. k) A zoomed area of the box in i) with arrows indicating weak gradient values, as the image has poor SNR, and as such are not able to maintain the particle boundary relying on the estimated particle boundary to become the final particle boundary.

3.1.4 Particle Localisation

Particle localisation is the final step of any particle detection method and is where the co-ordinate location of each particle is defined with sub-pixel accuracy. Investigated here is the centre-of-mass localisation method. Centre-of-mass calculates the centre of the particle using the particle boundary generated in the segmentation process, as such the accuracy of this method is directly linked to accuracy of the segmentation. When using centre-of-mass localisation, weighting based on intensity from the grayscale image is used to improve its accuracy. However, centre-of-mass assumes that the particles location is at the centre of the particle (Figure 3.5c), which in the case of the single particles that are typically investigated using this method is true (Figure 3.5a). However, when the location of the particle is not at the centre i.e. in the case of particles that appear as asymmetric Gaussian distributions such as microtubules ends imaged with fluorescence microscopy (Figure 3.5b), the weighted centre-of-mass method is no longer accurate (Figure 3.5d).

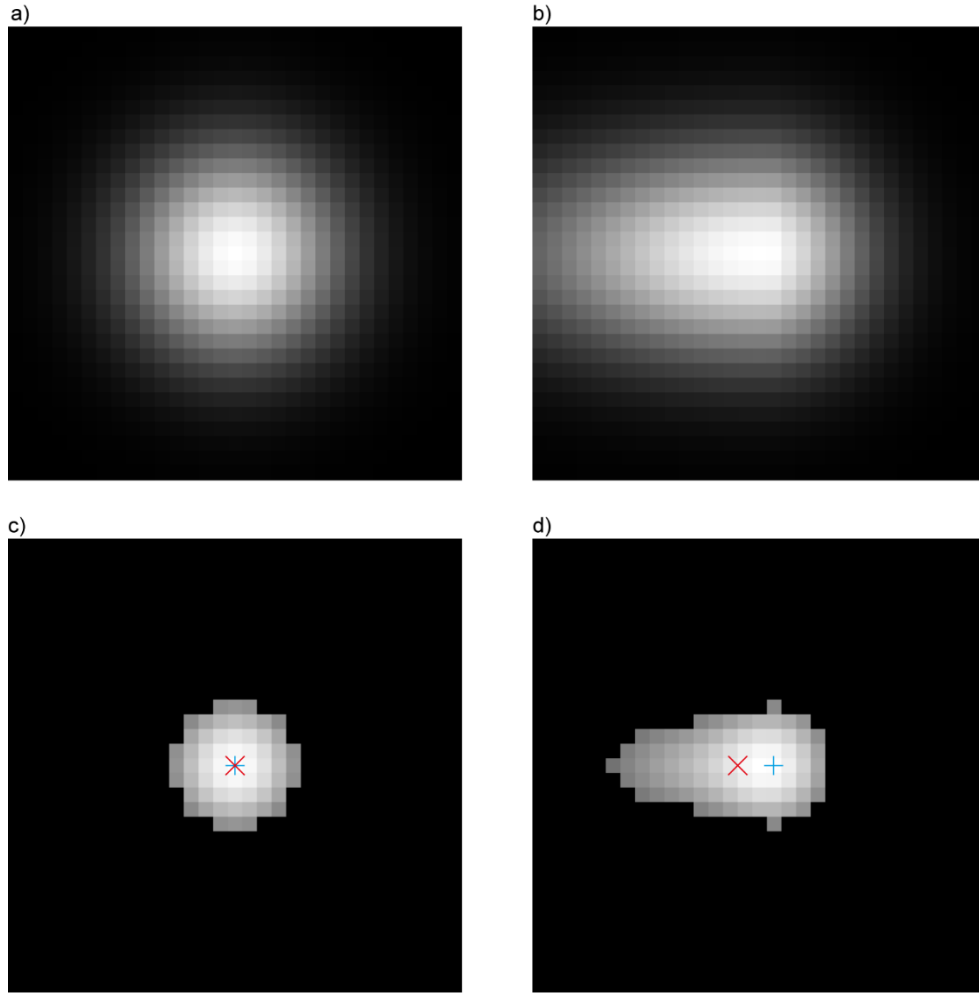


Figure 3.5: Comparison of localisation results on synthetic particles with symmetric and asymmetrical Gaussian profiles using centre-of-mass method. a) Synthetically generated symmetrical Gaussian distribution. b) Synthetically generated asymmetrical Gaussian distribution. c) and d) Results of localisation using the centre-of-mass method (red cross) in comparison with the ground truth (blue cross). See that the method is able to accurately identify the localisation for the synthetically generated symmetric Gaussian particle. However, in the case of the synthetically generated asymmetric Gaussian particle the centre-of-mass is approximately 2.5 pixels away from the ground truth localisation.

3.2 Trajectory Linking

The trajectory linking process of any tracking method aims to solve the correspondence problem of linking detected particles from frame to frame. Proposed here is a trajectory linking method which has been developed to link detected particles using additional particle features. Our method extends and improves previous work in which multiple Kalman filters are utilised in the IMM filter [29,69]. Improvements have come through extending the state

space variable to include more particle features describing a particles morphology and intensity profile, this allows for improved trajectory linking in image sequences with dense particle fields.

3.2.1 Trajectory linking with IMM and Kalman filters

Trajectory linking with the IMM method utilises three Kalman filters incorporated into the IMM filter. Each of the Kalman filters describes a different model of motion for the particles, with the IMM filter capable of switching between the three models to best estimate a particles future motion from its previous motion. The three motions that are modelled by the Kalman filters are random walk, first-order linear extrapolation and second-order linear extrapolation relating to Brownian motion, constant speed and constant acceleration respectively [55]. The IMM filter follows the three standardised particle linking steps; state prediction, data association and filtering parameters update, as described in [31,55]. Contributions to the improvement of trajectory linking using this method have focused on the state prediction step, here many more measures of particle features have been included in the state space variable describing each particles morphology and intensity profile. These measures can now be utilised with greater reliability in trajectory linking, as they can be more accurately measured due to improvements made in the particle detection and segmentation process. Furthermore, these morphological and intensity measurements become of more importance as the SNR of an image decreases, here the measurements of distance between particles in two consecutive state spaces become less dependable due to noise induced localisation error.

3.2.1.1 State Space Variable

The state space variable (or system state vector) of a trajectory linking method describes the current state of the system under investigation, at a given time point. Typically, it will

contain information regarding the location of particles (x_c and y_c) and other particle features e.g. area and intensity, for all particles within an image at a given time point. Correspondence between particles that appear in consecutive frames is determined by minimising the difference between all measured features for all particles. Here the state space variable has been extended to include measures of morphological features and measures describing the intensity profile of each particle. The morphological measures included are particle area, A , i.e. the number of pixels contained within the particle boundary (Figure 3.6, orange line), the area the bounding box (Figure 3.6, dashed yellow line) containing the particle boundary, A_B , along with the major axis distance (Figure 3.6, red arrow headed line), d_M , minor axis distance (Figure 3.6, blue arrow headed line), d_m , and perimeter (length of orange line in Figure 3.6), A_p , of the particle boundary. Extractable measurements relating to the intensity profile of each particle are more limited than the morphological measures available. As such, only the mean and maximum pixel intensity values, I_μ and I_{max} , within the particle boundary, are included in the state space variable. Furthermore, as intensity based measurements are easily corrupted by noise within the image, the particle intensity measurements are obtained from a noise reduced version of the grayscale image smoothed with a Gaussian kernel.

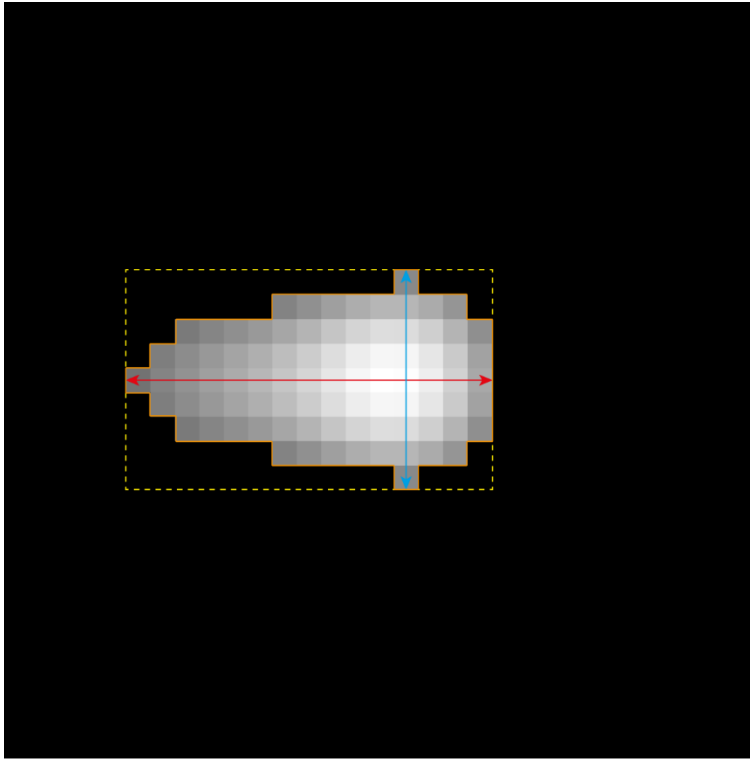


Figure 3.6: Schematic of measurements used in the state space variable for particle linking using the IMM method. The orange line represents the particle boundary, the length of which is the perimeter. The dashed yellow line represents the bounding box of the particle. Finally, the red and blue arrow headed lines represent the major and minor axis lengths of the particle, respectively.

Extending the state space variable in this way has allowed for more accurate trajectory linking, especially in images with dense particle fields and/or low-SNR. In dense particle fields the particle feature measurements become more important as the trajectory linking method can now more accurately distinguish differences in particles that are present in the same region of the image using these measures. In images with low-SNR the measurement of particle features again becomes more important as the localisation of particles become unreliable due to noise induced localisation error. However, the incorporation of many particle feature measurements into the state space variable of the trajectory linking process greatly increases its computational complexity. As such the number and type of particle feature measurements included in the state space variable using this trajectory linking method should be adapted for each individual application. Key factors for consideration when choosing what particle features to include are the image conditions i.e. the density of the particle fields and the SNR of the images, and hardware specifications such as the amount of memory and processing power available and time allowed for processing.

3.3 Performance Evaluation on Synthetic Images

In this section the performance of the particle tracking method and comparison with 14 other state-of-the-art tracking methods is completed on synthetically generated images.

3.3.1 Synthetic Datasets

Evaluation of the tracking method is undertaken on the synthetic data supplied for the particle tracking challenge of the “ISBI 2012” [70]. The challenge was set up so that different tracking methods could compete against each other on a variety of different datasets, each modelling various particle motions, particle densities and image SNRs. For the comparison with the 14 other state-of-the-art methods only the 2D image data scenarios named “vesicles” and “receptors” are included; the vesicle datasets model particles with Brownian motion and the receptor datasets modelled particles that switch between Brownian and directed motion. Both imaging scenarios consist 12 distinct datasets with each dataset having one of three particle densities; high, medium or low and one four different SNRs; 1, 2, 4 or 7. The SNR of the datasets was calculated using an intensity based method; $SNR = (I_0 - I_b)/\sqrt{I_0}$, where I_0 and I_b denote the peak object intensity and the mean background intensity respectively.

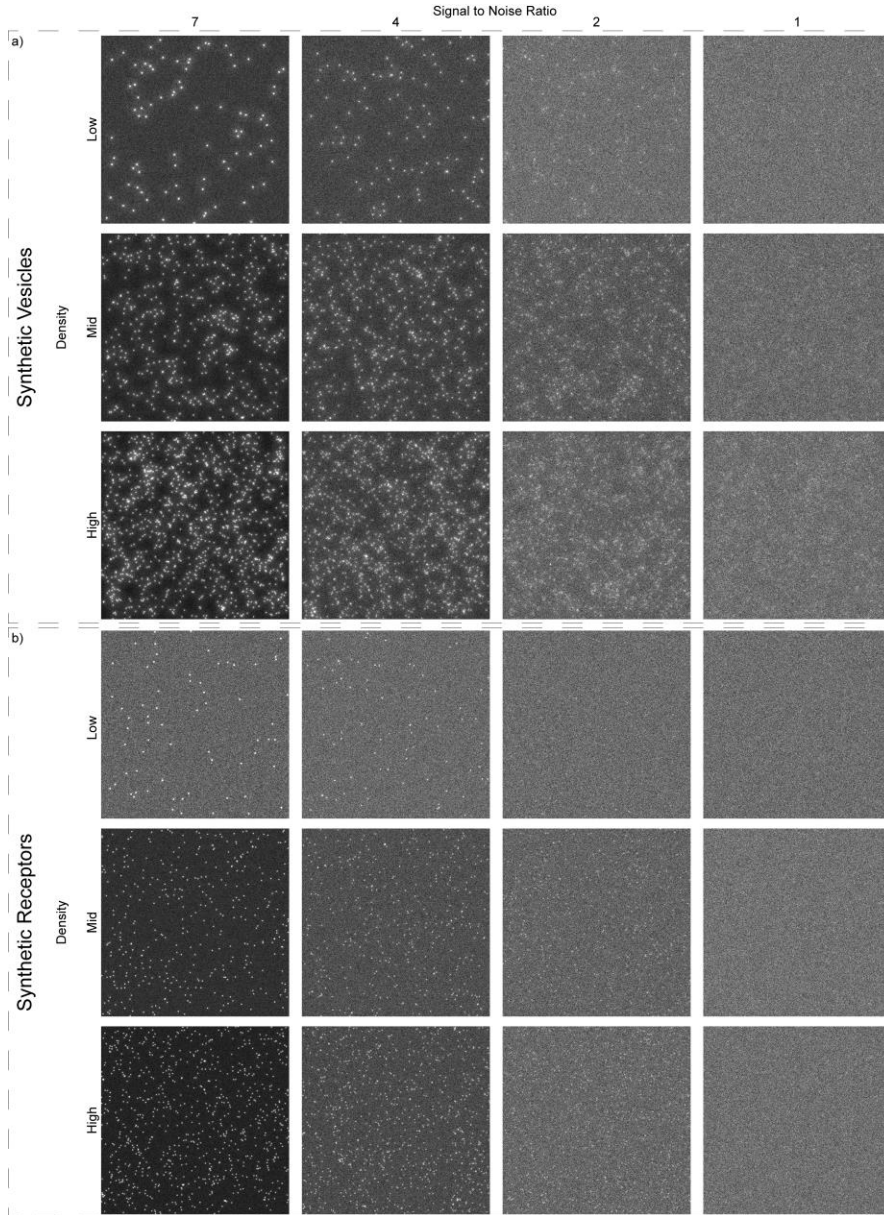


Figure 3.7 Sample image from each of the 24 datasets investigated. a) Sample images from the synthetic vesicles datasets. b) Sample images from the synthetic receptor datasets. In both panels a) and b) the SNR of the images decreases from 7 to 4, 2 and 1 in the columns going from left to right. The density of the particles within the images increases from low to mid to high in the rows going from top to bottom. Low particle density represents around 100 particles per image whereas mid and high densities represent around 500 and 1000 particles per image, respectively.

3.3.2 Comparison with State of the Art Methods

In total 14 different particle tracking methods competed in the particle tracking challenge organised by ISBI [70]. Each method used their own different approaches towards particle

detection and particle linking. Objective comparison of all methods was achieved through the use of six quantitative performance metrics; alpha, α , beta, β , the JSC for track points, JSC , the JSC for entire tracks, JSC_θ , the error of localisation, $RMSE$, and timing. However, for quantitative comparison with the particle tracking method described here the timing metric is excluded as similar hardware to allow accurate comparison is not available. Therefore, the metrics used in the comparison are calculated as follows:

$$\alpha(X, Y) \triangleq 1 - \frac{d(X, Y)}{d(X, \phi)} \quad (3.1)$$

$$\beta(X, Y) \triangleq \frac{d(X, \phi) - d(X, Y)}{d(X, \phi) + d(\bar{y}, \phi)} \quad (3.2)$$

$$JSC \triangleq \frac{TP}{TP + FN + FP} \quad (3.3)$$

$$JSC_\theta \triangleq \frac{TP_\theta}{TP_\theta + FN_\theta + FP_\theta} \quad (3.4)$$

Where for α and β calculations $d(X, Y)$ is the pairing distance between set of GT track X and estimated tracks Y . The distance between the two sets of tracks is determined using the Munkres algorithm, allowing a maximum pairing distance of 5 pixels between any two track points. Similarly, $d(X, \phi)$ is the pairing distance between the set of GT track and the set dummy tracks ϕ , finally, $d(\bar{y}, \phi)$ is the pairing distance between the tracks of Y that did not make it into the optimal pairing, \bar{y} , and the set of dummy tracks. For JSC and JSC_θ calculations, TP represents the correct, FN the missed and FP the spurious detections or tracks. The $RMSE$ metric is only calculated from the TPs in JSC , due to the pairing distance defined in the Munkres pairing algorithm $RMSE$ a maximal value of 5 pixels.

3.3.3 Results

Our particle tracking method was used to track the 12 datasets in each of the vesicle and receptors scenarios. For ease of understanding in the comparison, the results from the 14 other tracking methods, that took part in the ISBI particle tracking challenge, have been summarised into box plots. The centre of the boxes represents the mean value achieved by all 14 tracking methods on a given dataset, with the extrema of the boxes extending to one half a standard deviation from the mean, this gives the total box length as one standard deviation. The whiskers of the box plots extend to the minimum and maximum values achieved by the compiled 14 methods for any given dataset and metric. The performance of the tracking method presented here is represented by a blue line overlaying on the box plots. With a total of 24 datasets investigated and five performance metrics available for each dataset, this gives a total of 120 measures available for the comparison of the method with the other state-of-the-art methods. To easily describe all of the data from these 120 measures the results have been separated by performance metric. When referring to individual methods in the results, methods 1 to 14 are numbered the same as in the original particle challenge [70], with the method presented here added in as method 15.

The first comparison of the results of all the tracking methods is made using the alpha metric (Figure 3.8), which has an optimal value at one and a minimal value at zero. A high alpha is indicative of a tracking methods ability to accurately identify particle tracks with high accuracy, but does not account for the number false tracks that are generated whilst achieving this value. For both the vesicle (Figure 3.8, top row) and receptor (Figure 3.8, bottom row) data, at higher SNRs, the tracking method resides amongst the best performers used in the comparison. As the image quality deteriorates so does the performance of all tracking methods, with the performance of our, in comparison, also deteriorating and it is now only able to maintain an average performance, when compared to the other methods. However, particular note should be given to the performance of the method on the receptors dataset with medium density and SNR=2; here the method substantially outperformed all of the other methods in the comparison. Out of the 24 datasets investigated the tracking method achieved six number one rankings, equalled only

by method 11 [22,71,72]. However, unlike method 11 the number one rankings came from a variety of densities and SNRs in both scenarios, whereas method 11's all came from the receptor scenario, four of them from low density data.

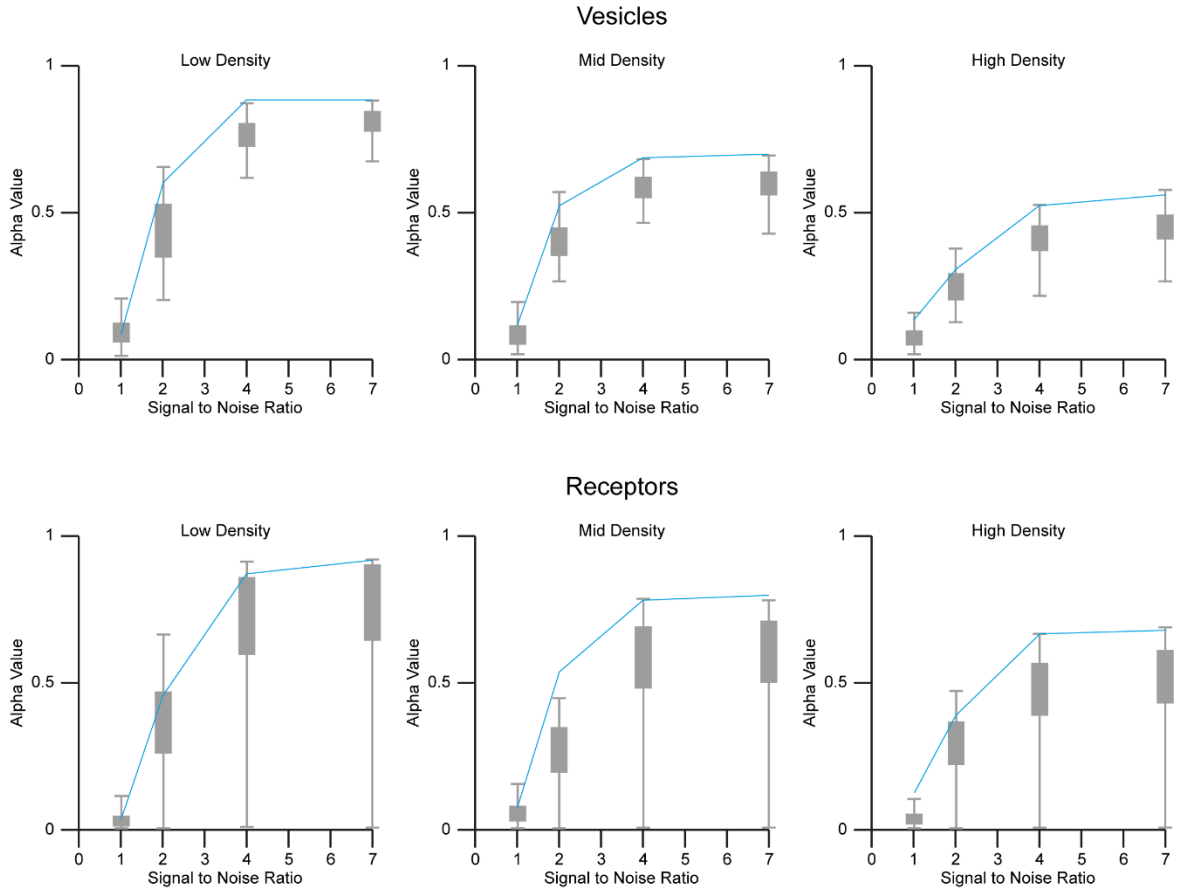


Figure 3.8: Performance of tracking method measured using the alpha metric. The top row shows the results on the synthetic vesicle data, whilst the bottom row represents the synthetic receptor data. In both rows the density of the particles move from low to high as you move left to right. In each graph the SNR increases as to move left to right along the x-axis. The method performs amongst the best of all compared methods for images with higher SNR, falling to an average performance for images with lower SNR. Of particular note is the performance of the method on the mid density receptor data with SNR=2, here the method outperformed all other methods compared by almost 10%. Another surprising yet pleasing result can be seen in the high density receptor data with SNR=1, here the method is again ranker number 1 on very low SNR data with which it typically struggles.

Examined next is the performance of the method using the beta metric (Figure 3.9). The beta metric is directly linked to the alpha metric; in that it also measures the tracking methods ability to accurately identify particle tracks. However, unlike the alpha metric the beta metric decreases in value with the number of false tracks that are generated, as such the optimal value for beta on a given dataset is the respective alpha value for that dataset and again has a minimal value at zero. For example, if a set of all possible tracks for an image sequence were generated, this set would contain all true particle tracks and as such would

achieve a perfect alpha score. However, this set of tracks would also contain an almost infinite number of false tracks, as such it would have a beta value approaching zero. Due to the beta metrics, close relationship with alpha metric the results of the tracking method using this metric follows very much the same pattern. Performance at higher SNRs for the vesicles (Figure 3.9 top row) and receptors (Figure 3.9 middle row) datasets is amongst the best of all the compared methods, with performance decreasing as the SNR deteriorates. Again, the method achieved six number one ranking using the beta metric, more than any other method, with method 11 achieving five number one rankings.

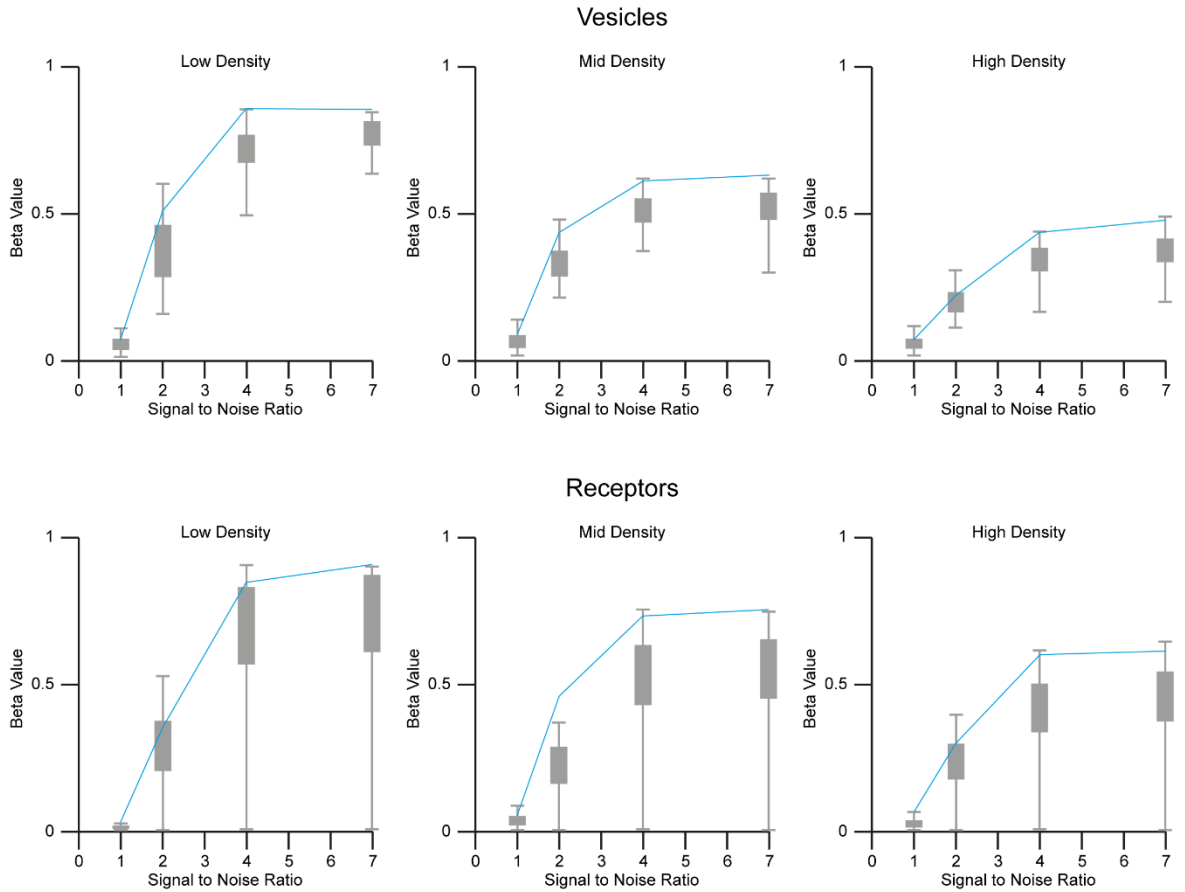


Figure 3.9: Performance of tracking methods measured using the beta metric. The top row shows the results on the synthetic vesicle data, whilst the bottom row represents the synthetic receptor data. In both rows the density of the particles move from low to high as you move left to right. In each graph the SNR increases as to move left to right along the x-axis. As the beta metric is so closely related to the alpha metric the results to are closely comparable. Again, the method is high achieving in data with high SNR, dropping to an average performance in data with a low SNR. However, again the method achieves excellent results in the synthetic receptor data with mid density and SNR=2 and high density data with SNR=1.

The JSC metric is a measure of the detection efficiency of a tracking method. JSC is calculated by classifying all points within a track as correct (if they are within the pairing distance

specified in the Munkres algorithm), suprious or missed. As seen in Figure 3.10 the tracking method again performed amongst the best of all the compared methods. For these datasets only two number one rankings were achieved. However, it is worth noting that most methods achieved very high values for this metric, as such the difference in value of the metric achieved between rankings is very small. This closeness in performance can be seen with three different methods achieving a best of five number one rankings, they are method 3 [22,59,73], method 5 [21,46] and method 7 [74]. As the JSC measure is purely a measure detection efficiency it would seem that the improvements made to the detection algorithm provide a clear advantage in the datasets examined.

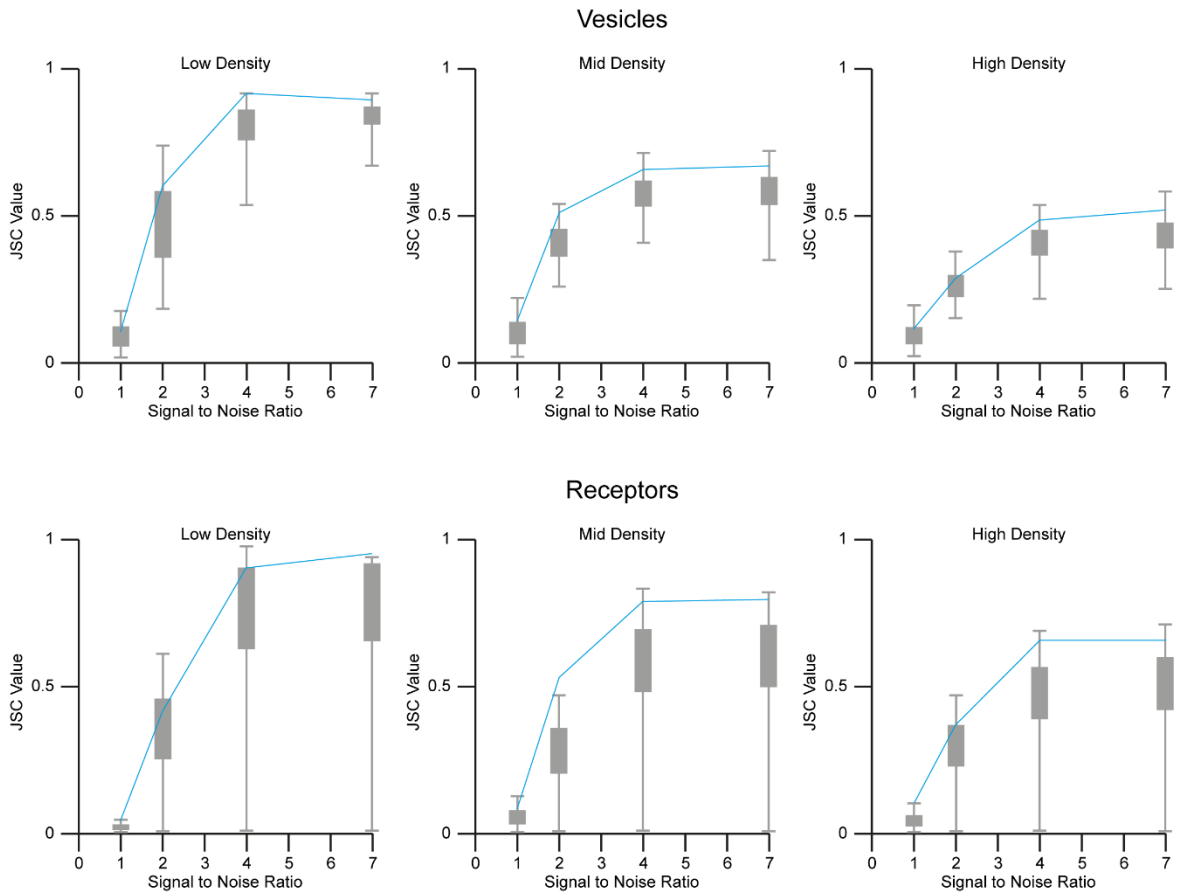


Figure 3.10: Performance of tracking methods measured using the JSC metric. The top row shows the results on the synthetic vesicle data, whilst the bottom row represents the synthetic receptor data. In both rows the density of the particles move from low to high as you move left to right. In each graph the SNR increases as to move left to right along the x-axis. Due to the simplified nature of this metric most teams see an improvement in performance making the relative performance of the method less substantial. However, as before the method achieves mean to high performance for all of the 24 datasets examined.

Similar to JSC the JSC_0 performance metrics classifies particle tracks as correct, spurious or missed and is purely a measure of the performance of the particle linking component of

each tracking method. Again, the tracking method performs amongst the best of all the compared methods (Figure 3.11) although it again only achieves two number one rankings. For this metric method 13 [34,75] achieved the most number one rankings with seven in total over the 24 datasets investigated.

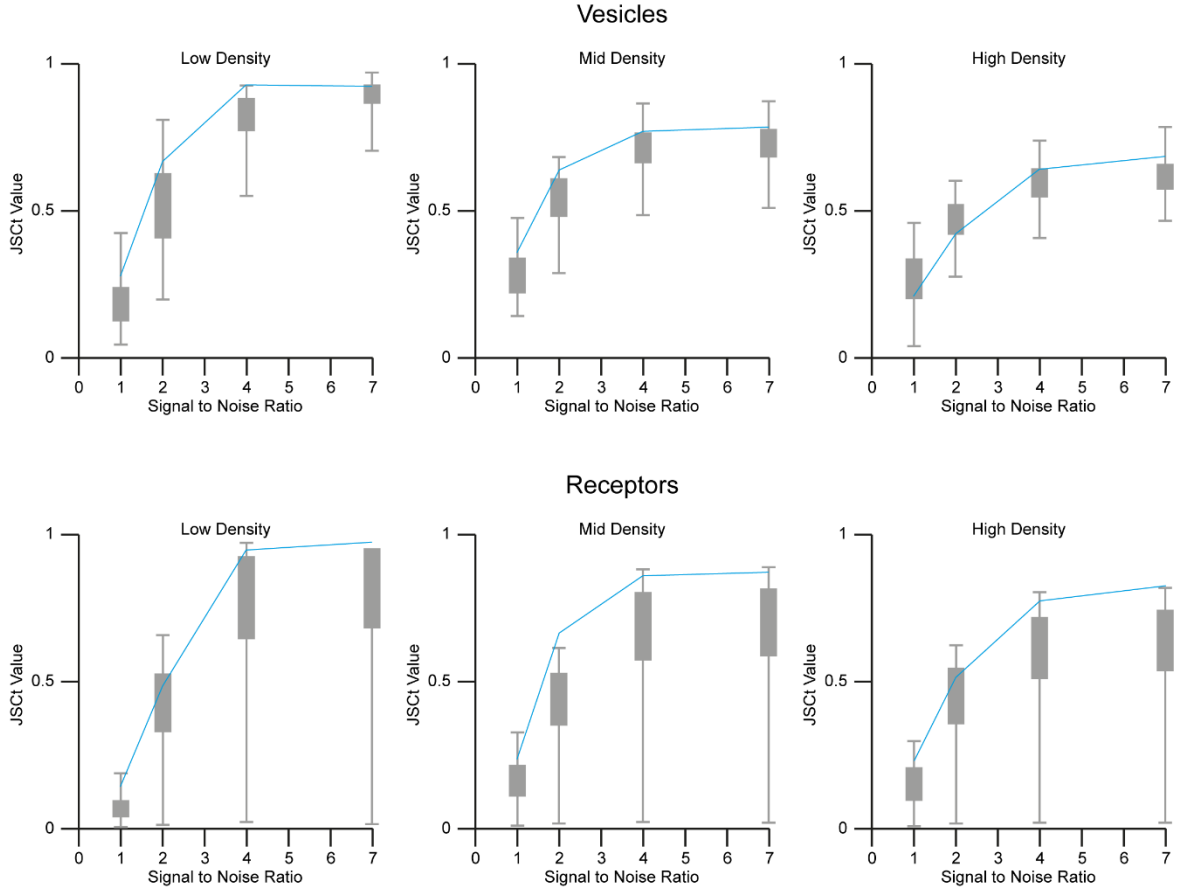


Figure 3.11: Performance of tracking methods measured using the JSC_t metric. The top row shows the results on the synthetic vesicle data, whilst the bottom row represents the synthetic receptor data. In both rows the density of the particles move from low to high as you move left to right. In each graph the SNR increases as to move left to right along the x-axis. As with the JSC metric the method achieves mean to high performance, when compare to the other competing methods, on all datasets except high density vesicles with SNR=1. Here the performance is just below the mean mark.

The final metric used in analysing the performance of all the tracking methods is RMSE, which is a measure of the localisation accuracy of the tracking methods. The RMSE is calculated from only the TP detections identified by the JSC metric, as such has an upper error bound of 5 pixels. As before the tracking method perform amongst the best of the methods evaluated (Figure 3.12). However, the method only achieved two number one rankings with method 1 [32] dominating with 16 number one rankings.

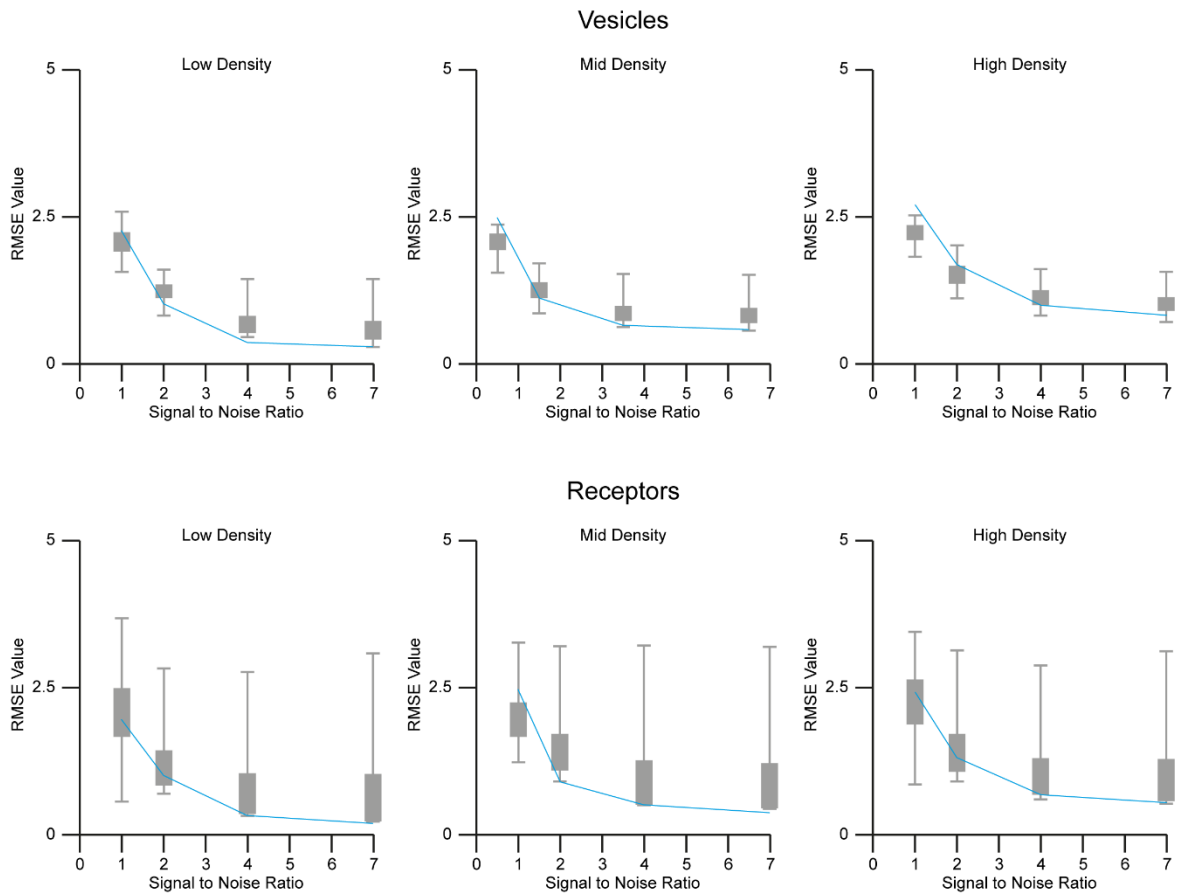


Figure 3.12: Performance of tracking methods measured using the RMSE metric. The top row shows the results on the synthetic vesicle data, whilst the bottom row represents the synthetic receptor data. In both rows the density of the particles move from low to high as you move left to right. In each graph the SNR increases as to move left to right along the x-axis. Unlike other metrics RMSE is best when at a minimum. Here the method again struggles with low SNR whilst achieving the best, or close to best results for the higher SNR datasets.

As seen from the above results it is clear that no one tracking method stands out above all others, with seven of the 15 methods investigated achieving the (joint) most number one rankings for the different metrics. Due to this variability in comparative performance it is useful to try and generalise the overall performance of all the investigated tracking methods. As such methods that achieved a top three result are examined, as opposed to just the number one ranked method, for each metric on each dataset, these results are present in table 3.1.

| Scenario | Density | SNR | Vesicles | | | | | | | | | | | | Receptors | | | | | | | | | | | |
|----------|---------|-----|----------|----|----|----|-----|----|----|----|------|----|----|----|-----------|----|----|----|-----|----|----|----|------|----|----|----|
| | | | Low | | | | Mid | | | | High | | | | Low | | | | Mid | | | | High | | | |
| | | | 1 | 2 | 4 | 7 | 1 | 2 | 4 | 7 | 1 | 2 | 4 | 7 | 1 | 2 | 4 | 7 | 1 | 2 | 4 | 7 | 1 | 2 | 4 | 7 |
| α | #1 | | 5 | 2 | 15 | 1 | 2 | 8 | 15 | 15 | 2 | 8 | 1 | 1 | 11 | 11 | 11 | 11 | 11 | 15 | 3 | 15 | 15 | 11 | 3 | 3 |
| | #2 | | 2 | 5 | 5 | 15 | 5 | 15 | 1 | 1 | 5 | 2 | 15 | 15 | 14 | 5 | 1 | 1 | 13 | 8 | 15 | 3 | 11 | 2 | 15 | 15 |
| | #3 | | 11 | 15 | 11 | 8 | 11 | 2 | 8 | 8 | 15 | 5 | 3 | 5 | 15 | 2 | 3 | 15 | 15 | 11 | 11 | 11 | 13 | 5 | 11 | 11 |
| β | #1 | | 5 | 2 | 5 | 15 | 5 | 8 | 8 | 15 | 5 | 8 | 1 | 1 | 15 | 11 | 11 | 15 | 11 | 15 | 3 | 15 | 11 | 11 | 3 | 3 |
| | #2 | | 2 | 5 | 15 | 1 | 2 | 15 | 15 | 8 | 13 | 5 | 15 | 15 | 13 | 2 | 1 | 11 | 13 | 2 | 15 | 3 | 15 | 2 | 15 | 15 |
| | #3 | | 13 | 9 | 3 | 5 | 13 | 3 | 1 | 1 | 11 | 11 | 3 | 8 | 11 | 9 | 3 | 1 | 1 | 11 | 11 | 11 | 13 | 5 | 11 | 11 |
| JSC | #1 | | 5 | 2 | 5 | 7 | 5 | 8 | 7 | 7 | 5 | 5 | 7 | 7 | 13 | 11 | 3 | 15 | 11 | 15 | 3 | 3 | 11 | 11 | 3 | 3 |
| | #2 | | 2 | 5 | 15 | 15 | 2 | 3 | 3 | 3 | 13 | 8 | 3 | 1 | 15 | 2 | 11 | 3 | 13 | 2 | 15 | 15 | 15 | 2 | 15 | 15 |
| | #3 | | 13 | 13 | 7 | 3 | 13 | 15 | 15 | 15 | 2 | 2 | 1 | 15 | 11 | 3 | 1 | 11 | 15 | 11 | 11 | 11 | 13 | 5 | 11 | 11 |
| JSC0 | #1 | | 13 | 13 | 7 | 7 | 13 | 8 | 7 | 7 | 13 | 5 | 7 | 7 | 13 | 2 | 3 | 15 | 13 | 15 | 3 | 3 | 13 | 11 | 3 | 3 |
| | #2 | | 2 | 2 | 15 | 12 | 5 | 3 | 3 | 3 | 5 | 8 | 3 | 5 | 15 | 13 | 1 | 3 | 1 | 2 | 11 | 15 | 1 | 5 | 15 | 15 |
| | #3 | | 15 | 5 | 5 | 3 | 15 | 5 | 8 | 8 | 14 | 11 | 5 | 15 | 5 | 9 | 11 | 5 | 15 | 5 | 15 | 11 | 11 | 2 | 11 | 11 |
| RMSE | #1 | | 12 | 1 | 15 | 1 | 1 | 1 | 1 | 1 | 12 | 1 | 1 | 1 | 12 | 1 | 1 | 1 | 12 | 15 | 1 | 15 | 12 | 1 | 1 | 1 |
| | #2 | | 1 | 15 | 8 | 15 | 12 | 8 | 15 | 15 | 1 | 8 | 8 | 15 | 1 | 12 | 11 | 6 | 1 | 1 | 11 | 11 | 8 | 11 | 11 | 15 |
| | #3 | | 15 | 12 | 10 | 5 | 14 | 15 | 10 | 12 | 14 | 12 | 12 | 12 | 15 | 8 | 6 | 11 | 11 | 12 | 12 | 12 | 1 | 8 | 15 | 11 |

Table 3.1: Top 3 tracking methods for each dataset. The method described here is include as number 15 (yellow) whilst the other 14 methods are numbered according to their original number in [70]. It is clear from the table than no one method dominated the rankings with a spread of methods achieving top 3 rankings for all datasets at all densities and SNRs.

To quantify the results from table 3.1 the frequency that all tracking method appears in table 3.1 was examined and a final ranking dependent on this frequency was determined, the rankings are given in table 3.2. As seen the method appears a total of 73 times out of a possible 120 in the top 3 spaces, 16 more than the next highest ranked method. Whilst these results do not give a full picture of the performance of each of the competing methods, they do indicate that the tracking method presented here is generally more effective at tracking this kind of synthetic image data. However, the variability in the best performing method on each dataset and each metric reiterates the need for careful consideration to be given to the system under investigation when developing these tools.

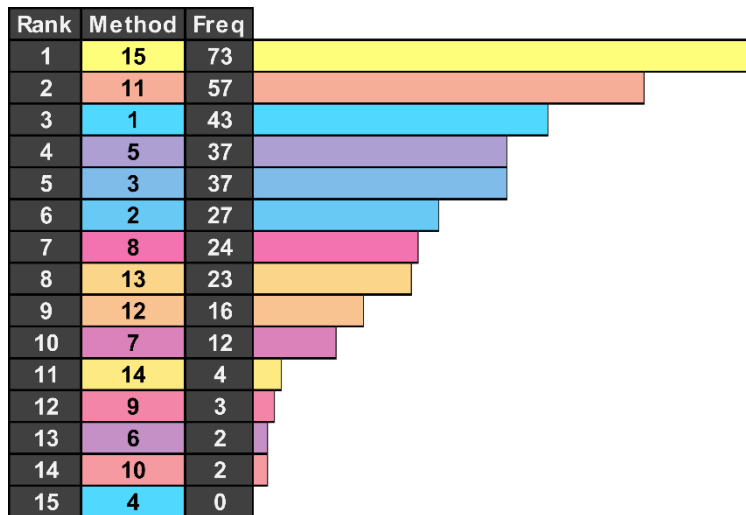


Table 3.2: Ranking based on the number of appearances in table 3.1. The method described here is the clear number one ranked method accumulating 73 top 3 appearances, 16 more than method 11 in second place. Note that method 4 scored no top 3 rankings as it did not compete on the datasets investigated here.

In conclusion, the proposed tracking method perform amongst the best of all the state-of-the-art methods evaluated here. Metrics describing the performance of the individual components of the proposed methods ability to detect (JSC), link (JSC_0) and localise (RMSE) particles shows that it is capable of performing amongst the best if the methods already available. As well as having highly comparable scores for the overall tracking performance metrics (alpha and beta).

3.4 Performance Evaluation on Real Microscopy Images

Even the well-modelled synthetic ISBI challenge datasets are unable to completely simulate experimentally collected data accurately. To further validate the tracking method, this time using real data, single EGFP-labelled LDCVs in PC12 cells were tracked, acquired using TIRFM at 20 FPS using an EMCCD detector.

3.4.1 Experimental Setup and Image Quality

Experimentally collected images have many more complex spatial and temporal image features and artefacts when compared to their synthetic counterparts. Larger fluctuations in intensities emanating from the particles, uneven image backgrounds and intensity-dependent noise all make the task of particle detection much more difficult. The SNR of the image sequence was estimated to be approximately 3.2, using the intensity based definition of SNR given in section 3.3.1. However, as image intensity fluctuates throughout a single image, as well as the entire image sequence, the SNR was measured manually by identifying many single vesicles throughout the image sequence, and defining the background as being a region directly adjacent to that vesicle. A value of SNR=3.2 was obtained averaging of around 200 such observations. The density of the particles within the image was found to be equivalent to the medium density level of the ISBI challenge datasets [70].

3.4.2 Comparison of Performance

To form a GT for comparison vesicles were manually identified in all image frames and linked manually from frame to frame to form tracks. As the GT, has been generated manually, the distance measurements between the GT and measured tracks becomes unreliable, here synthetic images are preferential for defining a GT. As the metrics α , β , and RMSE are dependent on the distance measurement the results would not be accurate, as such for analysis of the tracking method on this data only the JSC and JSC₀ metrics are utilised. Other tracking methods included in the comparison on this data are method 1, method 6 [43] and method 12 [31,76], also included is the commercial software Imaris (Bitplane). Methods 1, 6 and 12 were chosen for the comparison as the software for these methods was readily available from their respective websites. They also represent a good distribution in performance of the methods investigated above in that method 1 is a highly ranked method (rank 3), method 12 is a middle ranked method (rank 9) and method 6 is a lower ranked method (rank 13).

3.4.3 Results

Figure 3.13a shows the first frame from a time-lapse microscopy sequence of 250 frames, the tracks identified by the tracking method for the whole time-lapse sequence are overlaid (in arbitrary colours for contrast). The results for the JSC and JSC_{θ} metrics from the trajectories identified by all methods are given in Figure 3.13b. It can be seen that, as expected, the method performs better with the JSC and JSC_{θ} metrics when compared to the other methods. This is indicative of a higher specificity and sensitivity by the method in its ability to not only detect individual vesicles in each frame but also link these detections correctly throughout the image sequence.

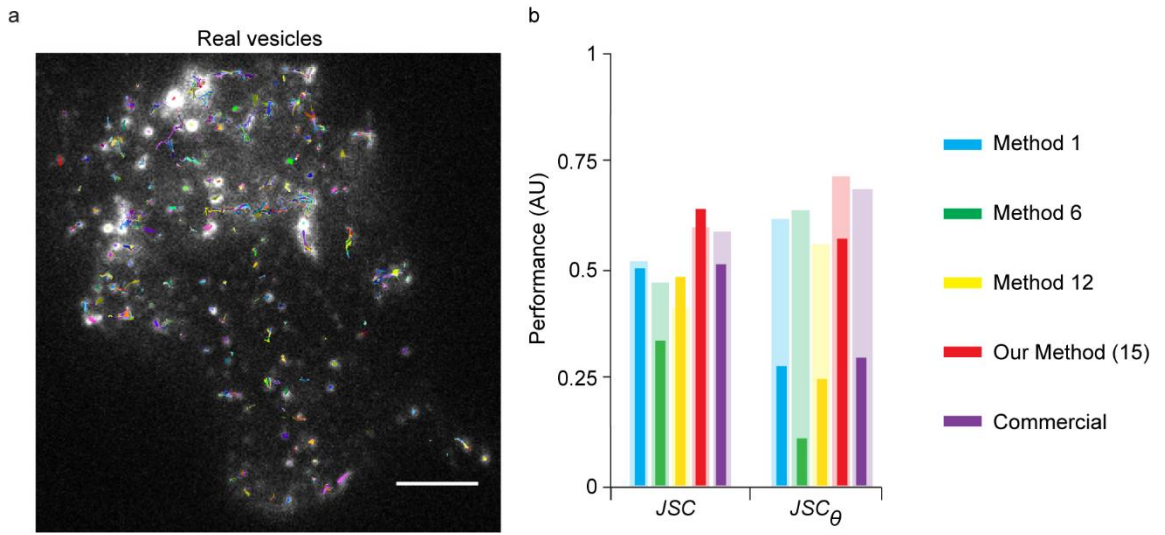


Figure 3.13: Performance Comparison on Experimental Data. a) The first of 250 image frames of single large dense-cored vesicles of PC12 cells, acquired under TIRF illumination at 20 fps, with 267 X 275 pixels and scale bar: 5 μ m. All the tracks laid on the image have a minimum tracked length of three frames. b) Performance comparison of the JSC and JSC_{θ} metrics, blue for Method 1, green for method 6, yellow for method 12, red for the method described here (15) and purple for Imaris; the faded bars correspond to their performance on the synthetic vesicles at similar level of noise and particle density.

Also of interest is comparing the results on these experimentally collected images with the synthetically generated images, this allows for the investigation of consistency between tracking methods results on synthetic image data and this more complex image data. The faded bars in Figure 3.13b represent values of the JSC and JSC_{θ} metrics for synthetic vesicle data of the same density and SNR of the experimentally collected images. As seen all methods give a consistent performance on this image data despite its more complex behaviours for the JSC metric. However, for the JSC_{θ} metric whilst the method is the most consistent it has lost some of its consistency. The other investigated methods perform even more less consistent in comparison.

3.5 Summary

Presented in this Chapter is a tracking method for the tracking of single particles in 2D image space. Particle detection is achieved through signal enhancement using Haar-like features and a new thresholding scheme. Clumping splitting of conjoined particles is completed using a marker-water controlled watershed transform with markers being defined as local-maxima in the original grayscale image. For images with lower-SNR a further restriction is applied to the watershed transform in the form of boundaries derived from the PPI. Finally, localisation of the particles is defined as the intensity-weighted centred of mass because of its efficient nature and applicability to most application to which the method is applied i.e. particles with symmetric intensity profiles. Trajectory linking uses three Kalman filters within an IMM framework with an extended state space variable including information about a particles morphology and intensity profile.

The method is fully validated using synthetic data and compared with 14 other state-of-the-art methods presented in [70]. The proposed method performs amongst the best of all the compared methods on the datasets tested for all 5 performance metrics. Furthermore, the technique is validated on real microscopy images again showing to be among the best of the methods tested which included the commercial software Imaris. Our method also showed a consistent result on tracking in real microscopy images when compared to the expected result from synthetic image data of the same SNR and density despite the more complex image features present in real microscopy image data.

Chapter 4 Biological Applications

4.1 Tracking of Single Molecules

An important goal in current biology is to be able to track large quantities of single molecules for the analysis of the global dynamics of these molecules. This challenge presents significant difficulties as individual fluorophores attached to the molecules of interest can only emit a low number of photons before they are destroyed by effects such as photo-bleaching. Furthermore, image acquisition at high frame rates is required to avoid under-sampling and thus the loss of fast particle dynamics, hence noise typically tends to dominate fluorescent time-lapse microscopy datasets used in these applications. To tackle such a challenge, the 2D particle tracking method, described in Chapter 3, was applied to two distinct live-cell fluorescent time-lapse microscopy datasets imaged using a spt-PALM protocol. For these datasets, the dynamics of munc18-1, a protein essential for regulated exocytosis in neurons and neuroendocrine cells, and SNAP-25, the most abundant pre-synaptic protein essential for regulated hormone secretion, were examined. As such both molecules were labelled with PAmCherry firstly in primary cortical neurons and secondly in neuroendocrine cells, with each of these datasets presenting their own limitations and challenges.

4.2 Experimental Setup

All fluorescence time-lapse microscopy data was acquired using the Olympus Cell Excellence software on an Olympus IX-81 microscope in TIRF mode equipped with an Olympus 150X UAPO 1.45 NA oil objective lens resulting in a pixel size of 106 nm. Cells were maintained in 5 % carbon dioxide and at a temperature of 37 °C throughout all experiments. For the spt-PALM imaging experiments the PAmCherry fluorophores were cyclically activated by a laser of 405 nm and imaged using a laser of 561 nm under TIRFM illumination conditions. For

each cycle, it was ensured that all activated molecules were bleached and no longer emitting before the next cycle of activation. Detection of fluorophores emitted from the primary cortical neurons was taken using an EMCCD, (Hamamatsu) detector. Images were collected at a rate of 30 FPS for 20 spt-PALM cycles with each cycle containing 100 images, this results in a dataset of 2,000 images of size 171×256 pixels. For experiments using neuroendocrine cells a sCMOS (Hamamatsu) detector was implemented. Here images were collected at a rate of 100 FPS for 60 spt-PALM cycles with each cycle containing 3,000 images, this resulted a dataset of 180,000 images of size 258×198 pixels.

4.3 Results

4.3.1 Tracking of Single Molecules in Primary Cortical Neurons

A time-lapse image sequence of 2,000 frames was acquired, using the experimental setup described, from live primary cortical neuron cultures. The SNR of this image sequence was estimated to be approximately 2, using the equation from section 3.3.1. Due to the nature of the spt-PALM imaging protocol utilised the density of the particles within the images could be assumed to be between low and medium, and hence favourable for trajectory linking by the method. Initially particles were detected in all frames using the particle detection method, from these detections just over 4,000 particle trajectories were subsequently formed using the trajectory linking method (both methods described in Chapter 3). Figure 4.1a shows all of the identified trajectories (in arbitrary colour for contrast) laid over the first image of the time-lapse image sequence. Figure 4.1b shows the density map of particles trajectories (given in log scale for contrast) corresponding to the number of trajectories which pass through each pixel of the images throughout the time-lapse image sequence. Investigating the dynamics of individual munc18-1 molecules further, as well as their collective behaviour, the angular direction of motion (θ_1) of each link within all of the trajectories is studied. This angle θ_1 is described in Figure 4.1c and displayed as a “rose diagram” Figure 4.1d. Rose diagrams are best described as angular

histograms, where the size, angle and colour of each “petal” section describes the movement of particles between 2 consecutive frames. For each petal, the size of each petal sub-section describes the volume of movements at that angle (angle of petal) and speed (colour of petal sub-section). The munc18-1 molecules travel along the axons within the neurons, this manifests strongly in the rose diagram as an off centre vertical line that is aligned with the orientation of the axon in Figure 4.1d. Molecules accumulate in varicosities of the neurons, in these areas the movement of the molecules behaves as Brownian motion this is shown by the inner circular structure in Figure 4.1d. The inner circular structure also has slight horizontal extensions due to the movement of molecules along a secondary branch of the neurons axon, this branch can be seen in the top left of Figure 4.1a.

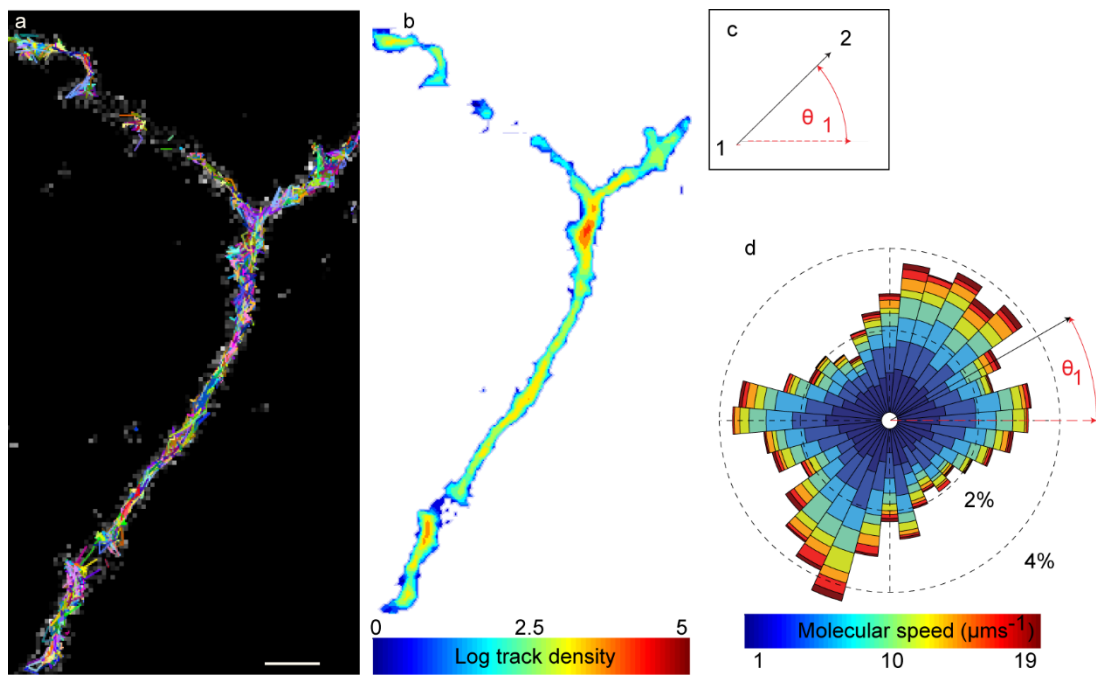


Figure 4.1: Tracking of single munc18-1 molecules a) A typical image (171 X 256 pixels) containing large quantities of single munc18-1 molecules overlaid with the trajectories (arbitrary colours for contrast) from the image sequence, scale bar: 1 μm . b) Trajectory density map (white background) showing the quantity of tracks passing through each pixel of the image. c) The measurement method of the angle θ_1 describing the direction of motion. d) Rose diagram displaying the overall dynamics of the direction of motion with the strongest directions of motion aligning with the orientation of the axon.

4.3.2 Tracking of Single Molecules in Neuroendocrine Cells

High-speed data acquisition is essential to avoid sampling artefacts when investigating the dynamics of biological sample, especially fast processes such as molecular diffusion. Whilst EMCCD detectors provide increased sensitivity for imaging these samples they are limited by their acquisition rate. To overcome this high-speed imaging using a sCMOS detector was used to image labelled SNAP-25 single molecules in neuroendocrine cells. As neuroendocrine cells have a larger surface area than the previously investigated neurons the task of particle tracking in these cells is not as simple. A spt-PALM time-lapse image sequences was acquired under TIRF illumination at 100 FPS with each PALM cycle lasting 30 seconds and a total of 60 cycles acquired, this results in a dataset consisting of 180,000 image frames. However, when imaging with an sCMOS detector although higher frame rates are achievable, they are typically of lower sensitivity, when compared to EMCCD detectors, because of this the SNR of the dataset was measured to be on average as 1.45. However, even at this high noise level the method can accurately identify and localise single molecules throughout the time-lapse image sequence. Detection and localisation was manually confirmed by random checks throughout the dataset. Again, because of the nature of spt-PALM, particle density is low-mid and hence favourable for trajectory linking, the resulting trajectories were checked for accuracy before analysis. In total, more than 200,000 trajectories were identified, these can be seen overlaid on a sample image from the dataset in Figure 4.2a. As these cells have a larger surface area it is possible to accurately measure two angles for each link within a trajectory. Firstly, the direction of motion, θ_1 , as before and secondly the direction of motion switching, θ_2 , as shown in Figure 4.2b. The molecules were found to display Brownian motion in their direction of motion displaying as an evenly distributed rose diagram in Figure 4.3c. However, by measuring the direction of motion switching θ_2 , it can be seen that if a molecule initially travels along a given direction, it has a high probability of switching its direction of motion to the opposite direction in the following step, this manifests as a strong asymmetry in the rose diagram for the direction of motion switching favouring $\theta_2 \approx 180^\circ$ (Figure 4.2d).

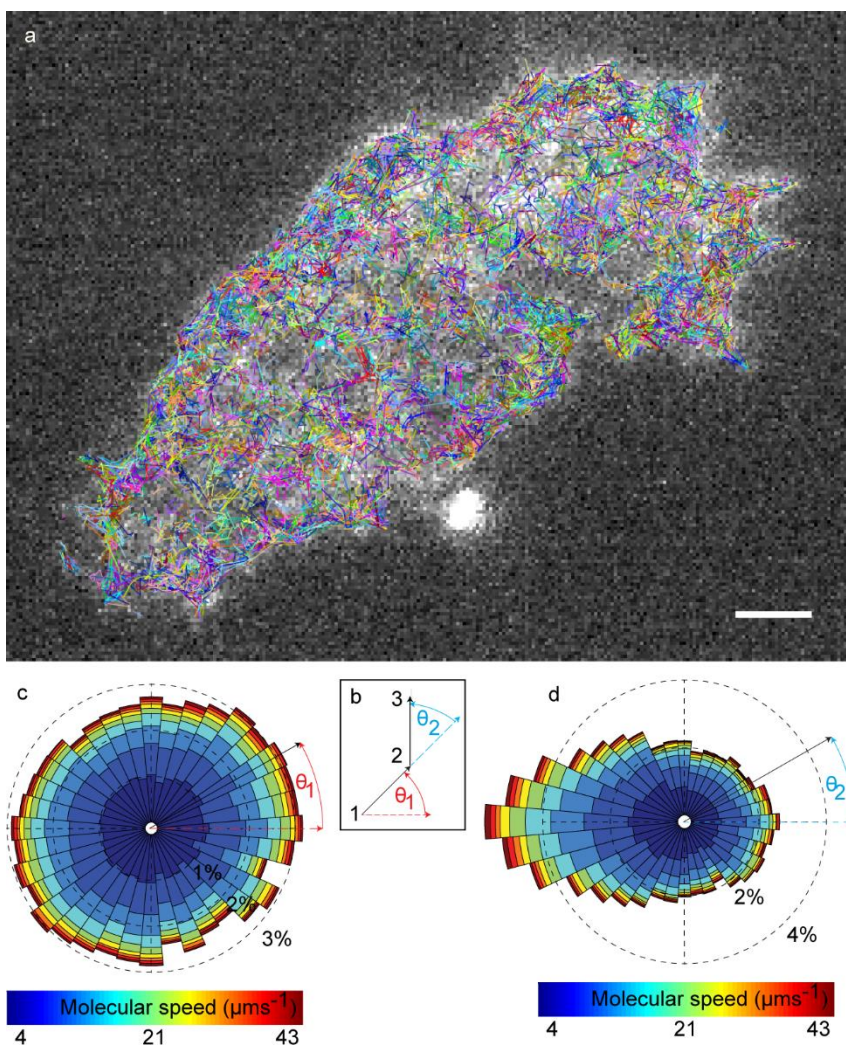


Figure 4.2: Tracking of single SNAP-25 molecules. a) An exemplar image (258 X 198 pixels) of SNAP-25 molecules in a neuroendocrine cell used for particle tracking, scale bar: 1 μm . Overlaid are 202,890 trajectories (arbitrary colour for contrast) obtained from the time-lapse image sequence containing 180,000 frames. b) Schematic showing how the angles that measure the direction of motion, θ_1 , and direction of motion switching, θ_2 , are calculated. c) Rose diagram showing the collective dynamics of direction of motion. d) Rose diagram showing the collective switching in direction of motion of molecules.

4.4 Summary

Even in the absence of sophisticated image denoising techniques, the particle tracking method described in Chapter 3 is able to generate particle trajectories even in the most complex imaging and biological environments where images are subject to artefacts such as inhomogeneity of pixel intensity and intensity-dependant noise. Furthermore, the method is able to process hundreds of thousands of images and particle trajectories in a

very efficient manner without the need for high-end specialist computer hardware i.e. using only a readily available desktop computer. Finally, the high probability of switching motion by 180° by the particles seen in Figure 4.2d would appear to agree with the earlier hypotheses about the organisation of palmitoylated proteins at the cell membrane in that they appear to move as if caged in nanodomains [77].

Chapter 5 Particle Tracking 3-Dimensional Microscopy Data

As with most biological structures cells are 3D in nature and not just 2D surfaces. As such the processes to be investigated within these cells also occur in 3D, therefore being able to track particles in 3D space is essential to fully understand the dynamics of various biological processes. However, “true” 3D time-lapse microscopy methods, where multiple focal planes of a sample are imaged at once, are not currently widely available and difficult to implement requiring specialised instrumentation [78–80]. Most current techniques achieve 3D time-lapse microscopy by continuously moving from focal plane to focal plane to take images. However, these methods are prone to motion induced distortions as the particles being imaged are constantly moving, with the extent of this distortion being directly linked to the amount of time it takes to move the microscope stage from focal plane to focal plane. However, as the technologies to achieve “true” 3D time-lapse imaging become more widely available to the scientific community, it will be essential that the tools to analyse the data generated by these technologies are ready.

Presented in this chapter is a new tracking method which is capable of working with both 2D and 3D image data. Particle detection in this new method is achieved using a novel Haar-inspired feature which improves signal enhancement allowing for accurate segmentation through the use of a global threshold. Finally, localisation for 2D image data takes the form of Gaussian fitting, whereas for 3D image data weighted centre-of-mass is utilised. Trajectory linking in both 2D and 3D image space is performed by extending and improving the global nearest neighbour method from [32] in three main areas. Firstly, the method is now capable of handling 3D image data, a necessity for a 3D tracking method. Secondly, many different particle features have been incorporated into the state space variable allowing for better trajectory linking in dense particle fields. Finally, motion models are incorporated which describe both Brownian and directed motion, with the trajectory linking method being able to switch between the models based on the particles instantaneous previous motion. The particle tracking method is fully validated on all 2D and 3D synthetic

image datasets presented in [70] allowing for the comparison of the with up to 14 other state-of-the-art methods.

5.1 Particle Detection

As discussed previously in Chapters 1, 2 and 3 particle detection is typically a three stage process of signal enhancement, segmentation and localisation. Each of these steps for the detection method is discussed in the following sections, highlighting the differences in how these processes perform for 2D and 3D image data.

5.1.1 Signal Enhancement using a Novel Haar-Inspired Feature

As mentioned in section 2.3, Haar-like features were derived from the Haar wavelet and first successfully implemented for object detection in [62]. Improvements in object detection methods using the Haar-like features primarily resulted from increasing the complexity and number of features used, this subsequently increases the complexity of the calculations involved [63–65]. The motivation behind the development of the Haar-inspired feature has come from two sources. Firstly, to provide local-contrast signal enhancement through filtering of an image with a Haar-like feature without the need for feature rotation, whilst also keeping the number of features used as small as possible, in doing so this minimises the complexity of the computation required. Secondly, as the main application of the Haar-inspired feature is the detection of single particles, the size of which are an order of magnitude below the diffraction limit. As such the Haar-inspired feature should follow the shape of a sub-diffraction particle i.e. that of an airy disk as described by Abbe [2] (Figure 5.1a) and therefore is circular in shape in 2D space (Figure 5.1b). As optimal signal enhancement using Haar-like features, and the Haar-inspired feature, will be achieved when the internal section (Figure 5.1b, white) of the feature used is of the same size, shape and orientation of the particle to be detected and the surrounding area contains zeros

(Figure 5.1b, black) [63], using a circular Haar-inspired feature should provide optimal signal enhancement for an Airy disk shape. In the case of detecting particles in 3D space the same theory is extended to 3D space and “*what’s a circle in three dimensions? A sphere.*” [81]. As such, the Haar-inspired feature in 3D space takes the form of a sphere, as shown in orthogonal views in Figure 5.1c. Whether being circular in 2D image space or spherical in 3D image space the Haar-inspired feature has the property of having an infinite order of rotational symmetry, this thus fulfils the first motivation of eliminating the need for feature rotation and more complex computations.

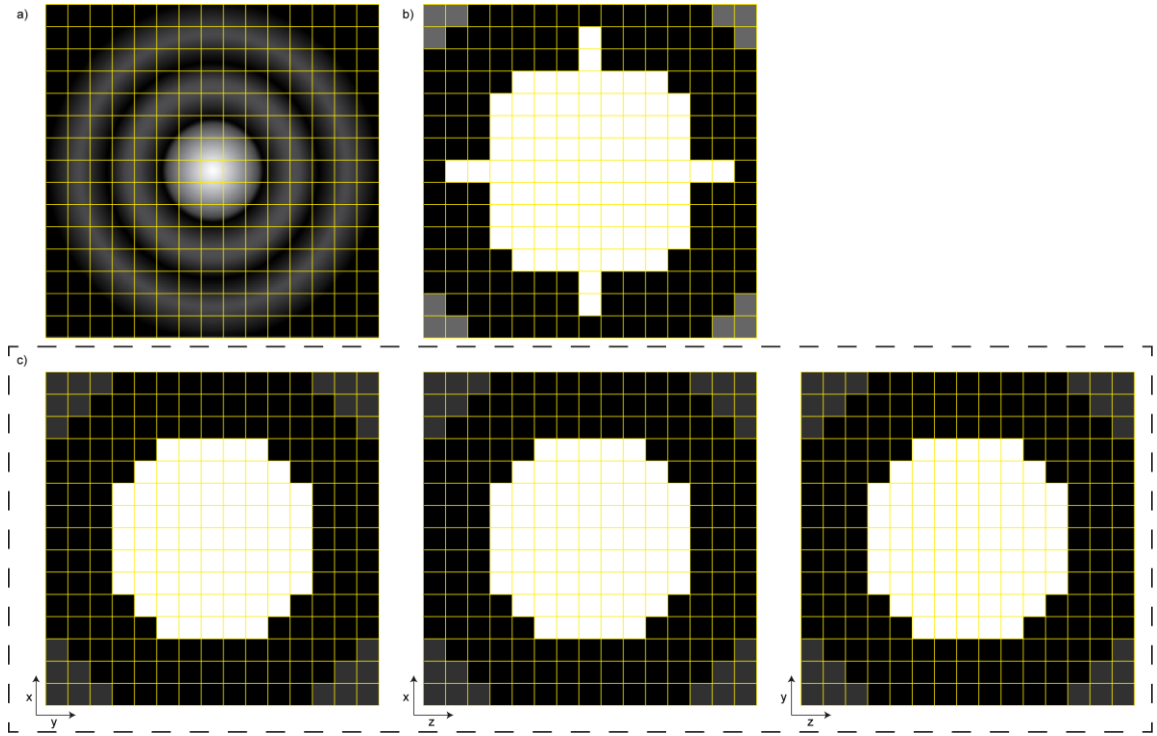


Figure 5.1: Comparison of Airy distribution and the 2D and 3D Haar-inspired feature. a) Example Airy distribution with clear circular shape. b) Example 2D Haar-inspired feature with approximated circular shape. c) Example 3D Haar-inspired feature in orthogonal views. Left: x-y, middle: x-z and right: y-z.

5.1.1.1 Signal Enhancement in 2D Image Data

To enhance the signal in a 2D image the Haar-inspired feature is used to measure local-contrast in each 2D pixel of an image (Figure 5.2a), over a range of spatial scales (Figure 5.2b right) with each spatial scale being weighted. The weights for each spatial scale are

determined from the user inputs of particle radius, R , and radius variability (as a percentage), V , using a normal distribution (Figure 5.2b left), where the maximum value (largest weight) of the distribution occurs at R and standard deviation of the distribution is defined using V . For efficiency, only the spatial scales within centre 99.7%, i.e. six standard deviations, of the distribution are used in the calculation, all other spatial scales are assumed to have zero weight. Finally, to combine all Haar-inspired pixel measurements from all spatial scales a maximum projection of all weighted local-contrast measures is taken to form a Haar-inspired local-contrast map (Figure 5.2c). Furthermore, it is also worth noting that the size of the radius of the particle to be detected does not have to be fixed within the detection process and it is possible to define a range of values for the radius, i.e. 3 to 7 pixels, or as multiple distinct values. This flexibility is beneficial if particles with different sizes are to be tracked in the same image dataset.

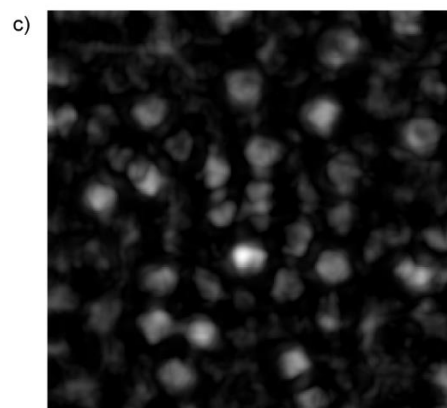
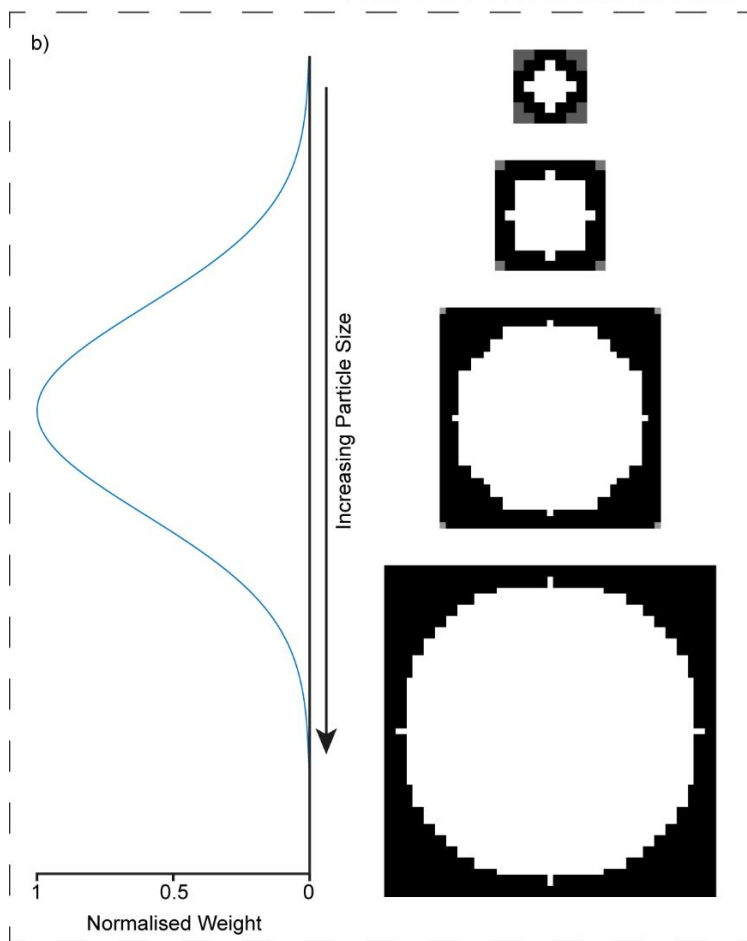
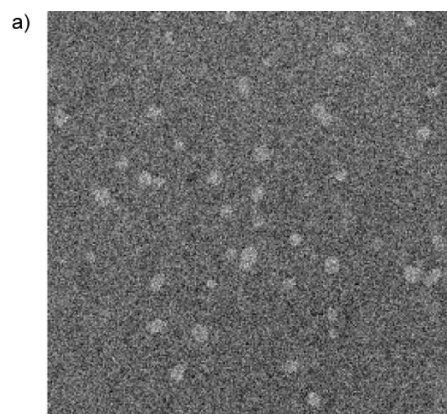


Figure 5.2: Example of local-contrast map generation in 2D using Haar-inspired features. a) Input grayscale image. b) Weighting scheme (left) applied to the different sizes of the Haar-inspired features (right). The weights are normally distributed and have a maximum at the user defined particle radius, with the width of the distribution also being user defined. c) The weighted convolution with Haar-inspired features at multiple spatial scales are combined linearly through the use of a simple mean.

As in Chapter 3, it is possible to generate a PPI from the Haar-inspired local-contrast map. However, as filtering using the Haar-inspired feature better matches the shape of the particles to be detected and, along with the use of weighting in the filtering methodology, the influence of particles that are not within the desired size range is reduced in the final Haar-inspired local-contrast map (Figure 5.3a). When compared to the Haar-like local-contrast map (Figure 5.3b). Furthermore, through using the Haar-inspired local-contrast map over the Haar-like local-contrast map mapping to a PPI is not necessary. The Haar-inspired local-contrast map (Figure 5.3a) provides more fine detail about the particles within the image when compared to the PPI (Figure 5.3c), these fine details are beneficial at later stages of the particle detection process.

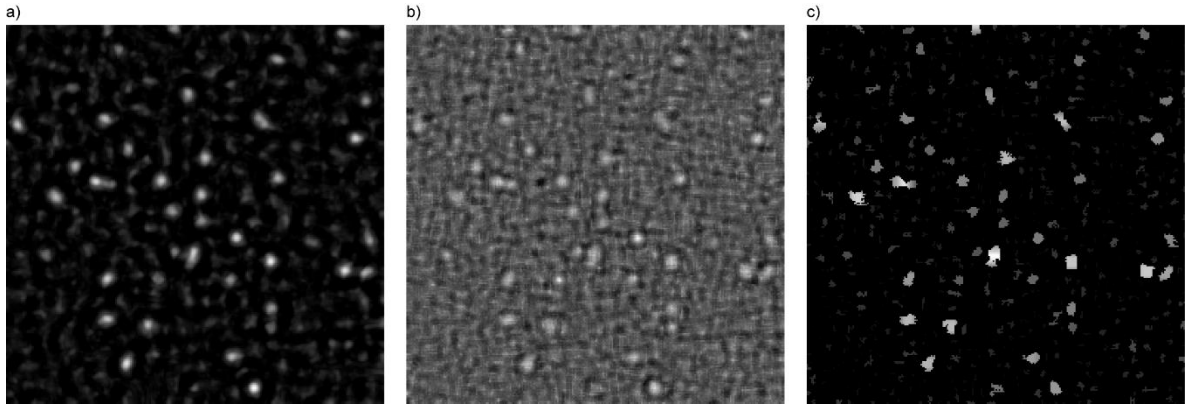


Figure 5.3: 2D comparison of Haar-inspired and Haar-like local-contrast maps and PPI. a) Shows the Haar-inspired local-contrast map which has greater signal enhancement when compared to the Haar-like local-contrast map in b) and more visible fine particle detail than the PPI in c).

5.1.1.2 Signal enhancement in 3D image data

Extension of the signal enhancement method to 3D image data using the Haar-inspired featured is fairly intuitive. As previously mentioned, in 3D image space the Haar-inspired feature takes the form of a sphere (Figure 5.1c shows the orthogonal views of the feature).

As in the 2D case a range of different sized 3D Haar-inspired features, the sizes of which are defined by the used input values R and V , are used to filter the image data with a weight applied to each different sized feature dependant on the user defined inputs. From here all the Haar-inspired measurements from different spatial scales are combined using a maximum projection to form a 3D Haar-inspired local-contrast map

5.1.2 Thresholding and Clump Splitting Segmentation

5.1.2.1 Thresholding in 2D and 3D image space

As the new signal enhancement method using the Haar-inspired feature is much more effective, segmentation of particles to form boundaries in both 2D and 3D image space can be performed by applying a global threshold. However, the key for accurate segmentation in using this method is determining an accurate threshold value, and this can often be very difficult. As such, to determine the threshold required the assumption that the histogram of the values with the 2D or 3D Haar-inspired local-contrast map can be split into two normal distributions is made; one relating to values arising from the foreground (particles) and one relating to values arising from the background (noise). Figure 5.4a gives an example of a 2D Haar-inspired local-contrast map in which the histogram of the values arising from the foreground and the background are both normally distributed, and as such they can be fitted with the sum of two Gaussian functions (Figure 5.4b). In image data, whether it be 2D or 3D, where the SNR conditions are extremely good, the threshold for segmentation is easily determined as the intersection of the two functions fitted to the histogram (Figure 5.4b, pink arrow), as there is no overlap of the two Gaussian functions. However, in real biological applications this is rarely the case. As the SNR of the image data decreases, the overlap between the two functions fitted to the histogram data increases and determining an accurate threshold becomes more difficult.

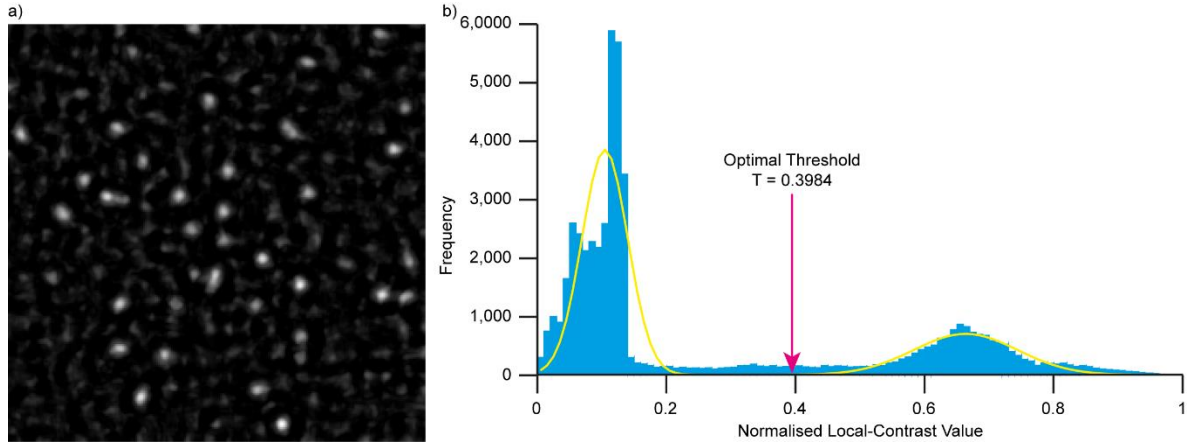


Figure 5.4: Simple foreground and background separability in Haar-inspired local-contrast map. a) Haar-inspired local-contrast map. b) Histogram from values from the Haar-inspired local-contrast map (blue bars). See that data can be fitted clearly by the sum of two Gaussian functions (yellow line). In this case the optimal threshold for segmentation can be used and is given at approximately 0.4 (pink arrow) where the two Gaussian functions are equal.

When overlap does occur between the two Gaussian functions fitted to the histogram data (Figure 5.5, orange line) the threshold used for segmentation can be defined using one of three different philosophies, the choice of which is dependent on the requirement of the current application. Firstly, the theoretical optimal threshold can be used, as before this is at the intersection of the two Gaussian functions fitted to the histogram of the Haar-inspired local-contrast map data (Figure 5.5, central arrow). However, when the optimal threshold is used with overlapping distributions, the results will contain both FP (spurious) and FN (missed) detections due to the inclusion of background pixels (Figure 5.5, yellow line) and the omission of foreground pixels (Figure 5.5, pink line). The quantity of each of these groups of fault detections being dependent on the size of the overlap between the two fitted Gaussian functions. The second philosophy that can be employed is to define a segmentation threshold in which all TP (correct) particle detections are included, regardless of the number of FP detections incurred. As such, the threshold using this philosophy is defined as $T = \mu_p - 3 \times \sigma_p$ (Figure 5.5, left arrow) where μ_p and σ_p are the mean and standard deviation parameters of the Gaussian function fitted to the histogram of the Haar-inspired local-contrast values arising from particles (Figure 5.5, pink line) and T is the threshold; assuming that particles have higher intensity values than their background. Conversely, the third way in which the threshold can be defined is using the philosophy that that all FP detections must be excluded, even at the expense of TP detections. As such the threshold using this philosophy is defined as $T = \mu_b + 3 \times \sigma_b$ (Figure 5.5, right arrow)

where μ_b and σ_b are the mean and standard deviation of the Gaussian function fitted to the histogram of the Haar-inspired local-contrast values from the image background. Again, the assumption here is that particles within the image data have higher intensity values than their background. Using the fitting of Gaussian functions to the histogram of the Haar-inspired local-contrast map also allows for the identification of situations where segmentation is not possible (or maybe extremely unreliable), in these cases the values of μ_p and μ_b would be close to being equal. When this situation arises, the data being investigated would be extremely noisy and may need to be re-evaluated for its suitability to be studied. Measurements extracted from data of this quality would most likely be very unreliable and lead to further errors in the trajectory linking process. Again, any of these philosophies for determining a threshold for segmentation can be applied to either 2D or 3D image data.

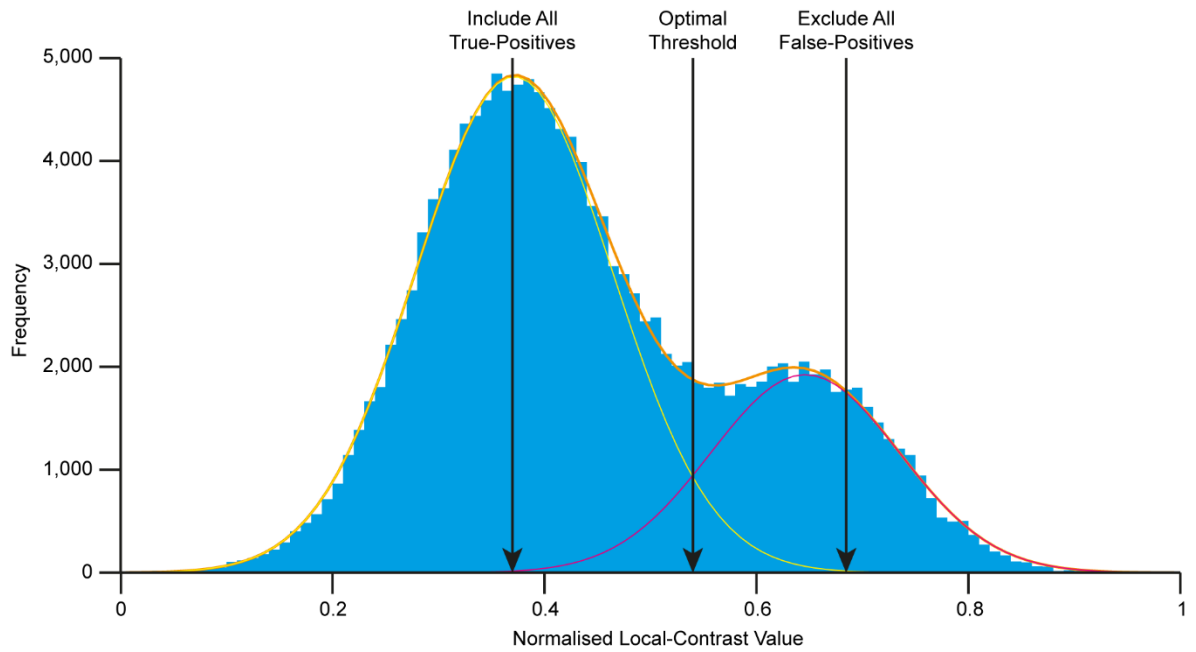


Figure 5.5: Example of a more complicated histogram of Haar-inspired local-contrast values. Here the optimum threshold can still be defined as the point where the two Gaussian functions fitted to the histogram data (orange line) are equal, but use of this threshold will include both spurious and missed detections. Alternative thresholding philosophies are to all foreground particle pixels (pink line) at the cost of including some spurious detections. Conversely it is possible to exclude all background particle pixels (yellow line) at the cost of missing some detections. The application of the method and the needs of the user has to be considered when having to define a threshold for segmentation when the histograms describing foreground and background pixels overlap in this way.

5.1.2.2 Clump splitting in 2D image space

However, generating particle boundaries through thresholding does not intrinsically allow for the detection of single particles, as such the resultant boundaries may contain more than one particle. For the identification of single particles, a further clump splitting step is required. Firstly, an estimate of the location and quantity of particles within all the particle boundaries generated through the thresholding process is gaged using local maxima detection within the Haar-inspired local-contrast map. Using the position of these local maxima within the particle boundaries clump splitting can be achieved using one of the following two methods. Firstly, a marker-controlled watershed transform can be performed, as previously described in section 3.1.3.1, using the local maxima positions (and no other restrictions) combined with the gradient of the Haar-inspired local-contrast map. However, in this application only the watershed lines from the watershed transform are required. These watershed lines are then applied to the particle boundaries obtained from thresholding process thus dividing the boundaries into single particles (Figure 5.6b). The second method is to compute a Voronoi tessellation of the local maxima positions and apply the regions obtained from this method to the particle boundaries obtained from the thresholding process [82]. The Voronoi tessellation does not include any further image information in its calculation and is a purely mathematical representation of the optimal splitting of the image data into 2D regions based on the Euclidean distance between the local maxima positions (Figure 5.6c).

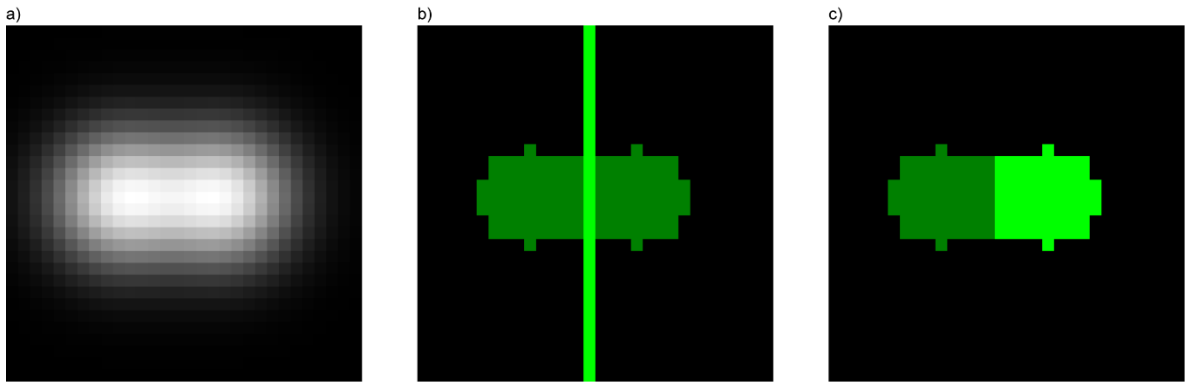


Figure 5.6: Example of 2D clump splitting methods. a) A synthetically generated example of two equal overlapping 2D particles with symmetric Gaussian profiles. b) Result of using marker-controlled watershed clump splitting where a line of separation must be defined. Here the resultant particles (dark green) are not equal as the watershed line (bright green)

takes the place of some of the pixels belonging to the particle on the right. d) Result of using Voronoi tessellation for particle clump splitting. Here the particles (two shades of green) are equal shapes, as expected, as a line of separation between the particles does not need to be defined as the particles are touching.

5.1.2.3 Clump splitting in 3D image space

In 3D image space the main concept that needs to be understood is that the extension of the lines, generated using the watershed now become planes and the regions generated using the Voronoi tessellation become volumes. The local-maxima used as input for both of these methods is now also calculated in 3D space, with the maxima identified as a voxel as opposed to a pixel. With the watershed method, the generated planes would now divide the clumped particles volumes generated in the thresholding process to generate particle volumes containing only single particles. The Voronoi tessellation method would work in completely the same way with the 3D Euclidean distance between points being used for the calculation of the tessellation, which now become 3D volume as opposed to 2D regions.

5.1.2.4 Choosing the correct clump splitting method

The key parameter to consider when choosing which clump splitting method to implement is R as described at the start of the detection process i.e. how many pixels or voxels a particle typically covers. Whilst the marker-controlled watershed method is typically the more accurate of the two methods, it has the requirement of defining a watershed line in 2D image data (or a plane in 3D image data) (Figure 5.6b, bright green line), which must be at least one pixel wide and acts as separation gap between clumped particles. If two particles are touching or overlapping (Figure 5.6a), the pixels (or voxels) used to form the watershed lines (or planes) have to be taken from the pixels (or voxels) defining the area (or volume) of one or more of the clumped particles, in doing so this will cause errors in the final localisation of the clumped particles. The extent of the localisation error induced by the use of the watershed method increases as the value of R decreases. This is because the proportional percentage of pixels (or voxels) taken from the particle boundary to form the

watershed line (or plane) increases (Figure 5.7, column ii). As the Voronoi tessellation method allows for the identification of single particles that can be touching (Figure 5.6c), i.e. the method requires no gap, the total area (or volume) of the clumped particles is maintained even after the clump splitting process (Figure 5.7, column iii). However, as no other image information is used, clump splitting with the Voronoi tessellation method may not be as accurate when the application is to split many particles, but this segmentation error can be minimised as the Voronoi tessellation method needs only be applied for clump splitting of particles with smaller values of R . In these applications particle boundaries are already difficult to define. Hence, the proportional error caused using the Voronoi tessellation method over the watershed method is offset by the extra information that becomes available for describing the particle features that will be used in the trajectory linking process.

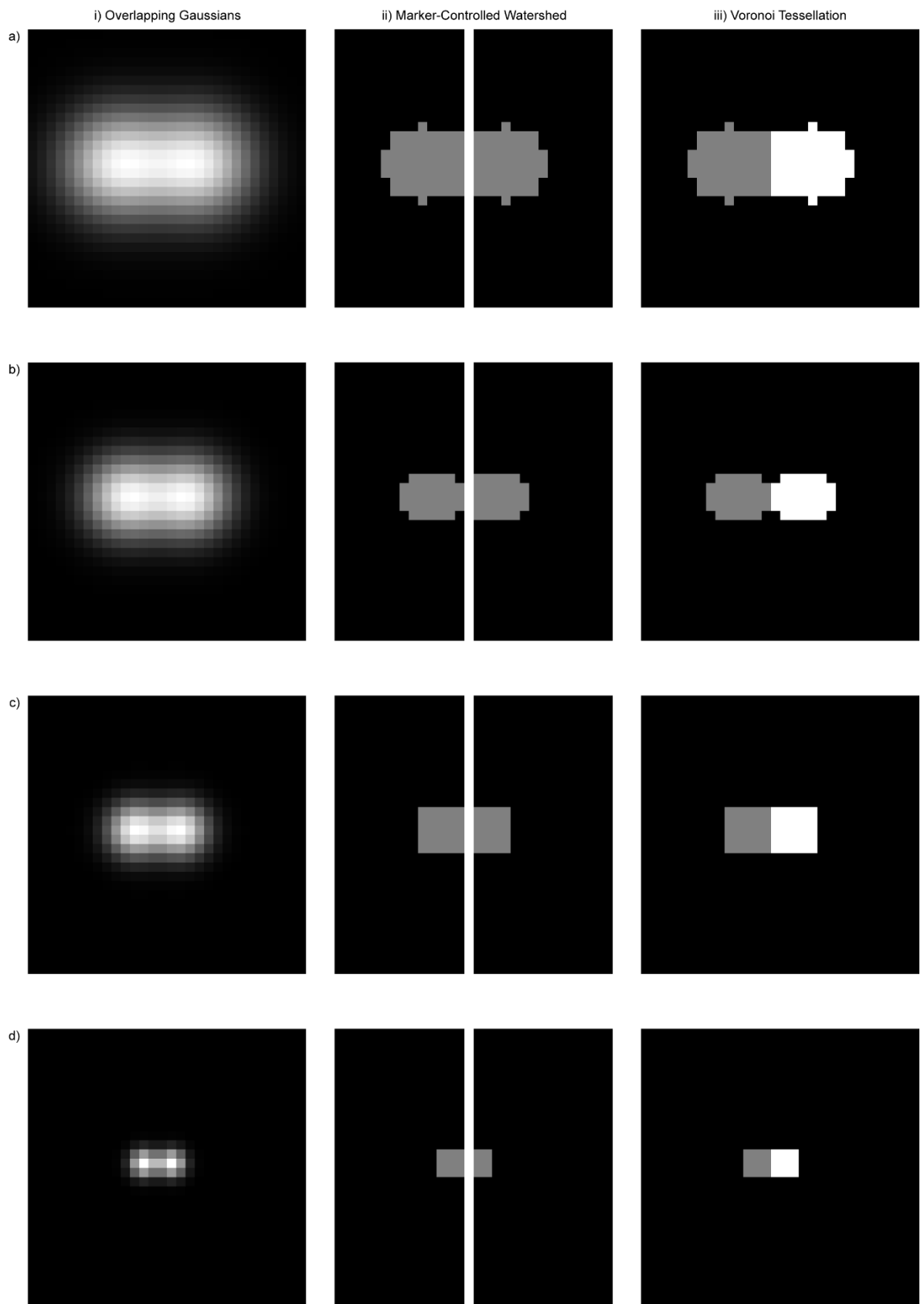


Figure 5.7: Comparison of both watershed and Voronoi tessellation clump splitting techniques for reducing particle size. i) Column shows the touching equal sized particles with symmetric Gaussian profiles requiring clumping splitting, the particle

size decreases in each row. ii) Column shows the results of clump splitting with marker-controlled watershed. iii) Column shows the results of clump splitting with Voronoi tessellation. As seen in column ii) clump splitting with the marker-controlled watershed method causes an asymmetry between the two particles as the line of separation must be taken from one of the particles. This asymmetry results in a localisation error in one or both particles, with the effect increasing with decreasing particle size. As Voronoi tessellation allows to define touching particles the split particles have more accurate particle shapes.

5.1.3 Particle Localisation

5.1.3.1 Localisation in 2D image data

For 2D image data localisation is determined by 2D Gaussian fitting, in doing so assumptions are made about the appearance of the particles being detected within image i.e. they can be approximated to 2D Gaussian distributions, with minimal error. Here the NLLS minimization method for 2D Gaussian fitting [37]. As Gaussian fitting methods have the benefit of being able to localise the peaks of both symmetric and asymmetric Gaussians (Figure 5.8c and d) it makes the detection and localisation method more applicable to more applications.

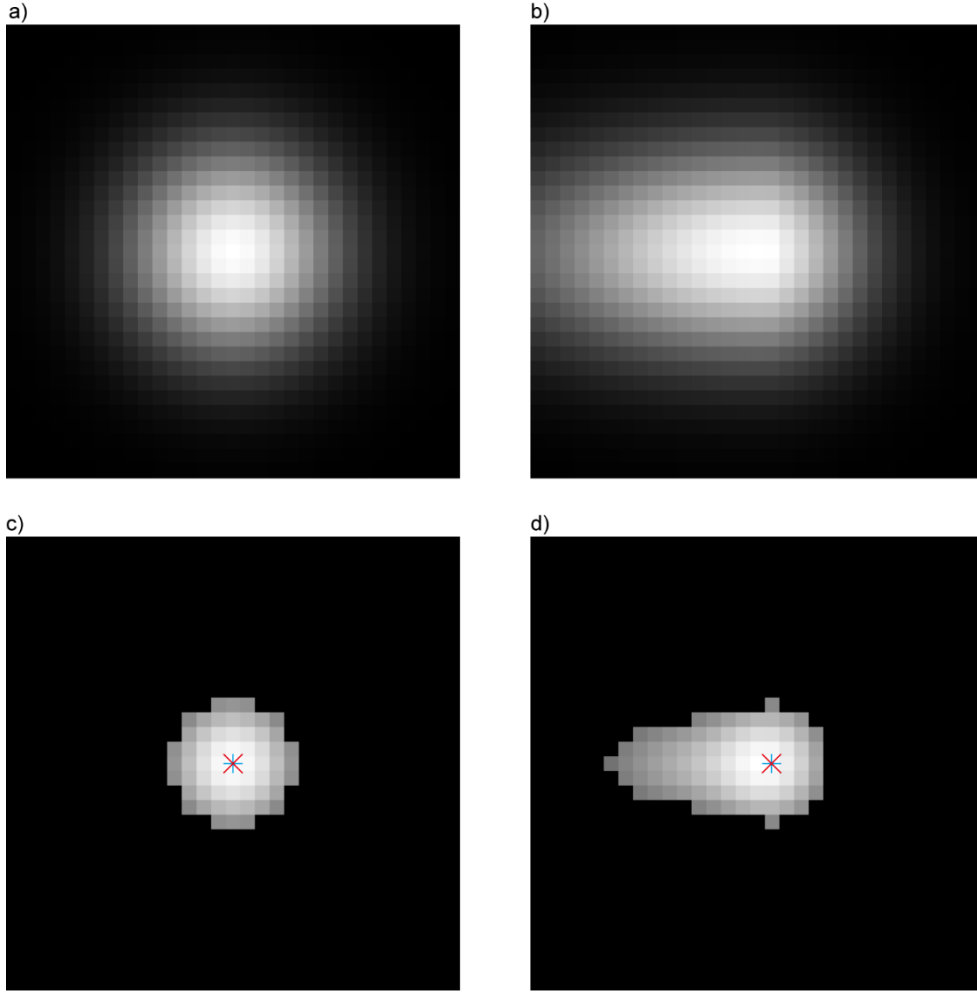


Figure 5.8: Comparison of localisation results on 2D symmetric and 2D asymmetrical Gaussian particles using 2D Gaussian fitting method. a) Symmetrical 2D Gaussian distribution. b) Asymmetrical 2D Gaussian distribution. c) and d) Show localisation result using the 2D Gaussian fitting method (red cross) in comparison with GT (blue cross). See how this method is capable of accurately identifying the true particle localisation in both cases, this a clear improvement on the centre-of-mass localisation method utilised in Chapter 3.

5.1.3.2 Localisation in 3D image data

The particle localisation for 3D image data is determine using the centre-of-mass method weighted with values from the Haar-inspired local-contrast map. The co-ordinated localisation of the particle is given as:

$$\begin{bmatrix} x_c \\ y_c \\ z_c \end{bmatrix} = \frac{\sum_{i,j,k \in R} \begin{bmatrix} x_i \\ y_j \\ z_k \end{bmatrix} H(i,j,k)}{\sum_{i,j,k \in R} H(i,j,k)}$$

(5.1)

Where, x_c , y_c and z_c are the calculated sub-pixels localisations of the centre of mass, i , j and k are the x , y and z indices of the values within the segmented region R within the Haar-inspired local-contrast map, H .

5.2 Trajectory Linking

Our new trajectory linking method extends, improves and enhances the feature point trajectory linking method initially described in [32]. The original method originally describes trajectory linking using particle location (XY co-ordinates) and two particle features; describing intensity moments of the order zero and two. Our trajectory linking method presented here extends and improves the quantity and type of particle features to be measured and included within the state space variable. Motion modelling is also incorporated into the methodology to improve the trajectory linking process and the ability the ability to handle 3D image data.

5.2.1 State space variable

As before the state space variable is utilised to minimise the “distance” between measurements extracted from particles that appear in adjacent frames. However, unlike before weighting can be applied to give preference to any extracted measurement or group of measurements.

5.2.1.1 State space variable for 2D image data

As initially described in section 3.2.1.1 the state space variable is first extended to include measurements describing the particle features area, A , the number of pixels contained within the particles perimeter. The bounding box area, A_B , the number of pixels contained within the dashed yellow line of Figure 5.9. The length of the major and minor axis, d_M and d_m , (Figure 5.9 red and blue arrows, respectively) and the particle perimeter, A_P , length of orange line in Figure 5.9. For each particle, intensity measurements describing the mean

and maximum pixel intensity, I_μ and I_{max} , within the particle boundary (perimeter) are included. For the new trajectory linking method described here, extending the quantity of particle features further the state space variable now includes a more complex morphological measurement describing the particle area; the area contained within the convex hull of the particle, A_H (Figure 5.9, green line) [83]. Also, incorporated into the state space variable are measurements to describe multiple characteristics of a particles shape, they are circularity, f_{circ} , aspect ratio, A_R , solidity, C_H , and bulkiness, B , the equations for which are given below.

$$f_{circ} = 4\pi \frac{A}{A_p^2} \quad (5.2)$$

$$A_R = \frac{d_m}{d_M} \quad (5.3)$$

$$C_H = \frac{A}{A_H} \quad (5.4)$$

$$B = \frac{d_m d_M \pi}{A} \quad (5.5)$$

An additional variable describing the intensity profile of each particle is also included in the state space variable, the standard deviation of the fitted Gaussian, σ . It is also possible to include comparative measurements of “intensity” from the Haar-inspired local-contrast map in combination with (or in place of) the intensity measurements from the input grayscale image data. The use of local-contrast values would be particularly advantageous in high noise environment as the measurement of local-contrast is more robust measurement than intensity in these high noise environments.

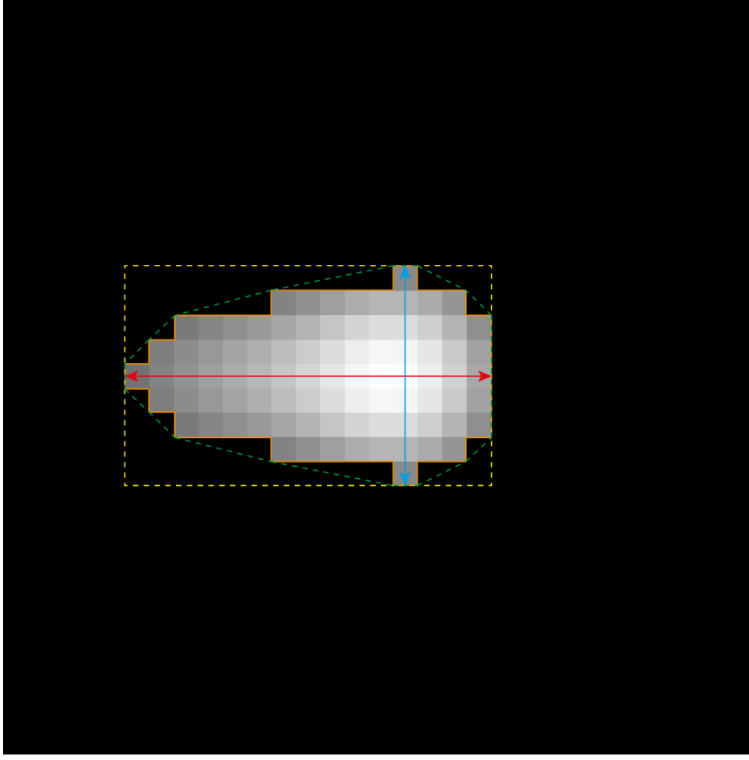


Figure 5.9: Schematic of measurements used for trajectory linking. Dashed yellow line represents the bounding box of the particle of which the area is used in the particle linking process. The orange line represents the perimeter of the particle the length f which is used in the particle linking process. The pixels contained within this line also described the particles area. The dashed green line represents the convex hull of the particle of which the area it contains is used for particle linking. The red and blue headed arrows represent the major and minor axis lengths respectively of the particles and are also included in the state space variable for particle linking.

5.2.1.2 State space variable for 3D image data

For trajectory linking in 3D image data these particle feature measures also need to be extended into 3D. Intuitively the 2D measure of particle area now becomes particle volume, A_3 . The 2D measurement describing the area contained within the bounding box, now becomes the volume contained within the bounding volume, A_V . The measurements for the major and minor axis lengths remain the same although now taken in 3D space and the measurement of the particles perimeter now becomes a measure of the particle surface area, A_S . The area contained within convex hull of the particle, A_H , now becomes the volume contained within the convex hull, with the convex hull algorithm now being extended to 3D image space. The calculation of the measurements to describe the characteristics of the particles shape remain the same, with the exception of circularity, f_{circ} , which now becomes sphericity and is defined as:

$$f_{spher} = \sqrt[3]{\frac{36\pi A_3^2}{A_s^3}}$$

(5.6)

Where in 3D space A_3 refers to the particle volume and P refers to the particle surface area. The general intensity measurements incorporated into the state space variable remain the same but instead are taken from the 3D particle volume whilst an additional measurement of intensity at the centre-of-mass is also included.

5.2.1.3 Weighting of state space variable

It is now also possible to add a weighting scheme to the values within the state space variable. These weights are currently user defined, with automatic weighting to be investigated as further work. Applying weights allows for preference to be given to either the group of morphological or intensity measures, or indeed specific measures within each of these groups, dependant on the data under investigation. This is particularly beneficial in applications where particle density is high and/or particles only cover a few pixels or voxels; in these conditions, it is preferential to give more emphasis to the intensity (local-contrast) based measurements within the state space variable. As previously described, clump splitting techniques used within the detection algorithm can give rise to errors in particle segmentation and hence the morphological based measurements can become less reliable. Alternatively, it is advantageous to give more emphasis to the morphological based measurements in images that are corrupted by high levels of noise, as the intensity measurements are not as reliable. This is due to the pixel values arising from noise typically being high and thus having a significant effect on the mean and maximum particle intensity values. Using these extended particle feature measurements becomes more pertinent in the initial stages of the particle linking process, when the motion of the particles is unknown and (by default) is assumed to be Brownian. Furthermore, in comparison to the particle linking method described in section 3.2.1 the number of particle features incorporated into

the state space variable has little effect on the processing time required to complete the particle linking process.

5.2.2 Motion Modelling

The motion models within this trajectory linking process assumes that at any given point in time a particle is undergoing one of two possible types of motion; Brownian motion or linear motion [50]. The motion model used for each link within a trajectory is determined by motion of the particle in its immediate previous two links. As the motion modelling requires two previous links to determine which motion model to use it is only implemented from the third link of the trajectory linking process, as clearly the prior required information is not available. In this case the two initial links the motion of a particle are assumed to follow the Brownian model by default, however, it is possible for the user to choose the linear motion model if desired. In the linear motion case, the first link is still assumed to follow the Brownian motion model before switching to the linear motion model for second link and subsequently allowing switching between the two motion models for the remainder of the linking process. Only requiring two previous links to determine which of the motion models to apply to the particle linking process allows for the investigation of the fast switching dynamics of particles. The identification of these fast switching properties is particularly beneficial as advancements in detector and imaging technologies allow for acquisition of images at faster and faster framerates.

5.3 Performance Evaluation on Synthetic Images

As in Chapter 3, the performance of the tracking method is validated on 2D and 3D image data using a range of synthetically generated images, in this way a comparison between the performance of the method with 14 other state-of-the-art tracking methods is possible.

5.3.1 Synthetic Datasets

As before validation of the tracking method is undertaken on the synthetic datasets supplied by the “ISBI 2012” for their particle tracking challenge [70]. As the new particle tracking method is capable of both 2D and 3D particle detection and trajectory linking all available datasets are used for a complete validation and comparison of the method. The imaging scenarios “vesicles” (Figure 5.10a) and “receptors” (Figure 5.10b) (see section 3.3.1 for details) are included along with the previously unused imaging scenarios “microtubules” (Figure 5.10c) and “3D viruses” (Figure 5.10d). The microtubules datasets are modelled to have directed motion in 2D image space, whilst the viruses are modelled to have motion that switches between Brownian and directed motion in 3D image space. As before all imaging scenarios consist 12 distinct datasets with each dataset having one of three particle densities; high, medium or low and one four different SNRs; 1, 2, 4 or 7 (Figure 5.10). The SNR of all datasets was calculated using the same intensity based method in section 3.3.1.

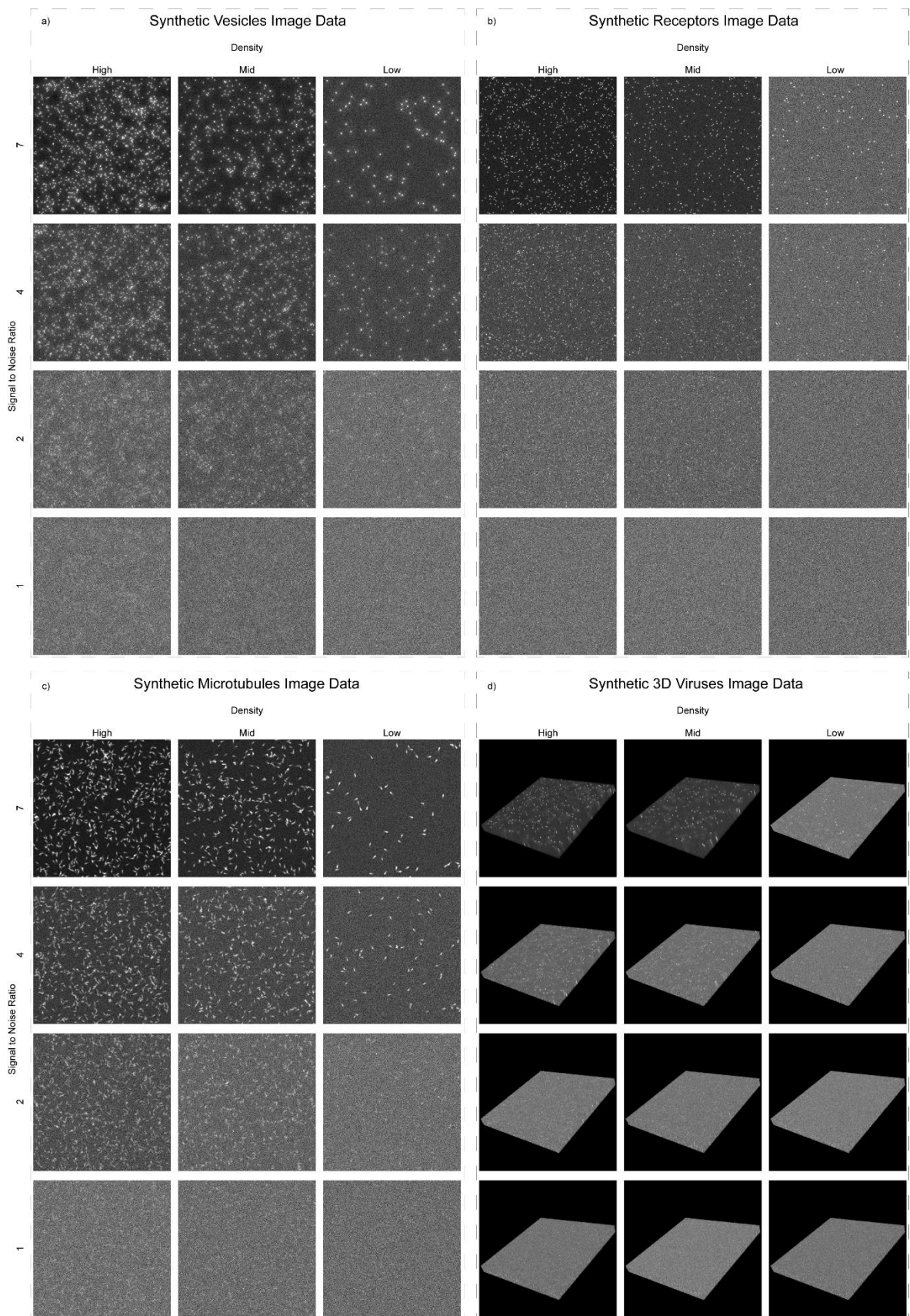


Figure 5.10 Sample image all datasets investigated. a)-d) The different imaging scenarios modelled by the synthetic image data. a) Sample images from the synthetic vesicles datasets. b) Sample images from the synthetic receptor datasets. c) Sample images from the synthetic microtubules datasets. d) Sample image volumes from the synthetic 3D viruses' datasets, each volume contains 10 images. In each panel the particle density decreases in the columns from high to mid to low density, with high density representing 1,000 particles per image and mid and low density representing 500 and 100 particles per image respectively. The rows of each panel represent the SNR levels of each imaging scenario with the SNR decreasing from 7 to 4, 2, and 1.

5.3.2 Comparison with State of the Art Methods

The performance of the method is made with the 14 state-of-the-art methods that competed in the ISBI particle tracking challenge, as in Chapter 3 [70]. To measure and compare the performance of the tracking method the same 5 performance metrics are utilised; alpha, α , beta, β , the JSC for track points, JSC , the JSC for entire tracks, JSC_θ , the error of localisation, $RMSE$ (for full details on how these metrics are measured see section 3.3.2). Again, the timing metric is omitted as comparative hardware is not available which would result in an unfair comparison of timings.

5.3.3 Results

With five performance metrics, four imaging scenarios, three particle densities and four SNRs there is a total of 240 measures for comparison of performance. For ease of comparison again box plots are used to summarise the results of the 14 methods that competed in the ISBI particles tracking challenge [70]. The centre of each box within the plot represents the mean value achieved by the 14 competing methods for that metric on that dataset, the edges of the boxes extend one half a standard deviation from the mean, giving a total box length of one standard deviation. The whiskers of the box plots extend to the minimum and maximum values achieve by the competing methods on that dataset for that metric. The performance of the method is represented by a blue line overlaying the box plots. For fair comparison, and in accordance with the original particle tracking challenge, the results are generated using the challenge image data using the optimal

parameters determined using the training data. For the purpose of discussing the results in a more easily understandable way they are separated by performance metric.

Firstly, the alpha metric, which has a maximum at one and a minimum at zero, measures the accuracy of the correct tracks identified by a tracking method (Figure 5.11). Examining first the vesicle datasets the method achieves seven of a possible 12 number one rankings, being on average 2% better for the high-SNR levels on low- and high-density data, and 10% better for the high-SNR mid-density datasets (Figure 5.11a). For lower-SNR datasets the results were on average 7% worse than the highest achieved result, however they were above the average result achieved by the competing methods. For the microtubules datasets, the method does not perform as well, it does not achieve any number one rankings and on average the results were 13% lower than the highest achieved result (Figure 5.11b). However, the results were consistently higher than the average achieved result on the datasets where the SNR was greater than one. When the SNR is equal to one the results were 5%, 15%, and 30% lower than the mean value achieved by the competing methods for the low, mid and high density datasets respectively. For the receptors datasets, the method achieves five out of a possible 12 number one rankings, joint equal with method 11 (Figure 5.11c). Notably, the method performs less well in comparison to the other competing methods on low-density datasets achieving a little over average on most of these datasets. However, when SNR is equal to two it achieves a below average result. In contrast, on the medium density datasets, with the exception of when the SNR is equal to one, the method performs substantially better, achieving on average a result 10% higher than the previous best result. Finally, for 3D viruses' datasets on the alpha metric the method achieved eight of 12 possible number one rankings, with results on average around 15% better than the next higher result (Figure 5.11d). Again, the method performs comparatively less well on data at lower-SNR levels. Here results are on average being about 10% lower than the highest achieved result. Even with these small variations in performance it is important to draw attention to the fact that the method only truly struggled on datasets where the SNR is equal to 1 and typically data of this quality would very rarely be used for any real biological applications.

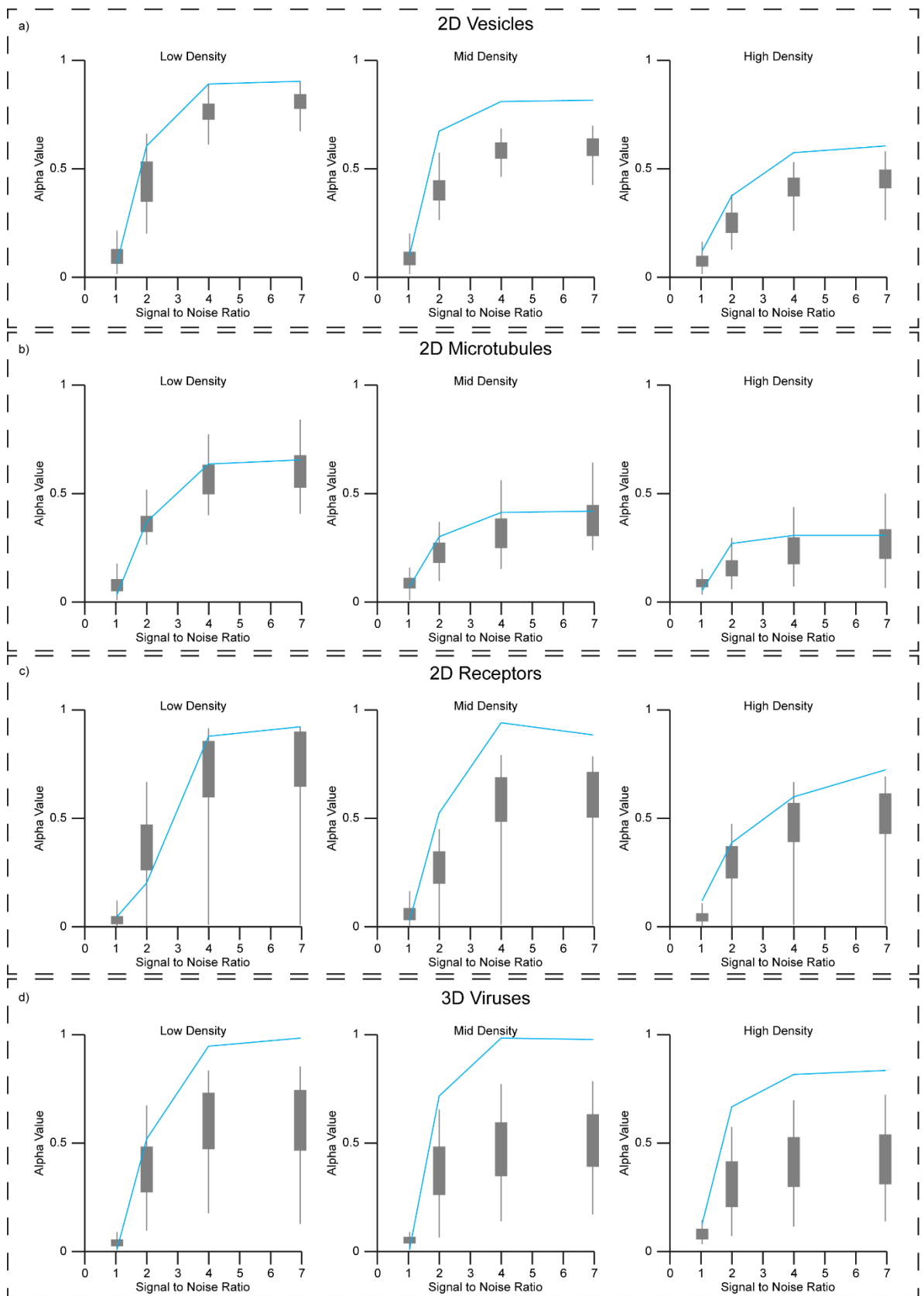


Figure 5.11: Performance of the tracking method measured using the alpha metric on a) 2D vesicles, b) 2D microtubules, c) 2D receptors and d) 3D viruses synthetic image datasets. In all panels the density of the particles move from low to high

as you move left to right. In each graph the SNR increases as to move left to right along the x-axis. Of note the method described here performs well above the next best performer on datasets with SNR >1 and mid density on the imaging scenarios vesicles, receptors and 3D viruses as well as high density 3D viruses. On all other datasets with SNR >1 the method achieved an at least average performance. When SNR is equal to 1 the method struggles in comparison to the other methods but this kind of data is unrealistic for real world applications.

As mentioned in Chapter 3 because of the close relationship between the alpha and beta metrics the pattern of the distribution of results is much the same. The beta metric has a maximum value at its corresponding alpha metric and a minimum value at zero. A higher difference between the alpha and beta metrics is indicative of a larger number of false tracks, as the beta metric penalises for the generation of these false tracks. For the synthetic vesicle image data (Figure 5.12a) the method achieves eight out of 12 number one rankings. Again, the datasets where a number one ranking was not achieved are typically of lower-SNR, with the exception of low-density vesicles with SNR of 7 where the number one ranking was missed by 0.05, a very small amount for a dataset where all methods performed well. In the lower-SNR datasets where a number one ranking was not achieved the results were still above the average achieved by the other competing methods with which the comparison is being made. Furthermore, the difference between the alpha and beta metrics on these dataset is low indicating that it is an inability to identify true tracks leading to less than optimal performance rather than the generation of false tracks. Notably, the performance of the method on the mid density datasets was around 0.1 better than the best result achieved by the other methods competing on the datasets with SNR equal to 2, 4 and 7, a significant improvement. For the microtubules datasets, where the method again appears to be less strong, only one number one ranking was achieved (Figure 5.12b). The most number one rankings were achieved by method 4, a specialised microtubule tracking method that did not compete on any of the other imaging scenario datasets in the challenge. However, the method is on average better than the mean results achieved by the competing methods and, in comparison with the results achieved on the alpha metric the differences are very small, meaning that the tracks identified are, on the whole, correct with very few incorrect tracks reducing the beta metric in comparison to the alpha metric. Moving on to the performance of the method on the receptors datasets (Figure 5.12c), the method takes six on the possible 12 number one rankings. Here the number one rankings of the method spans a range of SNR levels, however the method does seem to struggle with the datasets

of low density, in comparison to the other competing methods. On average the decrease from the maximum achieved results on this low density data is about 15%, but the results are consistently about the average result obtained. Finally, for the 3D viruses' data, the method achieved eight out of a possible 12 number one rankings with method five achieving the other four number one rankings. Furthermore, the reduction between the alpha and beta metric is very low, showing that the method is able to correctly identify tracks in this higher dimensional data without the generation of false tracks.

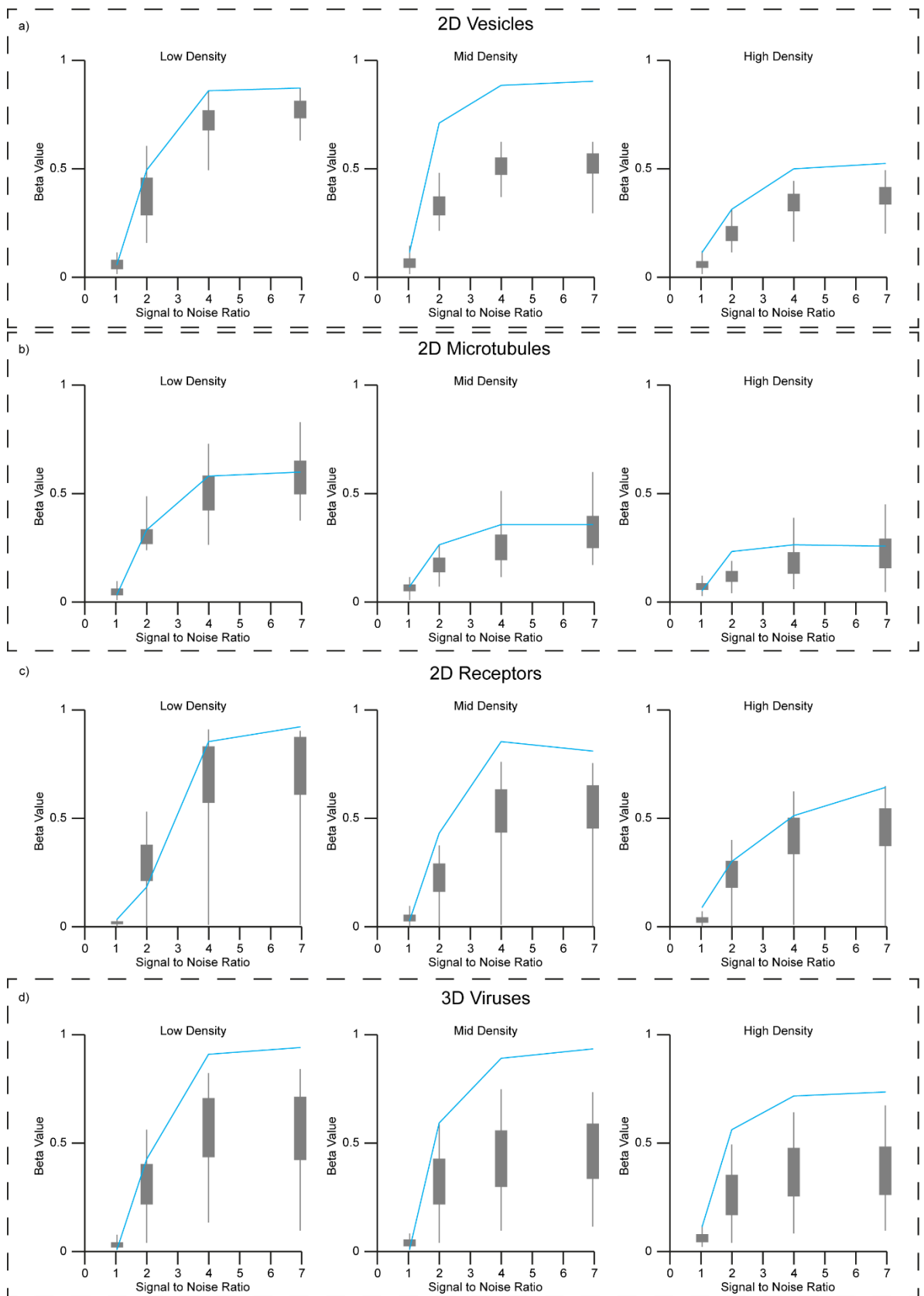


Figure 5.12: Performance of the tracking method measured using the beta metric on a) 2D vesicles, b) 2D microtubules, c) 2D receptors and d) 3D viruses synthetic image datasets. In all panels the density of the particles move from low to high as

you move left to right. In each graph the SNR increases as to move left to right along the x-axis. Again, due to its close relationship with alpha metric the method described here performed at on average with all our methods on datasets with SNR >1. Exceptional performance is again seen on the mid density vesicles, receptors and 3D viruses, as well as high density 3D viruses.

The next metric for comparison is the JSC metric, this metric is a measure of a tracking methods ability to correctly identify detections within the synthetic data (Figure 5.13). For the vesicles datasets, the method achieved seven of the possible 12 number on ranking (Figure 5.13a). Again, the method struggled at the lowest SNRs present by the challenge. However, the results on this low-SNR data were consistently above the mean of the values achieved by the other competing state-of-the-art methods. For the synthetic microtubules datasets, where the method struggled with the alpha and beta metrics, the JSC metric for the method achieved more number one rankings than for the alpha and beta metrics. This shows that the detection is efficient even if it is not overly accurate using distance measures (Figure 5.13b). The method achieved 2 number one rankings for the synthetic microtubules datasets. For the receptors datasets, the method achieved six of a possible 12 number one rankings (Figure 5.13c). The method again struggled to correctly detect particles at the lowest SNR levels. Finally, examining the 3D viruses' datasets the method achieves fives of the possible 12 number rankings. In the 3D viruses' datasets where a number one ranking was not achieved the method achieved a value well above the mean achieved by the other competing methods and, in many cases, was very close to the maximum achieved by the competing methods (Figure 5.13d). The number of true detections identified when using the JSC metric is of key importance as it is these detections that are used for the later RMSE metric to determine the accuracy in the localisation of the tracking method. A low number of true detections can lead to a false assumption on the accuracy that the tracking method can achieve, ideally the number of true detections should to be as high as possible so the RMSE has a large enough sample to infer a reliable result in the RMSE metric.

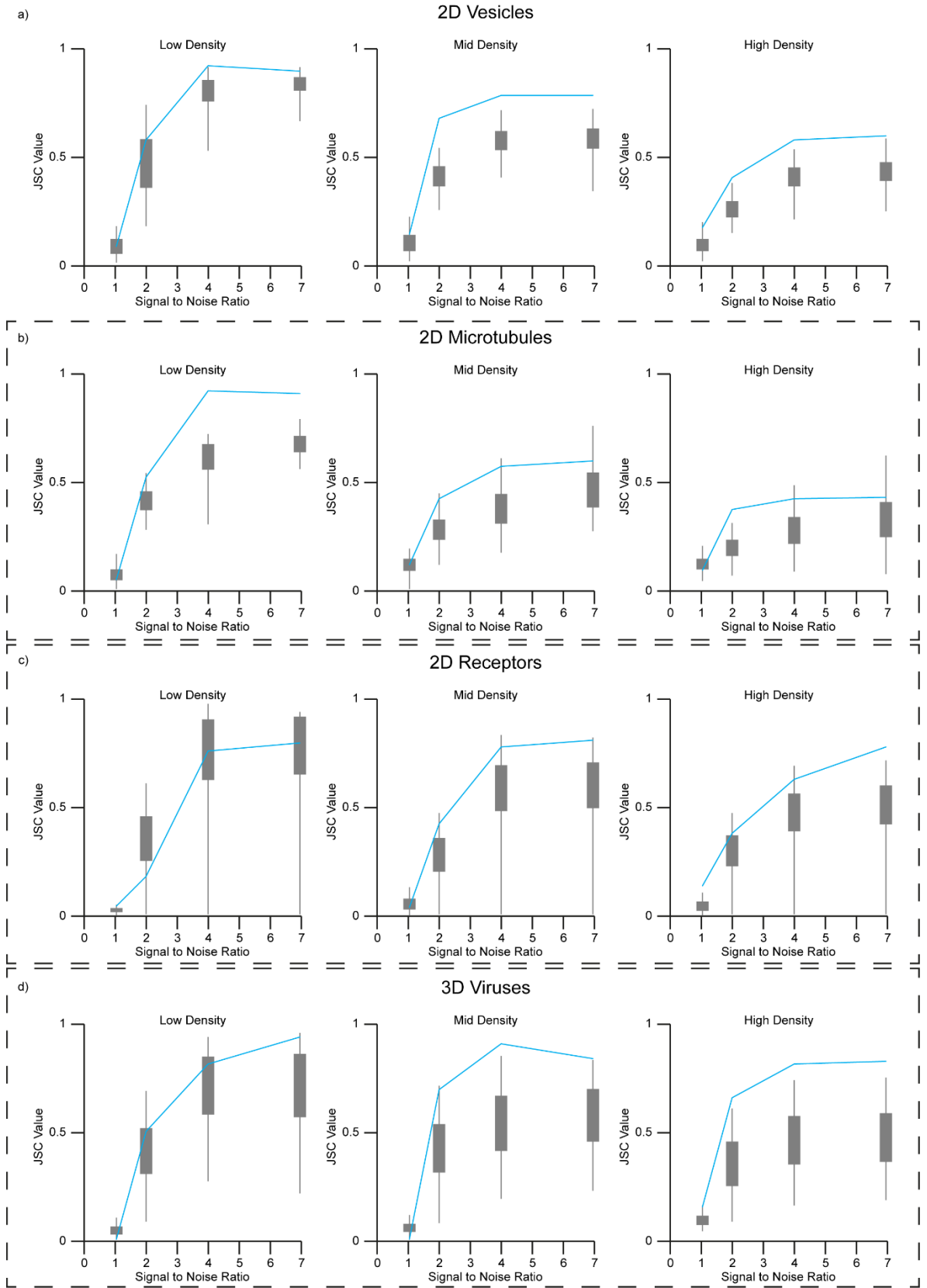


Figure 5.13: Performance of the tracking method measured using the JSC metric on a) 2D vesicles, b) 2D microtubules, c) 2D receptors and d) 3D viruses synthetic image datasets. In all panels the density of the particles move from low to high as

you move left to right. In each graph the SNR increases as to move left to right along the x-axis. Due to the more simplistic nature of the JSC metric the method described here as a more average relative performance. However, performance on mid density vesicles is again very good, the best for SNR >1, as well as mid and high density 3D viruses for these SNR levels. Also pleasing is the results on the low density microtubule data.

Similar to the JSC metric the JSC_0 metric is used to measure how well a tracking method can identify true tracks without missing tracks or generating false tracks at the same time (Figure 5.14). For the synthetic vesicles datasets, the method achieves eight of a possible 12 number one rankings, with methods 13 and 7 sharing the other four number one ranking spaces (Figure 5.14a). When the method does not achieve the number one ranking it is again typically at the lower-SNR levels, here the average difference between the score achieved by the method and the number ranked method is around 5%. However, as with all previous cases of missing the top ranking position the result the method achieves is above the mean result achieved by the other competing methods. For the microtubules datasets, the method achieves eight out of 12 number rankings reiterating the ability to form tracks in an efficient manner even when the distance measures used for single detections are not overly accurate (Figure 5.14b). Where a number one ranking was not achieved, the methods performance was around 10% lower than the best performing method on those given datasets, however are achieved performance was above the mean achieved by the competing methods. Moving onto the receptors datasets the method again achieves five out of a possible 12 number one rankings (Figure 5.14c). The method again struggles at low density and low-SNR in comparison to the other competing methods with results being on average 10% lower than the highest achieved result when the method is not ranked number one. However, as with all other datasets and metrics the values achieved are above the mean result achieved by the other competing methods. Finally, for the synthetic 3D viruses' datasets the method achieved nine of a possible 12 number rankings, with the remaining number rankings being taken by method 5 (Figure 5.14d). Again, low density or low-SNR datasets being problematic for the method, in these datasets where the method was not ranked number one the number one ranking was missed on average by 15%. Furthermore, more worryingly for the low and mid density dataset with SNR equal to 1 the result was the lowest of the eight methods that competed on these datasets.

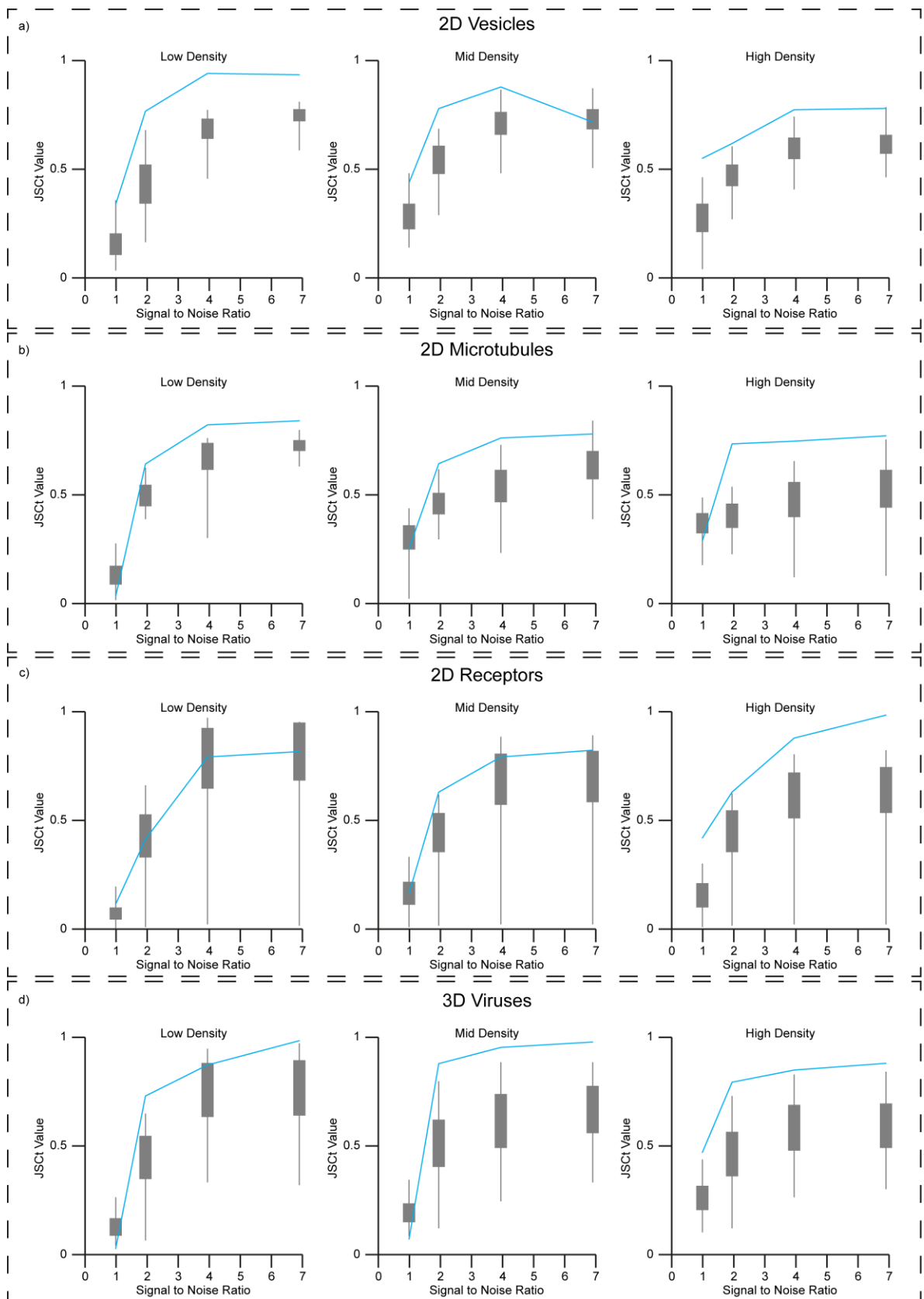


Figure 5.14: Performance of the tracking method measured using the JSCt metric on a) 2D vesicles, b) 2D microtubules, c) 2D receptors and d) 3D viruses synthetic image datasets. In all panels the density of the particles move from low to high as

you move left to right. In each graph the SNR increases as to move left to right along the x-axis. Here the performance of the method is strong on most datasets. However, low density datasets modelling receptors and viruses appear to be problematic for the method as well as datasets where SNR is equal to 1.

The final metric used in the comparison is the metric RMSE (Figure 5.15). This metric is measured in pixels and has a maximal value at 5, the maximum pairing distance allowed using the Munkres algorithm when comparing tracks and minimum value at zero. Unlike the other metrics used in the comparison a smaller value of the RMSE indicates a higher accuracy in the localisation of particles. Furthermore, the RMSE is only calculated for a subset localisations generated by the tracking method, that is the TP (correct) detection as determined in the JSC metric. For the synthetic vesicles datasets, the method took all 12 of the number rankings (Figure 5.15a). On average, for all SNRs and all densities, the method showed an improvement of 0.2 pixels, equivalent to about 4%, with better improvements coming at lower-SNR levels although this may be due the lower amount of detections used in the calculation of the metric. In the synthetic microtubules data, the method achieved six of the possible 12 number one rankings with methods four and eight sharing the other six spots (Figure 5.15b). Here again the method appears to have greater localisation accuracy in lower-SNR data, but this is most likely due to few number of localisations with which to compare. On average when the method does not achieve the number one ranking it is around 0.3 pixels away from the best possible result, around 6%, however even for these cases the result is well above the mean value achieved by the competing methods on that dataset. Examining next the synthetic receptors datasets the method achieved five of a possible 12 number one rankings with the remaining number one rankings being shared between methods 1, 11 and 12 (Figure 5.15c). For the datasets where a number one ranking was not achieved the method was on average about 0.25 pixels away from the best achieved result, around 5%. Nevertheless, on these datasets the achieved localisation accuracy by the method was about equal to the mean result achieved by the competing methods. Finally, for the 3D viruses' synthetic datasets the method achieved 11 out of 12 possible number one rankings (Figure 5.15d). For the dataset where the number one ranking was not achieved the method was ranked second, missing the number one ranking by 0.2 pixels, the equivalent of 4%, and achieved a localisation accuracy 0.6 pixels better than the mean achieved by the methods competing on that dataset.

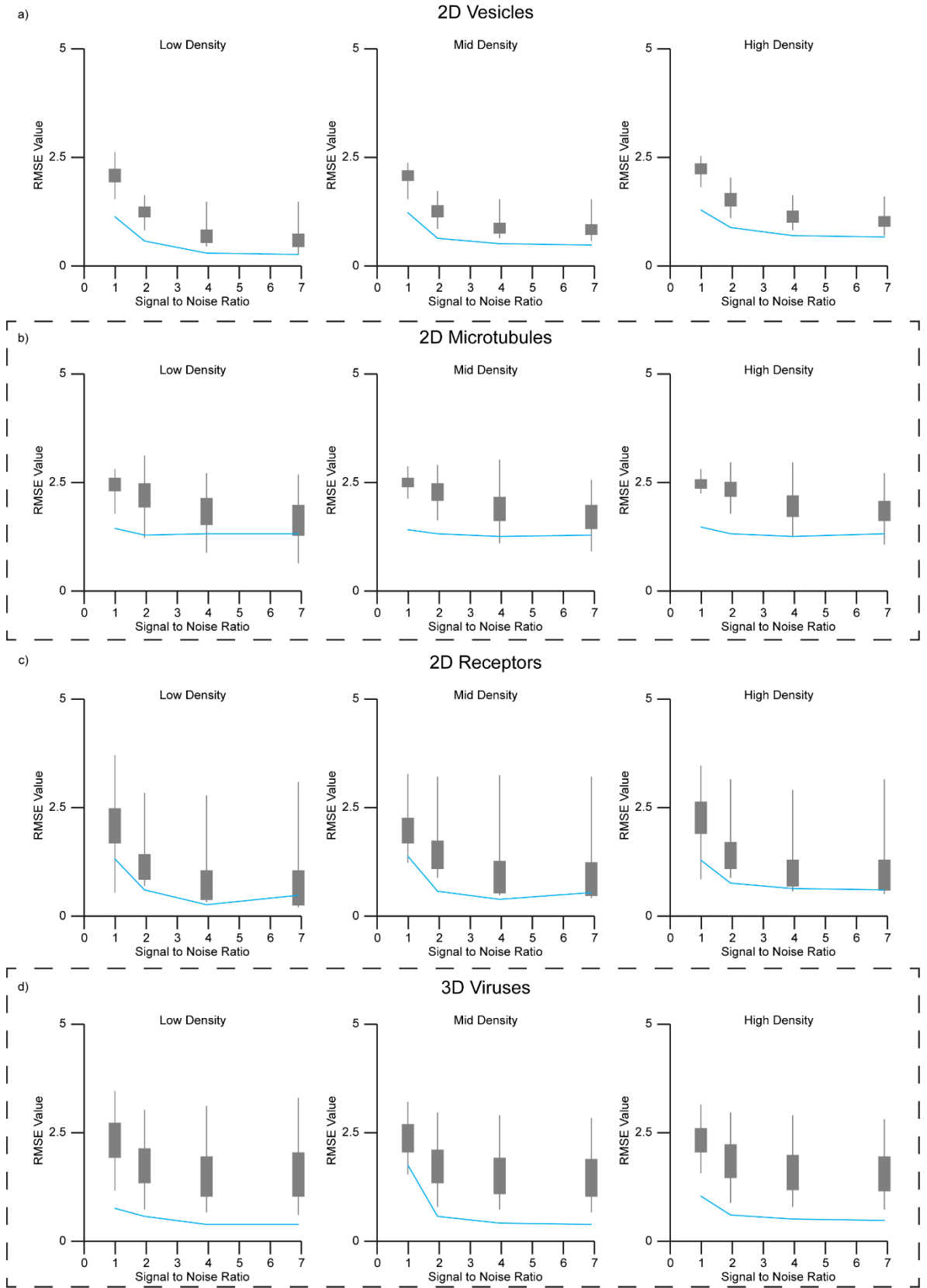


Figure 5.15: Performance of the tracking method measured using the RMSE metric on a) 2D vesicles, b) 2D microtubules, c) 2D receptors and d) 3D viruses synthetic image datasets. In all panels the density of the particles move from low to high

as you move left to right. In each graph the SNR increases as to move left to right along the x-axis. Here the method performed well for all datasets. Of particular note are both the vesicles and 3D viruses datasets where the method was the best performer of all competing methods on all datasets.

As seen from the results presented for each the metrics used to quantify the performance of all the tracking methods, it is clear that no one method stands out as the overall best performer (Figure 5.11-15). In fact, depending on the dataset under investigation and the metric used to quantify the performance of the tracking methods the top performer varies greatly. As before in Chapter 3, conclusions are drawn as to which method is the best overall performer by examining the methods that achieved the top three values for each metric on each given dataset (Table 5.01). Within the table the numbers 1 to 14 represent the original 14 competing tracking methods that took part in the ISBI particle tracking challenge [70], with the numbers assigned to each method being the same. Our new particle tracking method presented in this Chapter has been added as a 15th method and is represented with the letter “X”. For ease of reading the table all methods have also been assigned an arbitrary colour, with the method described here, X, being given the colour green. The multicolour nature of the table reiterates that no one tracking method dominates the variety of synthetic datasets investigated.

| Scenario | Density | 2D Vesicles | | | | | | | | | | | | 2D Microtubule | | | | | | | | | | | | 2D Receptors | | | | | | | | | | | | 3D Viruses | | | | | | | | | | | | | | | |
|----------|---------|-------------|----|----|----|-----|---|----|----|------|---|---|----|----------------|----|----|---|-----|----|----|---|------|----|----|----|--------------|----|----|----|-----|----|----|----|------|----|----|----|------------|---|---|---|-----|---|---|---|------|---|---|---|---|---|---|---|
| | | Low | | | | Mid | | | | High | | | | Low | | | | Mid | | | | High | | | | Low | | | | Mid | | | | High | | | | Low | | | | Mid | | | | High | | | | | | | |
| | | SNR | 2 | 4 | 7 | 1 | 2 | 4 | 7 | 2 | 4 | 7 | 1 | 2 | 4 | 7 | 2 | 4 | 7 | 1 | 2 | 4 | 7 | 2 | 4 | 7 | 1 | 2 | 4 | 7 | 2 | 4 | 7 | 1 | 2 | 4 | 7 | 2 | 4 | 7 | 1 | 2 | 4 | 7 | | | | | | | | | |
| α | #1 | 5 | 2 | X | X | 2 | X | X | X | 2 | 8 | X | X | 11 | 5 | 4 | 4 | 2 | 2 | 4 | 4 | 2 | 2 | 4 | 4 | 11 | 11 | 11 | 11 | 11 | X | X | X | X | 11 | 3 | X | 5 | 5 | X | X | 1 | X | X | X | 1 | X | X | X | | | | |
| | #2 | 2 | 5 | 5 | 1 | 5 | 8 | 1 | 1 | 5 | X | 1 | 1 | 13 | 4 | 8 | 5 | 11 | 4 | 2 | 2 | 11 | X | 2 | 2 | X | 5 | 1 | X | 13 | 8 | 3 | 3 | 11 | 2 | 11 | 3 | 13 | 2 | 1 | 1 | 5 | 2 | 5 | 2 | X | 2 | 2 | 2 | | | | |
| | #3 | 11 | X | 11 | 8 | 11 | 2 | 8 | 8 | X | 2 | 3 | 5 | 2 | 2 | 2 | 5 | 2 | 8 | 11 | 5 | 5 | 8 | 11 | 11 | 5 | 14 | 2 | 3 | 1 | 1 | 11 | 11 | 11 | 13 | 5 | 1 | 11 | 8 | X | 5 | 5 | 2 | 5 | 2 | 1 | 5 | 5 | 5 | | | | |
| β | #1 | 5 | 2 | X | X | 5 | X | X | X | 5 | X | X | X | 13 | 5 | 4 | 4 | 11 | 4 | 4 | 4 | 11 | X | 4 | 4 | X | 11 | 11 | X | 11 | X | X | X | 11 | 3 | 3 | 5 | 5 | X | X | 5 | X | X | X | 5 | X | X | X | | | | | |
| | #2 | 2 | 5 | 5 | 1 | 2 | 8 | 8 | 8 | X | 8 | 1 | 1 | 9 | 4 | 5 | 5 | 8 | X | 5 | 2 | 8 | 11 | 11 | 2 | 13 | 2 | 1 | 11 | 13 | 2 | 3 | 3 | 11 | 2 | 11 | X | 8 | 2 | 1 | 1 | 1 | 5 | 5 | 2 | X | 5 | 2 | 2 | | | | |
| | #3 | 13 | 9 | 3 | 5 | 13 | 3 | 1 | 1 | 13 | 5 | 3 | 8 | 2 | 11 | 8 | 2 | 13 | 11 | X | 5 | 1 | 4 | X | 11 | 11 | 8 | 3 | 1 | 1 | 11 | 11 | 11 | 13 | 5 | 1 | 11 | 1 | X | 5 | 5 | 8 | 2 | 2 | 1 | 1 | 2 | 5 | 5 | | | | |
| JSC | #1 | 5 | 2 | X | 7 | 5 | X | X | X | 5 | X | X | X | 13 | 5 | X | 2 | 11 | 11 | 4 | 2 | 11 | X | 4 | 2 | 13 | 11 | 3 | X | 11 | X | X | X | 11 | 3 | X | 5 | 5 | 1 | 1 | 5 | 5 | X | X | 5 | X | X | X | | | | | |
| | #2 | 2 | 5 | 5 | X | 2 | 8 | 7 | 7 | X | 5 | 7 | 7 | 9 | 11 | 5 | 4 | 13 | X | X | 4 | 13 | 11 | X | 4 | 13 | 11 | X | 4 | X | 2 | 11 | 3 | 13 | 2 | 3 | 3 | 11 | 2 | X | 3 | 8 | 2 | 5 | 5 | 1 | 2 | 5 | 1 | X | 2 | 2 | 2 |
| | #3 | 13 | 13 | 7 | 3 | 13 | 3 | 3 | 3 | 13 | 8 | 3 | 1 | 2 | 13 | 11 | X | 8 | 4 | 11 | X | 8 | 1 | 11 | 11 | 11 | 3 | 1 | 11 | 5 | 11 | 11 | 11 | 13 | 5 | 11 | 11 | 13 | 9 | 2 | X | 8 | X | 2 | 2 | 1 | 5 | 5 | 5 | | | | |
| JSCt | #1 | 13 | 13 | X | 7 | X | X | X | 7 | X | X | X | X | 13 | X | X | 2 | 13 | X | X | X | 1 | X | X | X | 13 | 2 | 3 | X | 13 | X | X | X | X | X | X | 5 | X | 5 | X | 5 | X | X | X | X | X | X | X | X | | | | |
| | #2 | X | 2 | 7 | 12 | 13 | 8 | 7 | X | 13 | 5 | 7 | 7 | 6 | 9 | 5 | X | 11 | 11 | 4 | 2 | 11 | 11 | 4 | 2 | X | 13 | 1 | 3 | 1 | 2 | 3 | 3 | 13 | 11 | 3 | 3 | 8 | 2 | 1 | 1 | 13 | 5 | 5 | 1 | 5 | 5 | 2 | 2 | | | | |
| | #3 | 2 | X | 5 | 3 | 5 | 3 | 3 | 3 | 5 | 8 | 3 | 5 | 2 | 13 | 11 | 4 | 8 | 5 | 5 | 4 | 8 | 1 | 11 | 4 | 5 | 9 | 11 | 5 | 11 | 5 | 11 | 11 | 1 | 5 | 11 | 11 | 1 | 5 | 2 | 5 | 1 | 2 | 2 | 5 | 13 | 2 | 5 | 5 | | | | |
| RMSE | #1 | X | X | X | X | X | X | X | X | X | X | X | X | X | X | X | X | X | 8 | 8 | 8 | X | X | 4 | 4 | X | X | X | 12 | X | X | 1 | 12 | X | X | 11 | 12 | X | 1 | 1 | X | X | X | 1 | X | X | X | X | X | | | | |
| | #2 | 12 | 1 | 8 | 1 | 1 | 1 | 1 | 1 | 1 | 1 | 1 | 1 | 12 | 1 | 1 | 1 | 4 | 4 | 4 | X | 8 | 5 | 4 | 4 | X | 1 | 1 | 6 | X | 1 | 1 | 12 | X | 1 | 1 | 12 | X | 1 | 1 | 1 | 2 | 2 | X | 1 | 2 | 2 | 1 | 1 | 2 | 2 | | |
| | #3 | 1 | 12 | 10 | 5 | 12 | 8 | 10 | 12 | 1 | 8 | 8 | 12 | 5 | 4 | 5 | 5 | 1 | 5 | 8 | 5 | 4 | 5 | 8 | 9 | 1 | 12 | 11 | 1 | 1 | 12 | 11 | 6 | 8 | 11 | 11 | 12 | 5 | 2 | 5 | 5 | 5 | 2 | 5 | 5 | 5 | 5 | 5 | 5 | | | | |

Table 5.01: Top 3 ranking methods for all of the synthetic datasets examined in the ISBI particle tracking challenge. Methods 1-14 are the same as described in the original particle challenge [70] with the tracking method described here represented in the table with an “X”. No one method appears to dominate the table with different methods appearing in the top 3 for each modelled scenario. However the method described here does appear to be a regular top performer across all datasets.

Further to table 5.01, the frequency that each competing tracking method appears within the table is examined, this was the technique used to draw a final ranking in the original challenge paper [70] (Table 5.02a). In addition to this the frequency each method appears within the top 3 for each imaging scenario was investigated, allowing for a conclusion to be drawn as to which tracking method is best suited to each imaging scenario (Table 5.02b-e).

Analysing the overall rankings (Table 5.02a) the method achieved the most top 3 appearances over all the datasets investigated achieving 170 out of a possible maximum of 240 top 3 placings, over 50 more than the second placed method. Looking at the number of top 3 appearances for individual imaging scenarios starting with the 2D synthetic vesicles datasets the method achieved 51 out of a possible 60 top 3 appearances, an impressive result, and more than double the method in second place which achieved 25 top 3 appearances (Table 5.02b). Next examining the 2D synthetic microtubules datasets, as expected method 4, a specialised microtubule tracking method, achieved the highest number of top 3 rankings with 39 out of 60 (Table 5.02c). Our method achieved the second most top 3 rankings on this microtubules data with 30 out of a possible 60, a pleasing result especially as the method never seemed to overachieve on any of the given performance metrics. Next the 2D synthetic receptors datasets in which method 11 achieved the most top 3 rankings with 50 out of a possible 60 appearances, the method achieving 40 appearances (Table 5.02d). Overall this is a good result for the method, it is clear from the results that the method struggled with the low-density synthetic receptors datasets. Finally, examining the 3D synthetic viruses' datasets in which not so many of the methods competed, in fact 8 of the competing failed to achieve any top 3 rankings (Table 5.02e). In these 3D viruses' datasets method 5 achieved the most top 3 rankings with 55 out of a possible 60. Our tracking method was a close second achieving 49 out of a possible 60 top 3 rankings. However, although the method was ranked second in this way the method achieved an overall 41 number one rankings compared to method 5's 13 number one rankings on the 3D synthetic viruses' datasets.

| a) Overall | | | b) 2D Vesicles | | | c) 2D Microtubules | | | d) 2D Receptors | | | e) 3D Viruses | | |
|------------|--------|------|----------------|--------|------|--------------------|--------|------|-----------------|--------|------|---------------|--------|------|
| Rank | Method | Freq | Rank | Method | Freq | Rank | Method | Freq | Rank | Method | Freq | Rank | Method | Freq |
| 1 | X | 170 | 1 | X | 51 | 1 | 4 | 39 | 1 | 11 | 50 | 1 | 5 | 55 |
| 2 | 5 | 112 | 2 | 5 | 25 | 2 | X | 30 | 2 | X | 40 | 2 | X | 49 |
| 3 | 2 | 85 | 3 | 1 | 22 | 3 | 11 | 28 | 3 | 3 | 23 | 3 | 2 | 38 |
| 4 | 11 | 81 | 4 | 8 | 18 | 4 | 5 | 23 | 4 | 1 | 22 | 4 | 1 | 27 |
| 5 | 1 | 76 | 5 | 2 | 14 | 4 | 2 | 23 | 5 | 13 | 12 | 5 | 8 | 6 |
| 6 | 8 | 42 | 5 | 3 | 14 | 6 | 8 | 16 | 6 | 2 | 10 | 6 | 13 | 4 |
| 7 | 4 | 39 | 7 | 7 | 12 | 7 | 13 | 10 | 7 | 5 | 9 | 7 | 9 | 1 |
| 8 | 3 | 37 | 8 | 13 | 11 | 8 | 1 | 5 | 8 | 12 | 7 | 8 | 11 | 0 |
| 8 | 13 | 37 | 9 | 12 | 7 | 9 | 9 | 4 | 9 | 8 | 2 | 8 | 4 | 0 |
| 10 | 12 | 15 | 10 | 11 | 3 | 10 | 12 | 1 | 9 | 9 | 2 | 8 | 3 | 0 |
| 11 | 7 | 12 | 11 | 10 | 2 | 10 | 6 | 1 | 9 | 6 | 2 | 8 | 12 | 0 |
| 12 | 9 | 8 | 12 | 9 | 1 | 12 | 3 | 0 | 12 | 14 | 1 | 8 | 7 | 0 |
| 13 | 6 | 3 | 13 | 4 | 0 | 12 | 7 | 0 | 13 | 4 | 0 | 8 | 6 | 0 |
| 14 | 10 | 2 | 13 | 6 | 0 | 12 | 14 | 0 | 13 | 7 | 0 | 8 | 14 | 0 |
| 15 | 14 | 1 | 13 | 14 | 0 | 12 | 10 | 0 | 13 | 10 | 0 | 8 | 10 | 0 |

Table 5.02: Final rankings dependant on the number of appearances within table 5.01. a) the overall ranking, b) the ranking for the 2D vesicles synthetic datasets, c) the ranking for the 2D microtubules synthetic datasets, d) the ranking for the 2D receptors synthetic datasets and e) the ranking for the 3D viruses' synthetic datasets. The method described here is the best overall performer achieving over 50 more top 3 rankings than the second place method showing its versatility for all types of image data. Looking at each scenario independently, the method was again the top performer for the vesicles scenario, second in the microtubule scenario where it was beaten by a specialist method that did not compete on any other scenarios. Again, the method was second on the receptors scenario beaten by method 11 although many of these appearances are at rank #3. Finally, the method was second on the 3D viruses datasets beaten by the best performing method from the original ISBI challenge.

5.4 Summary

This Chapter has presented a tracking method capable of tracking single particles in both 2D and 3D image space. Particle detection is achieved through signal enhancement using a new and novel Haar-inspired feature from which segmentation can be achieved using a global threshold. The threshold can be defined using one of three philosophies dependant on the requirements of the data under investigation. Two methods of clumping/splitting for conjoined particles are explored, finding that the size of the particles under investigation is key in deciding which of the two methods to use. Finally, the localisation of the particles has been improved, especially with particles that have an asymmetric intensity profile, by implementing 2D Gaussian fitting for 2D image data. For the 3D image data, weighted centre-of-mass is implemented. Trajectory linking in the method is achieved using a global nearest neighbour methodology into which many features describing the particle morphology and intensity profile have been incorporated. Furthermore, motion models

have also been incorporated describing both Brownian and linear motion behaviour, as well as allowing fast switching between the two models.

The method is fully validated using all available synthetic image datasets from the ISBI particle tracking challenge thus allowing for a comparison with the 14 other state-of-the-art tracking methods presented in [70]. Our proposed method performs as the best method when ranked using the number of top 3 results achieved compared to the other methods competing in the challenge. Although the method was not the best method for all synthetic imaging scenarios when inspecting them individually. However, the high ranking achieved even in certain specialised applications shows the utility of the method, and that in general it will provide accurate results regardless of the imaging scenario being investigated.

Finally, although true 3D time-lapse biological image data is very difficult to currently collect the tools to analyse such data when the technologies become more readily available will be essential.

Chapter 6 Super-Resolution

The standard diffraction limit which limits resolution in optical microscopy is around 200nm, for visible light. Techniques used to circumvent the diffraction limit are referred to commonly as SR in light microscopy. This Chapter focuses on work contributed to evaluating and validating a new SR method called TRAM and is adapted from [1]. To achieve SR in microscopy three main approaches have emerged. Firstly, hardware SR approaches aim to either engineering a specific PSF, as in STED, or employ optical patterning of excitation illumination and measure the nonlinear response from the sample, as in SIM. Secondly, SMLM approaches such as PALM and dSTORM, aim to separate PSFs temporally allowing the localisation of each molecule generating a PSF to be calculated with a precision much higher than the diffraction limit. A SR image is then reconstructed using all locational information from different time points. Finally, computational SR approaches assume that any acquired diffraction limited image is the result of an original high resolution image being degraded by noise and blur. It is therefore the aim of computational SR to restore the original high resolution image from a set of diffraction limited images using various image processing techniques. It is within this category, computational SR, that the TRAM method resides. TRAM works by restoring a SR image, using information theory and image processing techniques, from multiple diffraction-limited resolution observations, these observations can be obtained using any conventional microscope whilst translating the sample in the image plane. TRAM has the added advantage as these translational steps do not need to be exact and allow for smaller regions of interest to be scanned with more detail (Figure 6.1).

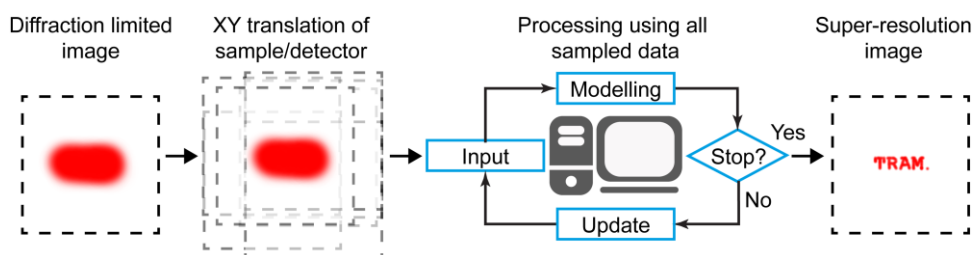


Figure 6.1: Translation microscopy delivers super-resolution image data in a simple, inexpensive way. a) Schematic illustration of translation microscopy (TRAM). TRAM involves acquiring multiple images of the same sample, as the object

is moved on the microscope stage. All the acquired data are then used to rationally denoise and restore a super-resolution image through an iterative energy minimization process.

The contributions to the TRAM method included in this thesis consists of analysing the validation process to find results that concur with a novel GT. Secondly, the analysis of the results generated by applying the TRAM method to a readily available, off the shelf, biological sample is presented.

6.2 Analysis to Validate TRAM

In SR, suitable GT data used in the evaluation and validation of a method is often difficult to obtain. In general, synthetically generated GT image data is used for initial comparison of performance of these methods, however these synthetic images often lack the complexity present in real image data. The demand for more complex GT image data has given rise to the generation of GTs based on organic samples. As such to evaluate the TRAM method a GT of specifically designed and synthesised novel QD-DO structures of constant and predictable dimensions was utilised. The reliability of these structures was confirmed by imaging them using AFM to confirm that they did indeed have the same dimensions of the structure that were designed. QDs were chosen as the fluorescent emitters due to their predictable size and photo-stability, this is in comparison to organic dyes which are prone to photobleaching and hence cannot be used reliably with TRAM due to the extended exposure times required. The QD-DO structures were designed to have the dimensions of 47×53 nm on a DNA origami scaffold of 70×100 nm, as depicted in Figure 6.2a. Although the QD-DO structures were designed to have a 16 nm diameter QDs in each corner of the DNA origami scaffold, occupation of every conjugation site was difficult to achieve whilst trying to simultaneously avoid over-saturation of the sample and contamination by non-conjugated QDs. Nevertheless, this approach delivered samples with sub-resolution structures that could be used as GT for the SR method. Although the samples were heterogeneous, typically each scaffold had 3 or 4 QDs conjugated to it each of which was separated by a measurable and predictable distance which was confirmed using AFM (Figure 6.2b, inset). TRAM was applied to the QD-DO samples, 45 diffraction limited images

were collected whilst translating the sample with steps of around 100 nm in a 2D grid-pattern on a CLSM. Figure 6.2c gives an exemplar single diffraction-limited image acquired using the CLSM with no visible sub-diffraction structures in the image or in the zoomed region of interest (Figure 6.2d). As acquiring many images whilst translating the sample is essentially oversampling a simple sum of these 45 (translation-corrected) images was used to see if they reveal any useful contrast (Figure 6.2e and 6.2f) but still no structures were visible, however, these images still provide essential information for TRAM restoration process. A TRAM restored image showing the same region as in Figure 6.2c and 6.2e is shown in Figure 6.2g with Figure 6.2h showing a TRAM restored and rendered image of the same region shown in Figure 6.2d and 6.2f. Within the TRAM image sub-diffraction rectangular structures become more apparent confirming what was imaged using AFM in Figure 6.2b.

To quantify the results of the TRAM reconstruction whilst accounting for the heterogeneity in sample preparation, the distribution of the lengths between the QDs on the DNA-origami scaffold in both the GT samples, imaged using AFM, and the reconstructed TRAM images were examined. Here two edges (x and y) and the hypotenuse can be measured. Due to the overlapping nature of the structures in both the AFM and TRAM restored images the measurements of the edges and hypotenuse was undertaken in a semi-automatic nature. Firstly, around 40 viable structures to be used in the measurements were manually identified from a large sample containing over 100 such structures. Due to incomplete conjugation of some DNA-origami sites the structures contained within the sample used for the measurements contained both 3 and 4 QDs conjugated to the origami scaffold. Secondly, the measurements between each individual QD-DO structure was undertaken using a simplified version of the automatic particle detection described in Chapter 5. Finally, the distance measurements between the QDs were manually classified into being either of the x (short) length of a triangle or square, y (long) length of a triangle or square or, finally, belonging to the hypotenuse of the triangle or square. The distribution of these values is assumed to belong to a normal distribution with the mean value for the distribution of each of the lengths was found to be 46, 53 and 71nm for the x, y and hypotenuses lengths respectively in the AFM images (Figure 6.2i). Overlapping of the three histograms describing

the three measured lengths and the high variance of each of the distributions is the manifestation of the imperfections in the structures as previously discussed (Figure 6.2b). Next taking the same measurements for the TRAM restored images, the mean values for the length distributions were 50, 58 and 76 nm for the x, y and hypotenuses lengths respectively (Figure 6.2j). These measurements describe rectangular structures of the same aspect ratio as in the AFM images, but slightly larger albeit by only a small fraction of the TRAM pixel size of 19 nm. Investigating this result further, the three representative exemplar structures that were observed in TRAM images are given with their pixel grids (Figure 6.2j), this helps to explain the distribution of the x, y and hypotenuse histograms. In the three examples the “x” length mainly resides between 42 and 54 nm, which correspond to the diagonal lines of 1×2 and 2×2 pixels, respectively. The correlation between the AFM and TRAM results is encouraging especially given the inhomogeneity of the samples and the differences in the two imaging modalities. The TRAM restoration process was able to deliver, from image data that was acquired using very common laboratory equipment in the form of a CLSM, a distinct improvement in the spatial resolution of the image as well as a clear improvement in image contrast. The TRAM restoration process revealed the sub-resolution rectangular structures from images where they were not visible. Through simple measurements the structures were confirmed to indeed have the same shape and aspect ratio of the structures that were designed.

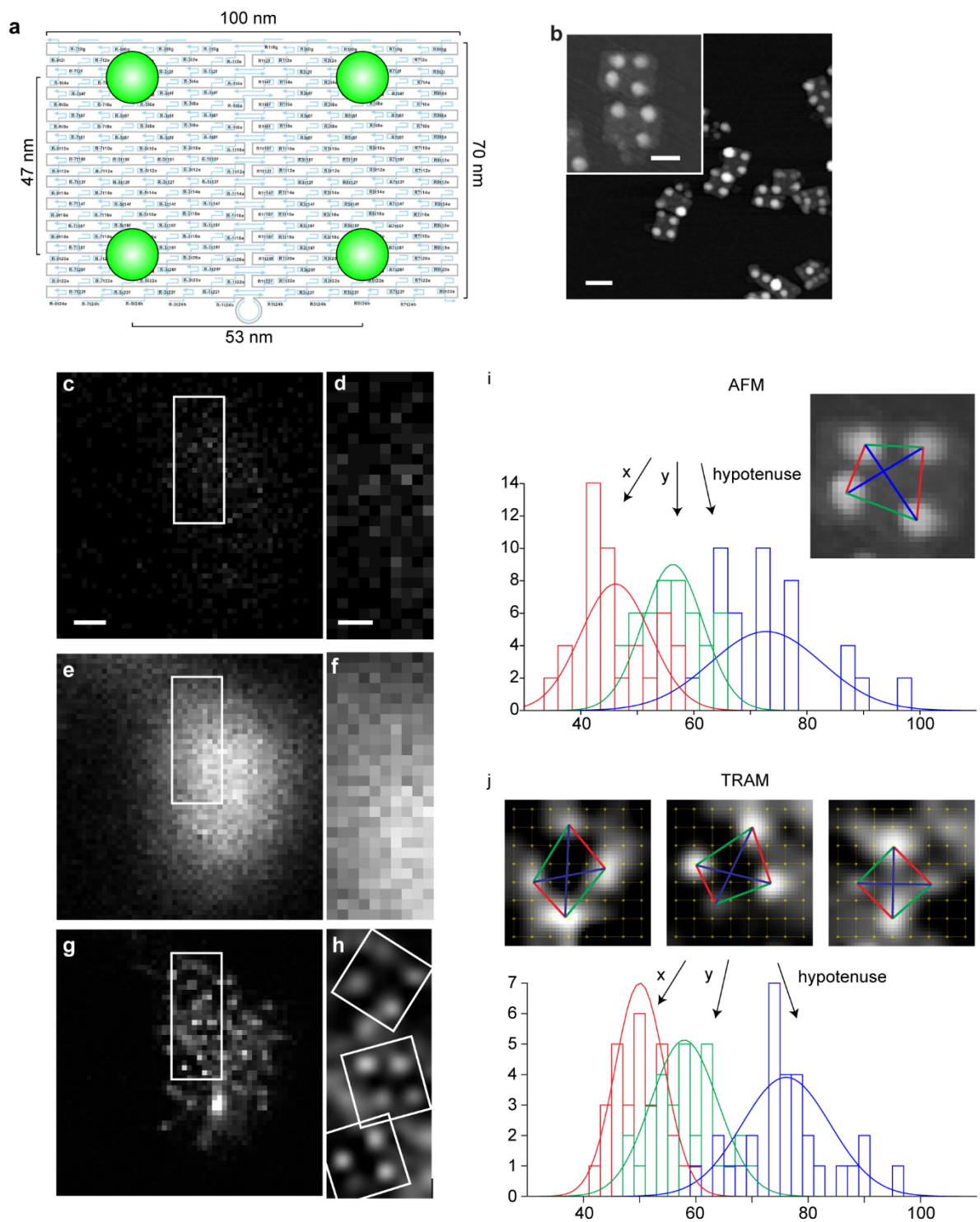


Figure 6.3: 'GT' samples demonstrate the high-fidelity of TRAM. a) Schematic of the rectangular QD structure on a DNA origami template. b) AFM image of the structure (scale bar 100 nm), inset shows a zoom area (scale bar 50 nm), confirming that the design is reiterated in the nano-structure. c) A single diffraction-limited image, from the set of 45 translation images acquired using CLSM. Scale bar 100 nm. d) A zoom region of interest from c). Scale bar 50 nm. e) Sum of all data from 45 aligned translation images, showing no structures in the over sampled data. f) A zoom region of interest from e). g) TRAM SR reveals rectangular structures in restored image. h) A rendered, zoom region of interest from g). i) Measurement of the edges and hypotenuse of the rectangular structures from the AFM: (x) 46 nm, (y) 53 nm and (hypotenuse) 71 nm. j) Similar measurements for the TRAM restored image: 50 nm, 58 nm and 76 nm, where three representative structures are also shown in the pixel grid of 19 nm.

6.3 Analysis of Application of TRAM

Having demonstrated through the validation process that TRAM could restore a SR image in a straightforward manner without the need for special instrumentation it was next applied to a biological sample to show its versatility. A common requirement in biological applications is to look at many structures simultaneously, these structures will typically be labelled with different fluorophores each having their own excitation and emission characteristics and will be combined into a single (false coloured) multi-coloured image. However, finding multiple fluorophores that are compatible with a single SR method remains difficult, for example, STED commonly utilises a single depletion laser, meaning that only special combinations of organic dyes will allow for multi-colour imaging using this method. Dual colour PALM experiments remain difficult until better versions photo-activatable green fluorescent proteins are created. Multi-colour dSTORM is reliant on highly technical sample preparation. In principle, the TRAM method described here is naturally multi-colour and requires no special sample preparation. As such to test the method an “off-the-shelf” commercially available three colour sample was selected to test its versatility. The sample selected was a bovine pulmonary artery endothelial cell sample; this sample had its tubulin network firstly immunofluorescently labelled with primary anti-bovine α -tubulin mouse monoclonal antibodies and was then secondarily labelled with goat anti-mouse Fab fragments conjugated to BODIPY FL, the sample also has DNA present within the nucleus stained by DAPI and its cytoskeletal actin network stained by Texas Red phalloidin. This sample provides as good test for multi-colour TRAM as these dyes are not commonly known to be particularly photo-stable or to have any special properties. A set of 60 diffraction-limited images of all three labels were acquired in approximately 30 seconds using a CLSM, translation of the sample was again achieved using an XY-grid-pattern with the spacing between images being around 100nm. A single diffraction-limited image and the corresponding TRAM restored image are given in Figure 6.3a and 6.3b, respectively. The TRAM restoration process reveals a clear and apparent improvement in the image resolution. A region corresponding to the centrosome is shown as a zoomed section in Figure 6.3c, this highlights the close proximity of the actin (red) and tubulin (green)

networks within this region. This apparent improvement in resolution was validated within the multi-colour TRAM image by measuring the FWHM of cross sections for multiple samples in both the actin and tubulin networks. The FWHM is commonly used as an estimator for image resolution. Figure 6.3d (top row) shows a zoomed segment of part of the tubulin network from which 4 measurements were taken. Firstly, two lines of only a single pixel width at slightly different locations and secondly two “line” measurements averaged over a sliding window of width 25 pixels. As seen intensity fluctuations can considerably affect the shape and width of the measurements taken with only a single pixel width however, when these measurements are averaged over a window of width 25 pixels they are almost unchanged. Therefore, 60 typical straight tubulin sections, from various locations throughout the entire image, were measured using the window of width 25 pixels. The histogram of the FWHM of these measurements is given in the bottom row of Figure 6.3d, a distinct peak can be seen in the histogram and occurs when the value of the FWHM is around 55 nm. This result has good correlation with the 50-60 nm range observed by Gustafsson, Sedat and co-workers when measuring the width of microtubules in their 3D SIM experiment [11]. Furthermore, comparable measurements were undertaken using window widths of 25 pixels on the actin network, here it was found that the FWHM cross sectional measurement to be on average around 80nm. Shown is a zoom view of tubulin network and nuclei (stained with DAPI) for both CLSM and TRAM images, Figure 6.3e and 6.3f respectively, the corresponding signal intensity profile for a 25 pixels’ width line for the TRAM restored image is given Figure 6.3g. As seen the tubulin network again has a FWHM of around 55 nm, confirming the earlier measurements, while the FWHM of the DAPI-stained nuclei is measured to be around 180 nm. While this DAPI measurement is larger than that measured by Sedat and co-workers in the aforementioned 3D SIM experiment it probably shows the current limitations of TRAM to resolve blob-like structures, less well than filament type structures, as well as SIM. Although, this should not take away from the TRAM methods overall versatility when compared to other SR methods.

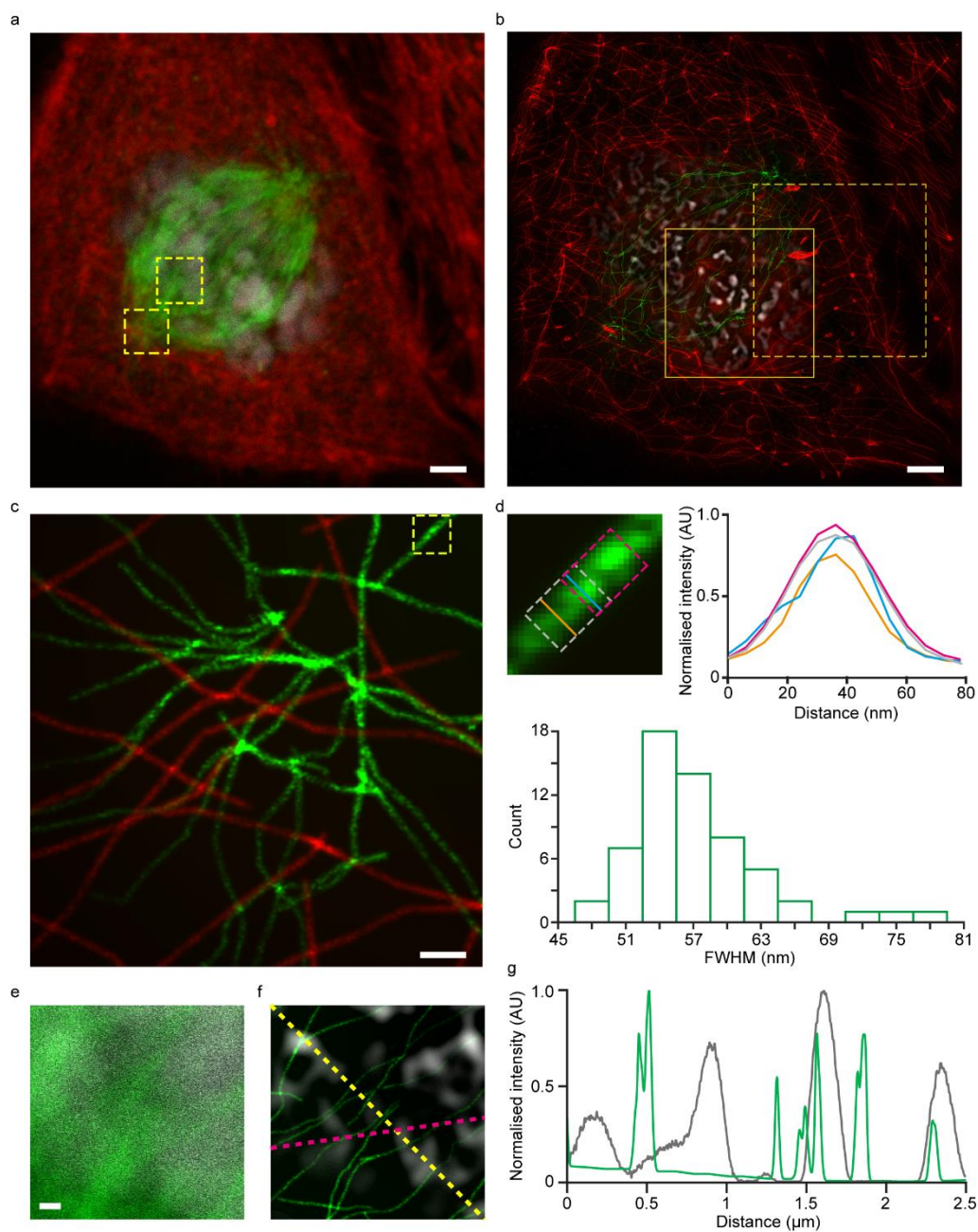


Figure 6.3: Multi-colour TRAM performed on a pulmonary endothelial cell. (a) One of the 60 LR images acquired whilst translating the sample in XY-steps of around 100 nm. Three colours represent three different stained structures; red: actin, green: tubulin and gray: DNA (DAPI), respectively. Scale bar 2 μm . (b) TRAM-restored image using the 60 diffraction-limited images. (c) A zoom-view of the spindle-pole region (bottom-left box in (a)) showing TRAM restored data for both colour channels. Scale bar 250 nm. (d) Top row: A zoom-view of a segment of the tubulin network from the box in (c) and corresponding intensity profiles of the cross-section measurements at single pixel and within a window of 25 pixels respectively. Bottom row: Histogram of the FWHM measurements of 60 cross-sections taken from the tubulin network, exhibiting a distinct peak at around 55 nm. (e) A zoom-view of the tubulin network (green) and DAPI stained nuclei (gray) from the top-right region-of-interest in (a). Scale bar 250 nm. (f) Corresponding TRAM restored region in which DAPI-stained structures are clearly resolved. (g) Intensity profiles of the tubulin network (yellow line) and DAPI (pink line) from the TRAM restored image.

6.4 Summary

As with all other SR microscopy techniques TRAM has its limitations. The method relies upon intensity based pixel information, so if photo-bleaching occurs within a sub-region of any image the restoration process is affected within that sub-region. TRAM is currently limited to the restoration of fixed samples (in common with many other SR imaging modalities), if there are changes to the structures within a sample between the translation images due to dynamics (or motion induced blur), TRAM in its current form cannot accurately restore these structures. Currently, TRAM restoration is not computationally efficient and requires a few hours to restore an image of 256×256 pixels using a high-end desktop computer running MATLAB, however, its performance will improve with the optimisation of the algorithm, implementation of parallel processing and with advances in computer hardware. Finally, even though TRAM is dependent on its operating conditions, as with other SR microscopy techniques, it is less reliant on the sample preparation techniques required.

In summary, TRAM is a SR imaging technique, which can be implemented without any modification to the microscope or other hardware. TRAM was developed for the sole purpose of restoring images that are of low-SNR and contain small structures, typically many times below the diffraction limit. The use of multiple translation images in TRAM has enabled the use of more effective collaborative filtering in the image denoising process with the newly developed prior model. The multiple translation approach also imposes a tighter criterion on the TRAM restoration process. Therefore, a restored TRAM image can be viewed as an optimal SR counterpart of the set of diffraction-limited translation images. Using this methodology TRAM is more robust than present SR methods when applied to fluorescence biological imaging. Furthermore, TRAM is naturally multi-colour in its design, requires no special preparation of sample, is able to work with any fluorescent stain and simple to apply. As such the TRAM technique, could be of broad interest for various applications in the cell-biology community.

Chapter 7 Conclusions

7.1 Summary

This final Chapter summarises and concludes the work comprised in this thesis. As mentioned in the introduction the major aim of this thesis was to design single particle tracking methods that are capable of working in both 2D and 3D image space. These methods also need to be able to work in images with low-SNR and low-contrast, such as those found in live-cell biological environments. Finally, the methods should be able to tackle time-lapse image data with high particle density such that conclusions drawn from the trajectory analysis is reliable in having come from a high enough sample size.

The tracking method presented in Chapter 3 was designed to work with sub-diffraction particles that are airy in nature. The method was applied to the applicable “vesicles” and “receptors” synthetic image datasets generated for the ISBI single particle challenge. These datasets contain particles which have an airy profile but with different motion models; the synthetic vesicles were modelled to have Brownian motion whilst the synthetic receptors were modelled to have motion which switch between Brownian and directed motion. Even with these two different motion types the tracking method performed the best of the evaluated methods on these datasets scoring 73 out of a possible 120 top 3 rankings when ranked using the 5 performance metrics. Furthermore, this tracking method was again validated using experimentally collected data, although only two metrics were used to validation on this data due to the manually calculated GT. Here the method again performed amongst the best methods as well as showing a good consistency with results that would have expected from image data of the same quality that was generated synthetically. This finding validates that the results found on the synthetic image data can be transferred to real world applications with a reliable and repeatable accuracy.

In Chapter 4 the tracking method introduced in Chapter 3 was applied to two distinct biological datasets; tracking of munc18-1, a protein essential for regulated exocytosis, in

neurons and tracking of SNAP-25 in neuroendocrine cells. From the tracking of these datasets were able to observe the caged motion of the proteins further confirming the observations made in [77] about the organisation of these proteins at the cell membrane.

Chapter 5 introduced a newly developed second tracking method, unlike the method developed in Chapter 3 this method is capable of tracking in 3D image space as well as localising asymmetric particles in 2D space. As such, this method is validated on all of the synthetic datasets generated for the ISBI single particle challenge. In addition to the datasets used for validation in Chapter 3, validation was also undertaken on the synthetic “microtubules” datasets which model directed motion in 2D image space and finally, validation on the synthetic “viruses” datasets which model motion switching in 3D image space. Again, the method was shown to perform the best overall on these synthetically generated datasets scoring 170 top 3 rankings out of a possible 240.

Finally, Chapter 6 presents the techniques used to analyse the validation and application of a new computational SR method TRAM. For validation of the method a comparison with a novel GT of QDs on a DNA origami scaffold as used. As the structures were designed to have set distances between the QDs, which was verified through the use of AFM, it is possible to use these distances as a GT for the TRAM method. TRAM was performed on the same samples and the distance between the dots measured, which the distribution of distances in both the AFM and TRAM results having a very good consistency.

7.2 Further Work

Firstly, improvements can be made to the particle tracking method described in Chapter 5. Here the method appears to struggle with data of the lowest-SNR, to combat this image denoising could be implemented. However, as one of the main targets is for the tracking method to be efficient this could grossly effect the processing time required to form trajectories in a given dataset. Given that the overall performance using this tracking method on the synthetic microtubules datasets maybe a more specific signal enhancement

filter could be designed for data of this type. The most obvious being a Haar-inspired feature with the same asymmetric Gaussian distribution as the synthetic microtubule particles themselves. However, using this method rotation of the features would have to be introduced and, as discussed in Chapter 2, can lead to its own errors as well as increased processing times.

As a general note on the ISBI single particle challenge, with them having the ability to generate synthetic data it would have been pertinent to generate multiple training and challenge datasets for each scenario, density and SNR. This would avoid accidental (or intentional) over training by a tracking method on a training dataset before applying it to a challenge dataset. Also, the use of multiple challenge datasets would also avoid single anomalous results skewing the data in favour or against a certain tracking method on a certain dataset. It is also notable that using the same number of particles in 3D image space as 2D image space for the same density seems inconsistent, if a method was to use a slice by slice method for the identification of particles the density in each slice would be much lower than that in 2D image data of the same density.

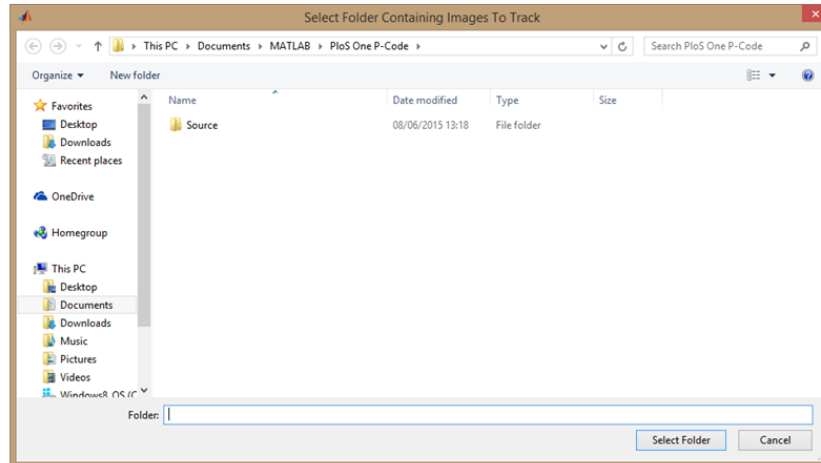
Appendix

Appendix A: Chapter 3 tracking method user guide

To start the program simply enter the following command into **command window** of Matlab

```
ParticleTracking();
```

1. Use the **browser** window to select the folder which contains the images you wish to track.



2. Define the filename specification of the image sequence that you wish to track. Image Filenames must take the of Prefix – Number – Format i.e. “IMG001.tif” or “Frame_0001.png”.

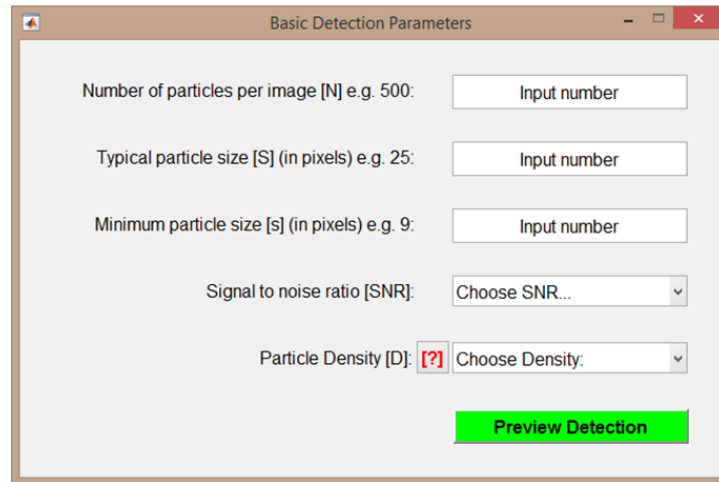
Input Image Sequence Filename

Input Images Need to have the Format: Prefix-Number-Format, i.e. "IMG001.tif"

| | |
|---|------|
| Filename Prefix: | IMG |
| File Format/Extension: | .tif |
| Number of The First Frame: | 1 |
| Number of The Last Frame: | 100 |
| Number of Digits for Enumeration i.e. 4 for 0001: | 3 |
| Number of Frames Per Cycle (for sptPALM): | 100 |

Click OK To Continue: **OK**

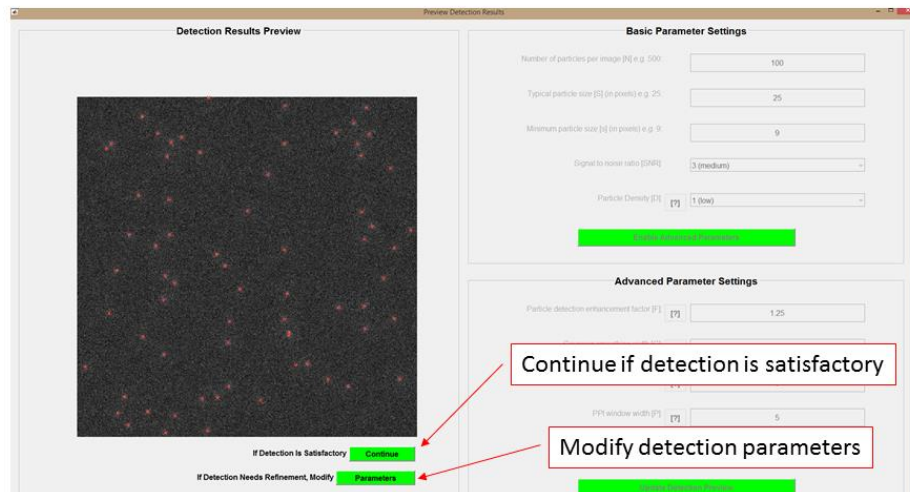
3. To begin particle detection we require a few **parameters**. i) An estimate of the number of particle per image. ii) The typical size of a particle within an image. iii) The minimum size of a particle within an image i.e. the smallest object that you are sure is a particle. iv) An assessment of the SNR of the image sequence i.e. low, medium or high. v) An assessment of the particle density within an image i.e. low, medium or high. These parameters can be refined at the next step.



A dialog box titled "Basic Detection Parameters" with a standard window control bar. It contains five input fields and a button:

- Number of particles per image [N] e.g. 500: Input number
- Typical particle size [S] (in pixels) e.g. 25: Input number
- Minimum particle size [s] (in pixels) e.g. 9: Input number
- Signal to noise ratio [SNR]: Choose SNR... (dropdown menu)
- Particle Density [D]: [?] Choose Density: (dropdown menu)
- Preview Detection (green button)

4. Preview of detection results. At this point you can either i) **continue** with the detection using the current parameters or ii) modify the **parameters** to obtain a better detection. Continuing will close this window, modifying parameters will activate more other panels.



A dialog box titled "Preview Detection Results" with a standard window control bar. It is divided into two main sections:

- Detection Results Preview:** A large black square image showing numerous small red dots representing detected particles.
- Basic Parameter Settings:** A panel on the right with input fields for:
 - Number of particles per image [N] e.g. 500: 100
 - Typical particle size [S] (in pixels) e.g. 25: 25
 - Minimum particle size [s] (in pixels) e.g. 9: 9
 - Signal to noise ratio [SNR]: 3 (medium)
 - Particle Density [D]: [?] 1 (low)

Below the Basic Parameter Settings is an **Advanced Parameter Settings** section with:

- Particle detection enhancement factor [F]: [?] 1.25
- FFT window width [W]: [?] 5

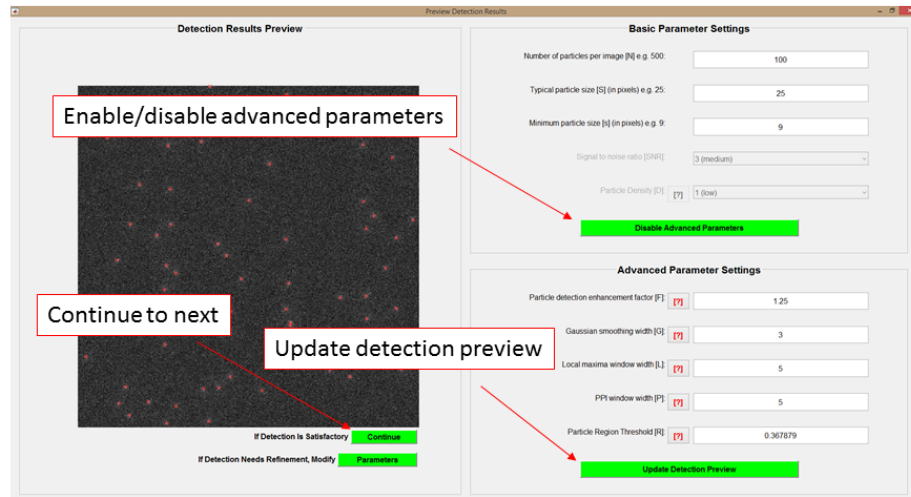
At the bottom, there are two green buttons:

- Continue**: Labeled "If Detection is Satisfactory".
- Parameters**: Labeled "If Detection Needs Refinement, Modify".

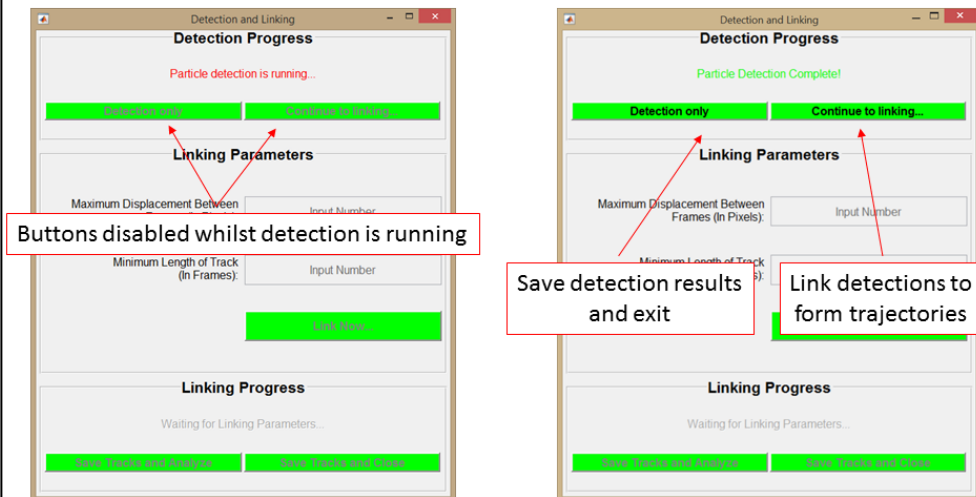
Red arrows point from text boxes to these buttons:

- "Continue if detection is satisfactory" points to the Continue button.
- "Modify detection parameters" points to the Parameters button.

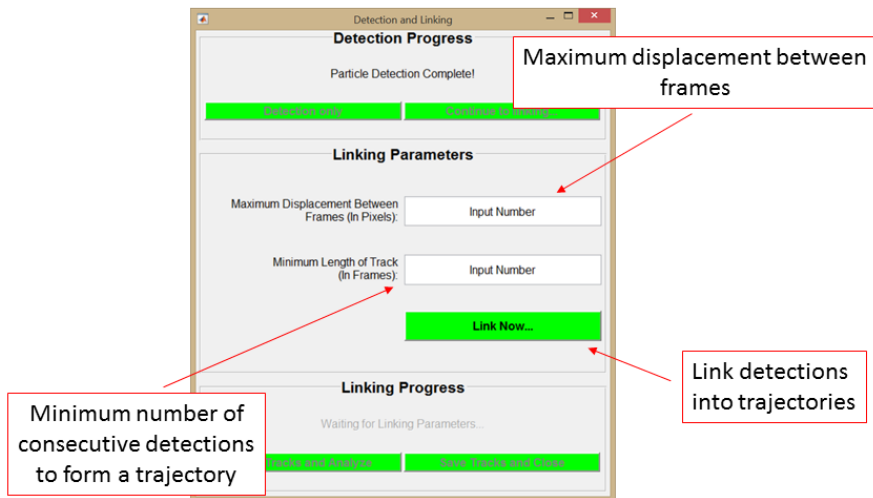
5. Initially only the “Basic parameters” are active, here you can modify the parameters we input earlier and use the “Update Detection Preview” button to see the effect. Enabling advanced parameters allows you modify some of the detection algorithms more complex parameters. Click **continue** when you are satisfied with detection.



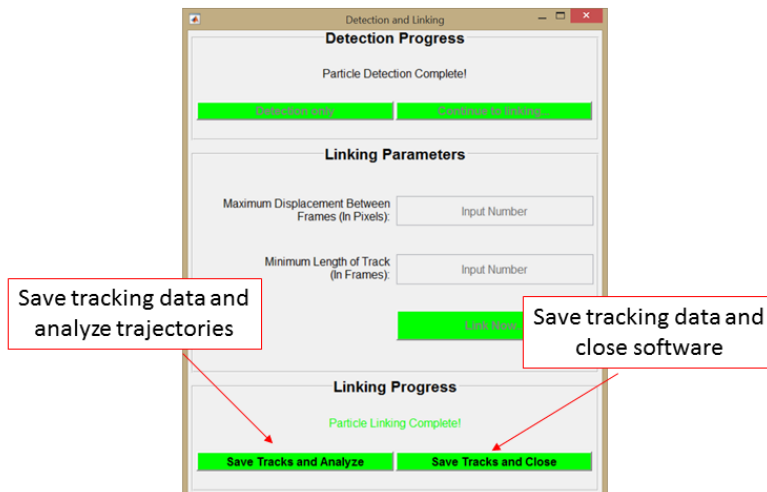
6. Whilst particle detection is running you will not have access to any of the other panel. Once detection is completed you have the option to i) Perform **detection only** and save the results and exit. ii) **Continue to linking** and form trajectories from the detected particles.



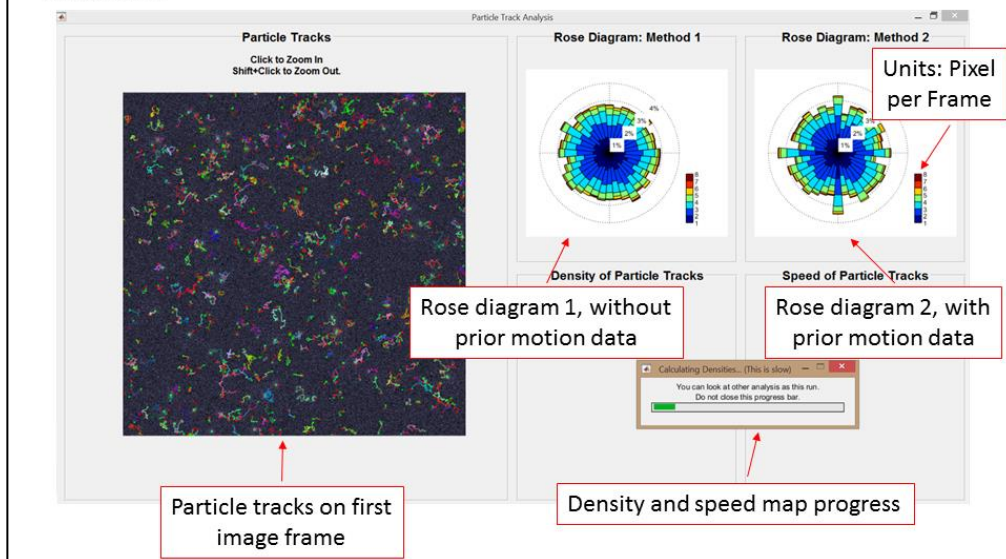
7. If you continue to linking you will be required to enter 2 more parameters. i) The maximum displacement between frames for a particles, this is related to maximum velocity of the particles. ii) Minimum track length, this is the number of consecutive detections that need to be linked to form a track, typically 3 or more.



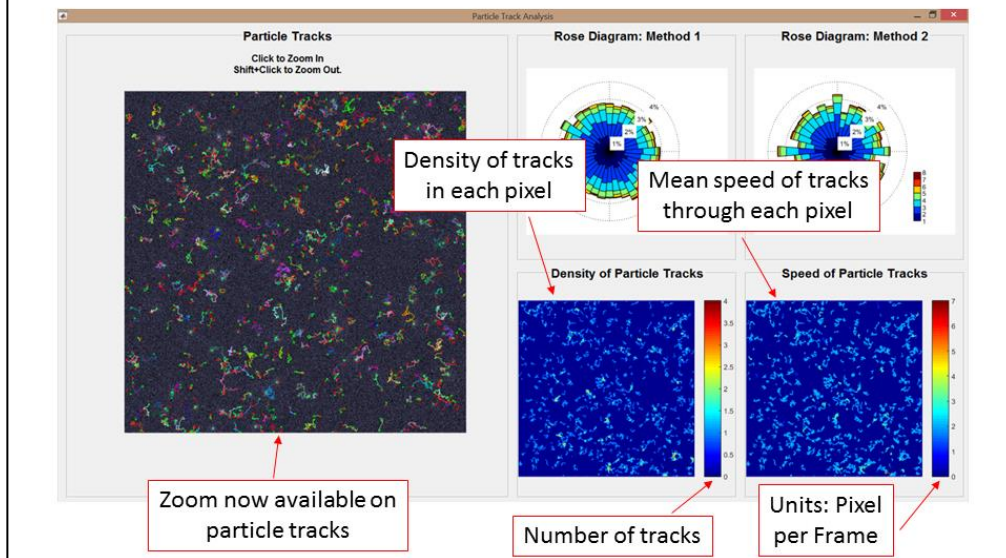
8. Once linking is complete you have 2 options. i) Save the tracks and analyze the data. ii) Save the tracks and exit the software. A pop up box appears to tell the user where the tracking and detection information has been saved.



9. If you select to **analyse** the following screen will be displayed. The **particle tracks** are displayed in colour over the first image of the input sequence. The **rose diagrams** display information of the movement of the particles within their tracks. Definitions of the 2 rose diagrams directions can be found in the paper. A progress bar is displayed for density calculation.



10. The **density** and **speed** maps will be displayed once their calculation is complete. At this stage you will also be able to zoom in and out of the **particles tracks** to view them more clearly. Close the figure to terminate the software.



References

1. Qiu, Z. et al. 2016 Translation Microscopy (TRAM) for super-resolution imaging. *Sci. Rep.* 6, 19993. (doi:10.1038/srep19993)
2. Abbe, E. 1873 Beiträge zur Theori des Mikroskops und der mikroskopischen Wahrnehmung. *Arch. für Mikroskopische Anat.* 9, 413–418. (doi:10.1007/bf02956173)
3. Meijering, E., Dzyubachyk, O., Smal, I. & van Cappellen, W. A. 2009 Tracking in cell and developmental biology. *Semin. Cell Dev. Biol.* 20, 894–902. (doi:10.1016/j.semcdb.2009.07.004)
4. Prasher, D. C. 1995 Using GFP to see the light. *Trends Genet.* 11, 320–323. (doi: 10.1016/S0168-9525(00)89090-3)
5. Zhang, J., Campbell, R. E., Ting, A. Y. & Tsien, R. Y. 2002 Creating new fluorescent probes for cell biology. *Nat. Rev. Mol. Cell Biol.* 3, 906–918. (doi:10.1038/nrm976)
6. Webb, R. H. 1996 Confocal optical microscopy. *Reports Prog. Phys.* 59, 427–471. (doi:10.1088/0034-4885/59/3/003)
7. Nakano, A. 2002 Spinning-disk confocal microscopy - a cutting-edge tool for imaging of membrane traffic. *Cell Struct. Funct.* 27, 349–355. (doi: 10.1247/csf.27.349)
8. Axelrod, D. 2001 Total internal reflection fluorescence microscopy in cell biology. *Traffic* 2, 764–774. (doi: 10.1034/j.1600-0854.2001.21104.x)
9. Betzig, E., Patterson, G. H., Sougrat, R., Lindwasser, O. W., Olenych, S., Bonifacino, J. S., Davidson, M. W., Lippincott-Schwartz, J. & Hess, H. F. 2006 Imaging intracellular fluorescent proteins at nanometer resolution. *Science* 313, 1642–1645. (doi:10.1126/science.1127344)
10. Hell, S. W. 2009 Microscopy and its focal switch. *Nat. Methods* 6, 24–32. (doi:10.1038/nmeth.1291)
11. Heintzmann, R. & Gustafsson, M. G. L. 2009 Subdiffraction resolution in continuous samples. *Nat. Photonics* 3, 362–364. (doi:10.1038/nphoton.2009.102)

12. Weber, M., Mickoleit, M. & Huisken, J. 2014 Light sheet microscopy. *Methods Cell Biol.* 123, 193–215. (doi:10.1016/B978-0-12-420138-5.00011-2)
13. Mattheyses, A. L., Simon, S. M. & Rappoport, J. Z. 2010 Imaging with total internal reflection fluorescence microscopy for the cell biologist. *J. Cell Sci.* 123, 3621–3628. (doi:10.1242/jcs.056218)
14. Rust, M. J., Bates, M. & Zhuang, X. 2006 Sub-diffraction-limit imaging by stochastic optical reconstruction microscopy (STORM). *Nat. Methods* 3, 793–795. (doi:10.1038/nmeth929)
15. Won, R. 2009 Eyes on super-resolution. *Nat. Photonics* 3, 368–369. (doi:10.1038/nphoton.2009.103)
16. Gould, T. J., Verkhusha, V. V & Hess, S. T. 2009 Imaging biological structures with fluorescence photoactivation localization microscopy. *Nat. Protoc.* 4, 291–308. (doi:10.1038/nprot.2008.246)
17. Kechkar, A. et al. 2013 Real-Time Analysis and Visualization for Single-Molecule Based Super-Resolution Microscopy. *PLoS One* 8, e62918. (doi:10.1371/journal.pone.0062918)
18. Tang, Y. et al. 2015 SNSMIL, a real-time single molecule identification and localization algorithm for super-resolution fluorescence microscopy. *Sci. Rep.* 5, 11073. (doi:10.1038/srep11073)
19. Manley, S., Gillette, J. M., Patterson, G. H., Shroff, H., Hess, H. F., Betzig, E. & Lippincott-Schwartz, J. 2008 High-density mapping of single-molecule trajectories with photoactivated localization microscopy. *Nat. Methods* 5, 155–157. (doi:10.1038/nmeth.1176)
20. Sage, D., Neumann, F. R., Hediger, F., Gasser, S. M. & Unser, M. 2005 Automatic tracking of individual fluorescence particles: application to the study of chromosome dynamics. *IEEE Trans. Image Process.* 14, 1372–1383. (doi: 10.1109/TIP.2005.852787)

21. Godinez, W. J., Lampe, M., Wörz, S., Müller, B., Eils, R. & Rohr, K. 2009 Deterministic and probabilistic approaches for tracking virus particles in time-lapse fluorescence microscopy image sequences. *Med. Image Anal.* 13, 325–342. (doi:10.1016/j.media.2008.12.004)
22. Olivo-Marin, J. C. 2002 Extraction of spots in biological images using multiscale products. *Pattern Recognit.* 35, 1989–1996. (doi:10.1016/S0031-3203(01)00127-3)
23. Starck, J.-L., Murtagh, F. & Bijaoui, A. 1998 Image processing and data analysis : the multiscale approach. Cambridge University Press.
24. Soille, P. 2003 Morphological image analysis: principles and applications. Springer.
25. Smal, I., Loog, M., Niessen, W. & Meijering, E. 2010 Quantitative comparison of spot detection methods in fluorescence microscopy. *IEEE Trans. Med. Imaging* 29, 282–301. (doi:10.1109/TMI.2009.2025127)
26. Smal, I., Niessen, W. & Meijering, E. 14-17 May 2008 A new detection scheme for multiple object tracking in fluorescence. In 2008 5th IEEE International Symposium on Biomedical Imaging, 264–267. Paris, France. (doi: 10.1109/ISBI.2008.4540983)
27. Rezaatfighi, S. H., Hartley, R. & Hughes, W. E. 2-5 May 2012 A new approach for spot detection in total internal reflection fluorescence microscopy. In 2012 9th IEEE International Symposium on Biomedical Imaging, 860–863. Barcelona, Spain. (doi:10.1109/ISBI.2012.6235684)
28. Applegate, K. T., Besson, S., Matov, A., Bagonis, M. H., Jaqaman, K. & Danuser, G. 2011 plusTipTracker: Quantitative image analysis software for the measurement of microtubule dynamics. *J. Struct. Biol.* 176, 168–184. (doi:10.1016/j.jsb.2011.07.009)
29. Yang, L., Qiu, Z., Greenaway, A. H. & Lu, W. 2012 A new framework for particle detection in low-SNR fluorescence live-cell images and its application for improved particle tracking. *IEEE Trans. Biomed. Eng.* 59, 2040–2050. (doi:10.1109/TBME.2012.2196798)

30. Genovesio, A. & Olivo-Marin, J.-C. 2004 Split and merge data association filter for dense multi-target tracking. In 2004 17th International Conference on Pattern Recognition, 677–680. Cambridge, UK. (doi:10.1109/ICPR.2004.1333863)
31. Jaqaman, K., Loerke, D., Mettlen, M., Kuwata, H., Grinstein, S., Schmid, S. L. & Danuser, G. 2008 Robust single-particle tracking in live-cell time-lapse sequences. *Nat. Methods* 5, 695–702. (doi:10.1038/nmeth.1237)
32. Sbalzarini, I. F. & Koumoutsakos, P. 2005 Feature point tracking and trajectory analysis for video imaging in cell biology. *J. Struct. Biol.* 151, 182–195. (doi:10.1016/j.jsb.2005.06.002)
33. Winter, M., Wait, E., Roysam, B., Goderie, S., Ahmed, R., Ali, N., Kokovay, E., Temple, S. & Cohen, A. R. 2012 Vertebrate Neural Stem Cell Segmentation, Tracking and Lineaging with Validation and Editing. *Nat. Protoc.* 6, 1942–1952. (doi:10.1038/nprot.2011.422.Vertebrate)
34. Celler, K., van Wezel, G. P. & Willemse, J. 2013 Single particle tracking of dynamically localizing TatA complexes in *Streptomyces coelicolor*. *Biochem. Biophys. Res. Commun.* 438, 38–42. (doi:10.1016/j.bbrc.2013.07.016)
35. Ku, T. C., Kao, L. Sen, Lin, C. C. & Tsai, Y. S. 2009 Morphological filter improve the efficiency of automated tracking of secretory vesicles with various dynamic properties. *Microsc. Res. Tech.* 72, 639–649. (doi:10.1002/jemt.20711)
36. Zhang, B., Zerubia, J. & Olivo-Marin, J.-C. 2007 Gaussian approximations of fluorescence microscope point-spread function models. *Appl. Opt.* 46, 1819–1829. (doi:10.1364/AO.46.001819)
37. Cheezum, M. K., Walker, W. F. & Guilford, W. H. 2001 Quantitative comparison of algorithms for tracking single fluorescent particles. *Biophys. J.* 81, 2378–88. (doi:10.1016/S0006-3495(01)75884-5)
38. Parthasarathy, R. 2012 Rapid, accurate particle tracking by calculation of radial symmetry centers. *Nat. Methods* 9, 724–726. (doi:10.1038/nmeth.2071)

39. Kalaidzidis, Y. 2007 Intracellular objects tracking. *Eur. J. Cell Biol.* 86, 569–578. (doi:10.1016/j.ejcb.2007.05.005)
40. Qian, H., Sheetz, M. P. & Elson, E. L. 1991 Single particle tracking. Analysis of diffusion and flow in two-dimensional systems. *Biophys. J.* 60, 910–21. (doi:10.1016/S0006-3495(91)82125-7)
41. Rogers, S. S., Waigh, T. A., Zhao, X. & Lu, J. R. 2007 Precise particle tracking against a complicated background: polynomial fitting with Gaussian weight. *Phys. Biol.* 4, 220–7. (doi:10.1088/1478-3975/4/3/008)
42. Paavolainen, L., Kankaanpää, P., Ruusuvuori, P., McNerney, G., Karjalainen, M. & Marjomäki, V. 2012 Application independent greedy particle tracking method for 3D fluorescence microscopy image series. In 2012 9th IEEE International Symposium on Biomedical Imaging, 672–675. Barcelona, Spain. (doi:10.1109/ISBI.2012.6235637)
43. Rink, J., Ghigo, E., Kalaidzidis, Y. & Zerial, M. 2005 Rab conversion as a mechanism of progression from early to late endosomes. *Cell* 122, 735–749. (doi:10.1016/j.cell.2005.06.043)
44. Jaiswal, A., Godinez, W. J., Eils, R., Lehmann, M. J. & Rohr, K. 2012 Tracking virus particles in fluorescence microscopy images using two-step multi-frame association. In 2012 9th IEEE International Symposium on Biomedical Imaging, 664–667. Barcelona, Spain. (doi:10.1109/ISBI.2012.6235635)
45. Godinez, W. 2013 Probabilistic Tracking and Behaviour Identification of Fluorescent Particles. (doi:10.11588/heidok.00015343)
46. Godinez, W. J., Lampe, M., Eils, R., Müller, B. & Rohr, K. 2011 Tracking multiple particles in fluorescence microscopy images via probabilistic data association. In 2011 8th IEEE International Symposium on Biomedical Imaging, 1925–1928. Chicago, USA. (doi:10.1109/ISBI.2011.5872786)

47. Blom, H. A. P. 1984 An efficient filter for abruptly changing systems. In 1984 23rd IEEE Conference on Decision and Control, 656–658. Las Vegas, USA. (doi:10.1109/CDC.1984.272089)
48. Blom, H. A. P. & Bar-Shalom, Y. 1988 The interacting multiple model algorithm for systems with Markovian switching coefficients. *IEEE Trans. Automat. Contr.* 33, 780–783. (doi:10.1109/9.1299)
49. Genovesio, A., Zhang, B. & Olivo-Marin, J.-C. 2004 Interacting multiple model based method to track moving fluorescent biological spots. In 2004 2nd IEEE International Symposium on Biomedical Imaging, 1239–1242. Arlington, USA. (doi:10.1109/ISBI.2004.1398769)
50. Rezatofighi, S. H., Gould, S., Hartley, R., Mele, K. & Hughes, W. E. 2012 Application of the IMM-JPDA filter to multiple target tracking in total internal reflection fluorescence microscopy images. *Med. Image Comput. Assist. Interv.* 15, 357–64. (doi:10.1007/978-3-642-33415-3_44)
51. Chenouard, N., Bloch, I. & Olivo-Marin, J. 2013 Multiple Hypothesis Tracking for Cluttered Biological Image Sequences. *IEEE Trans. Pattern Anal. Mach. Intell.* 35, 2736–3750. (doi:10.1109/TPAMI.2013.97)
52. Gordon, N. J., Salmond, D. J. & Smith, A. F. M. 1993 Novel approach to nonlinear/non-Gaussian Bayesian state estimation. *IEE Proc. F Radar Signal Process.* 140, 107–113. (doi:10.1049/ip-f-2.1993.0015)
53. Smal, I., Meijering, E., Draegestein, K., Galjart, N., Grigoriev, I., Akhmanova, A., van Royen, M. E., Houtsmuller, A. B. & Niessen, W. 2008 Multiple object tracking in molecular bioimaging by Rao-Blackwellized marginal particle filtering. *Med. Image Anal.* 12, 764–777. (doi:10.1016/j.media.2008.03.004)
54. Chenouard, N. 2010 Advances in probabilistic particle tracking for biological imaging.
55. Genovesio, A., Liedl, T., Emiliani, V., Parak, W. J., Coppey-Moisand, M. & Olivo-Marin, J.-C. 2006 Multiple particle tracking in 3-D+t microscopy: method and application to the

- tracking of endocytosed quantum dots. *IEEE Trans. Image Process.* 15, 1062–70. (doi:10.1109/TIP.2006.872323)
56. Smal, I., Draegestein, K., Galjart, N., Niessen, W. & Meijering, E. 2008 Particle filtering for multiple object tracking in dynamic fluorescence microscopy images: application to microtubule growth analysis. *IEEE Trans. Med. Imaging* 27, 789–804. (doi:10.1109/TMI.2008.916964)
57. Reid, D. 1979 An algorithm for tracking multiple targets. *IEEE Trans. Automat. Contr.* 24, 843–854. (doi:10.1109/TAC.1979.1102177)
58. Bar-Shalom, Y. 1990 Multitarget-multisensor tracking: Advanced applications. Artech House Publishers.
59. Chenouard, N., Bloch, I. & Olivo-Marin, J.-C. 2009 Multiple Hypothesis Tracking in Microscopy Images. In 2009 6th International Symposium on Biomedical Imaging, 3621–3624. Boston, USA. (doi:10.1109/ICIP.2009.5414278)
60. Haar, A. 1910 Zur Theorie der orthogonalen Funktionensysteme. *Math. Ann.* 69, 331–371. (doi:10.1007/BF01456326)
61. Papageorgiou, C. P., Oren, M. & Poggio, T. 1998 A general framework for object detection. In 1998 6th International Conference on Computer Vision, 555–562. Mumbai, India. (doi:10.1109/ICCV.1998.710772)
62. Viola, P. & Jones, M. 2001 Rapid object detection using a boosted cascade of simple features. In 2001 IEEE Computer Society Conference on Computer Vision and Pattern Recognition, 512–518 Kauai, USA. (doi:10.1109/CVPR.2001.990517)
63. Lienhart, R. & Maydt, J. 2002 An extended set of Haar-like features for rapid object detection. In 2002 International Conference on Image Processing, 900–903. Rochester, USA. (doi:10.1109/ICIP.2002.1038171)
64. Messom, C. H. & Barczak, A. L. C. In press. Fast and Efficient Rotated Haar-like Features using Rotated Integral Images.

65. Barczak, A. L. C. & Messom, C. H. In press. Real-time Computation of Haar-like features at generic angles for detection algorithms.
66. Elad, M. & Feuer, A. 1997 Restoration of a single superresolution image from several blurred, noisy, and undersampled measured images. *IEEE Trans. Image Process.* 6, 1646–1658. (doi:10.1109/83.650118)
67. Yang, L., Parton, R., Ball, G., Qiu, Z., Greenaway, A. H., Davis, I. & Lu, W. 2010 An adaptive non-local means filter for denoising live-cell images and improving particle detection. *J. Struct. Biol.* 172, 233–243. (doi:10.1016/j.jsb.2010.06.019)
68. Yang, L., Dun, A. R., Martin, K. J., Qiu, Z., Dunn, A., Lord, G. J., Lu, W., Duncan, R. R. & Rickman, C. 2012 Secretory Vesicles Are Preferentially Targeted to Areas of Low Molecular SNARE Density. *PLoS One* 7. (doi:10.1371/journal.pone.0049514)
69. Wilson, R. S., Yang, L., Dun, A., Smyth, A. M., Duncan, R. R., Rickman, C. & Lu, W. 2016 Automated single particle detection and tracking for large microscopy datasets. *R. Soc. Open Sci.* 3, 160225. (doi:10.1098/rsos.160225)
70. Chenouard, N. et al. 2014 Objective comparison of particle tracking methods. *Nat. Methods* 11, 281–289. (doi:10.1038/nmeth.2808)
71. Thompson, R. E., Larson, D. R. & Webb, W. W. 2002 Precise nanometer localization analysis for individual fluorescent probes. *Biophys. J.* 82, 2775–2783. (doi:10.1016/S0006-3495(02)75618-X)
72. Shafique, K. & Shah, M. 2005 A noniterative greedy algorithm for multiframe point correspondence. *IEEE Trans. Pattern Anal. Mach. Intell.* 27, 51–65. (doi:10.1109/TPAMI.2005.1)
73. Chenouard, N., Bloch, I. & Olivo-Marin, J.-C. 2009 Multiple Hypothesis Tracking in Cluttered Condition. In 2009 16th International Conference on Image Processing, 3621–3624. Cairo, Egypt. (doi:10.1109/ICIP.2009.5414278)
74. Liang, L., Shen, H., De Camilli, P. & Duncan, J. S. 2010 Tracking clathrin coated pits with a multiple hypothesis based method. In 2010 13th Medical Image Computing and

Computer Assisted Intervention, 315–322. Beijing, China. (doi:10.1007/978-3-642-15745-5_39)

75. Crocker, J. C. & Grier, D. G. 1996 Methods of Digital Video Microscopy for Colloidal Studies. *J. Colloid Interface Sci.* 179, 298–310. (doi:10.1006/jcis.1996.0217)

76. Lowe, D. G. 2004 Distinctive Image Features from Scale-Invariant Keypoints. *Int. J. Comput. Vis.* 60, 91–110. (doi:10.1023/B:VISI.0000029664.99615.94)

77. Boiko, T. & Winckler, B. 2003 Picket and Other Fences in Biological Membranes. *Dev. Cell* 5, 191–192. (doi: 10.1016/S1534-5807(03)00240-5)

78. Feng, Y., Dalgarno, P. A., Lee, D., Yang, Y., Thomson, R. R. & Greenaway, A. H. 2012 Chromatically-corrected, high-efficiency, multi-colour, multi-plane 3D imaging. *Opt. Express* 20, 20705–20714. (doi:10.1364/OE.20.020705.)

79. Dalgarno, P. A., Dalgarno, H. I. C., Putoud, A., Lambert, R., Paterson, L., Logan, D. C., Towers, D. P., Warburton, R. J. & Greenaway, A. H. 2010 Multiplane imaging and three dimensional nanoscale particle tracking in biological microscopy. *Opt. Express* 18, 877-884. (doi:10.1364/OE.18.000877)

80. Abrahamsson, S. et al. 2012 Fast multicolor 3D imaging using aberration-corrected multifocus microscopy. *Nat. Methods* 10, 60–63. (doi:10.1038/nmeth.2277)

81. Nolan, C. et al. 2014 *Interstellar*. Syncopy (Firm).

82. Du, Q., Faber, V. & Gunzburger, M. 1999 Centroidal Voronoi Tessellations: Applications and Algorithms. *SIAM Rev.* 41, 637–676. (doi:10.1137/S0036144599352836)

83. Andrew, A. M. 1979 Another efficient algorithm for convex hulls in two dimensions. *Inf. Process. Lett.* 9, 216–219. (doi:10.1016/0020-0190(79)90072-3)